Variable Stoichiometry Effects on Glacial/Interglacial Ocean Model Biogeochemical Cycles and Carbon Storage

Nathaniel Fillman[1], Andreas Schmittner[1], and Karin F Kvale[2]

[1]Oregon State University
[2]GNS Science

July 27, 2023

Abstract

Realistic model representation of ocean phytoplankton is important for simulating nutrient cycles and the biological carbon pump, which affects atmospheric carbon dioxide ($p\text{CO}_2$) concentrations and, thus, climate. Until recently, most models assumed constant ratios (or stoichiometry) of phosphorous (P), nitrogen (N), silicon (Si), and carbon (C) in phytoplankton, despite observations indicating systematic variations. Here, we investigate the effects of variable stoichiometry on simulated nutrient distributions, plankton community compositions, and the C cycle in the preindustrial (PI) and glacial oceans. Using a biogeochemical model, a linearly increasing P:N relation to increasing PO_4 is implemented for ordinary phytoplankton (P_O), and a nonlinearly decreasing Si:N relation to increasing Fe is applied to diatoms (P_{Diat}). C:N remains fixed. Variable P:N affects modeled community composition through enhanced PO_4 availability, which increases N-fixers in the oligotrophic ocean, consistent with previous research. This increases the NO_3 fertilization of P_O, the NO_3 inventory, and the total plankton biomass. Surface nutrients are not significantly altered. Conversely, variable Si:N shifts south the Southern Ocean's meridional surface silicate gradient, which aligns better with observations, but depresses P_{Diat} growth globally. In Last Glacial Maximum simulations, P_O respond to more oligotrophic conditions by increasing their C:P. This strengthens the biologically mediated C storage such that dissolved organic (inorganic) C inventories increase by 34-40 (38-50) Pg C and 0.7-1.2 Pg yr^{-1} more particulate C is exported into the interior ocean. Thus, an additional 13-14 ppm of $p\text{CO}_2$ difference from PI levels results, improving model agreement with glacial observations.

Hosted file

`969082_0_art_file_11225360_ryd1qt.docx` available at https://authorea.com/users/643297/articles/656731-variable-stoichiometry-effects-on-glacial-interglacial-ocean-model-biogeochemical-cycles-and-carbon-storage

1
2
Variable Stoichiometry Effects on Glacial/Interglacial Ocean Model Biogeochemical Cycles and Carbon Storage

3 **Nathaniel J. Fillman[1*], Andreas Schmittner[1†], and Karin F. Kvale[2‡]**

4 [1]College of Earth, Ocean, and Atmospheric Sciences, Oregon State University, Corvallis, OR, USA.

5 [2]Environmental Processes and Modelling, GNS Science, Lower Hutt, New Zealand.

6 Corresponding author: Nathaniel Fillman (FillmanN@oregonstate.edu)

7 * https://orcid.org/0000-0002-5380-7495

8 † https://orcid.org/0000-0002-8376-0843

9 ‡ https://orcid.org/0000-0001-8043-5431

10 **Key Points:**

11 • Variable C:P allows more physiological and ecological interactivity in plankton thereby
12   increasing the biological carbon pump.
13 • Variable Si:N affects ocean carbon cycling little but better constrains diatom and Si
14   simulations.
15 • Changes in glacial-interglacial phytoplankton C:P enhances ocean C sequestration and
16   reduces atmospheric CO_2 by $13 - 14$ ppm.

Abstract

Realistic model representation of ocean phytoplankton is important for simulating nutrient cycles and the biological carbon pump, which affects atmospheric carbon dioxide (pCO$_2$) concentrations and, thus, climate. Until recently, most models assumed constant ratios (or stoichiometry) of phosphorous (P), nitrogen (N), silicon (Si), and carbon (C) in phytoplankton, despite observations indicating systematic variations. Here, we investigate the effects of variable stoichiometry on simulated nutrient distributions, plankton community compositions, and the C cycle in the preindustrial (PI) and glacial oceans. Using a biogeochemical model, a linearly increasing P:N relation to increasing PO$_4$ is implemented for ordinary phytoplankton (P$_O$), and a nonlinearly decreasing Si:N relation to increasing Fe is applied to diatoms (P$_{Diat}$). C:N remains fixed. Variable P:N affects modeled community composition through enhanced PO$_4$ availability, which increases N-fixers in the oligotrophic ocean, consistent with previous research. This increases the NO$_3$ fertilization of P$_O$, the NO$_3$ inventory, and the total plankton biomass. Surface nutrients are not significantly altered. Conversely, variable Si:N shifts south the Southern Ocean's meridional surface silicate gradient, which aligns better with observations, but depresses P$_{Diat}$ growth globally. In Last Glacial Maximum simulations, P$_O$ respond to more oligotrophic conditions by increasing their C:P. This strengthens the biologically mediated C storage such that dissolved organic (inorganic) C inventories increase by 34-40 (38-50) Pg C and 0.7-1.2 Pg yr^{-1} more particulate C is exported into the interior ocean. Thus, an additional 13-14 ppm of pCO$_2$ difference from PI levels results, improving model agreement with glacial observations.

1. Introduction

Surface ocean plankton redistribute nitrogen (N), phosphorus (P), and carbon (C) to the deep ocean via incomplete respiration of sinking organic matter. Thereafter, respiration continues but remineralized nutrients assume the long residence times of deep ocean water masses, effectively sequestering them from the climate system. This process, known as the biological pump, increases the influx of atmospheric CO$_2$ (pCO$_2$) thereby influencing the global climate (McKinley et al., 2017; Sarmiento & Gruber, 2006; Sigman et al., 2010; Volk & Hoffert, 1985). Some C remains bound in the structures of dissolved organic molecules, termed dissolved organic carbon (DOC), but is not significantly chemically reactive to the air-sea exchange (Lønborg et al., 2020). DOC is then an additional long-lasting, depth-independent sink in the

48   inorganic ocean C cycle that allows further ocean C uptake (Jiao et al., 2010; Lønborg et al.,

49   2020). For simplicity, we include the DOC cycle in the definition of "biological C pump." The

50   oceanic biological carbon pump's influence on the global climate has long been documented

51   (Bisson et al., 2020; Falkowski, 2012; Field et al., 1998; Houghton, 2007; Nowicki et al., 2022).

52   Briefly, oceanic primary producers are estimated to export ~5–12 Pg C yr^{-1} and account for

53   ~50% of the global annual net primary production (NPP), in carbon, matching the terrestrial C-

54   fixation rates (Field et al., 1998; Nowicki et al., 2022). Thus, the biological carbon pump can

55   notably influence climate and must be simulated properly in global climate models.

56   In 1934, a close correlation between inorganic nutrient and carbon concentrations in the

57   ocean was observed by A. Redfield, leading him to suggest that, on average, plankton have

58   approximately constant C:N:P (Redfield, 1934) and that this ratio controls the relative quantities

59   of biogeochemical elements in ambient seawater (Redfield, 1958). This work has since strongly

60   influenced oceanography including the construction of global models with constant elemental

61   compositions (stoichiometry), which have been the norm until relatively recently (Martiny et al.,

62   2013). Overturning this paradigm is the well-documented adaptability of phytoplankton to

63   nutrient availability variations and recently discovered systematic variations from Redfield's

64   stoichiometry (C. Garcia et al., 2018; N. Garcia et al., 2018; Geider & LaRoche, 2002;

65   Klausmeier et al., 2004; Martiny et al., 2013; Weber & Deutsch, 2010). Phytoplankton, thus, can

66   lower their cellular quota for scarce nutrients while continuing to fix carbon, which is typically

67   more abundant (Galbraith & Martiny, 2015; Klausmeier et al., 2004; Martiny et al., 2013;

68   Moreno & Martiny, 2018).

69   While computationally inexpensive, the fixed stoichiometry simplification limits realism

70   (Flynn, 2010). The canonical fixed C:N:P of phytoplankton, in addition to fixed Si:N, may be

71   representative of the whole ocean average but its usage in global climate models smooths the

72   spatial variability of the carbon pump. As shown in this study and others, fixed ratios can impede

73   accurate simulations of primary producers, their population dynamics, ocean nutrient

74   distributions, and the biological pump (Galbraith & Skinner, 2020; Matsumoto et al., 2020;

75   Ödalen et al., 2020; Tanioka & Matsumoto, 2017). Model performance is thereby limited in

76   simulating realistic ocean carbon cycling under various climate states. The ocean modeling

77   community has started to include variable stoichiometric ratios in their simulations but few

78   capture any variability between the three primary macronutrients (C, N, and P) (Séférian et al.,

79   2020). Most of the CMIP 5 and 6 models have fixed ratios or only carry some form of

80   micronutrient to macronutrient variability, e.g., Fe:P (Pahlow et al., 2020; Séférian et al., 2020).

81   Otherwise, only a handful of fully coupled earth systems models use variable macronutrient

82   ratios, of which, three have studied the glacial C cycle implications: MESMO2 (Matsumoto et

83   al., 2020), cGENIE (Ödalen et al., 2020), and CSIRO Mk3L-COAL (Buchanan et al., 2019b).

84   Although, several simple box models have demonstrated the implications of variable

85   stoichiometry (Galbraith & Martiny, 2015; Moreno et al., 2018; Weber & Deutsch, 2010).

86   Here, we implement variable stoichiometry schemes in an intermediate complexity

87   climate/ocean model to allow a more interactive and responsive ocean carbon cycle. The C:P and

88   Si:N schemes are incrementally applied to individual plankton functional types (PFT) to

89   precisely highlight the full implications of capturing realistic biogeochemical interactions. We

90   also tune the new model slightly in a third experiment. These three configurations will be

91   collectively referred to as the variable stoichiometry models (VSMs).

92   The ordinary phytoplankton (P_O) C:P increases as ambient PO_4 concentrations decrease,

93   as observed in collected particulate organic matter (POM) (Galbraith & Martiny, 2015; Martiny

94   et al., 2013). The C:P variability can be induced by changes in the relative amounts of organic

95   molecules, e.g., proteins versus RNA, changes in nutrient resource storage, or taxonomic shifts

96   within a community (Geider & La Roche, 2002; Inomura et al., 2022; Liefer et al., 2019). C:N

97   was observed as mostly constant with planktonic heterotrophs exhibiting stable C:N:P (Ho et al.,

98   2020).

99   Diatoms (P_{Diat}) are phytoplankton that construct siliceous cell walls (or frustules) and

100 contribute to biological C storage not only through comprising a substantial portion (~1/5) of

101 global primary production but also through their frustules-enabled efficient sinking of organic C

102 to the deep ocean (Hildebrand & Lerch, 2015; Lafond et al., 2020; Zúñiga et al., 2021). P_{Diat}

103 continue to consume silicic acid, referred to simply as Si hereafter, from ambient seawater even

104 as other nutrients become scarce. Both in situ observations and culture experiments have shown

105 that the Si:N of P_{Diat} increases as Fe concentration decreases (Franck et al., 2000; Hutchins &

106 Bruland, 1998; Takeda, 1998). It is hypothesized that the formation rate of soft organic P_{Diat}

107 tissue slows faster with Fe limitations than the formation of hard siliceous tissue (Franck et al.,
108 2000; Meyerink et al., 2017).

109 The biological carbon pump may thus respond to different environmental and climatic
110 settings through changes in the stoichiometry of phytoplankton (Moreno et al., 2018). The
111 implications of these C:P and Si:N observations on our mechanistic understanding of biosphere-
112 climate interactions are not well understood (Galbraith & Martiny, 2015; Lafond et al., 2020;
113 Moreno et al., 2018; Moreno & Martiny, 2018; Séférian et al., 2020). We attempt, here, to
114 illuminate some of those mechanisms and better understand the Last Glacial Maximum (LGM)
115 to Preindustrial (PI) climate shift which promotes understanding of future climate evolution
116 (Tierney et al., 2020).

117 Variable stoichiometry may have played a significant role in carbon cycling during past
118 climate states such as the LGM when $p\mathrm{CO_2}$ was 90-100 ppm lower than PI levels (Barnola et al.,
119 1987; Bouttes et al., 2011; Du et al., 2020; Galbraith & Martiny, 2015; Lüthi et al., 2008;
120 Marcott et al., 2014; Petit et al., 1999). The biological carbon pump has been suggested to be
121 partially responsible for this $p\mathrm{CO_2}$ drawdown, but most previous modeling studies used fixed
122 stoichiometric ratios and can only explain a portion of this reduction (Brovkin et al., 2007;
123 Buchanan et al., 2019b; Khatiwala et al., 2019; Kohfeld et al., 2005). Two prior studies that have
124 used flexible stoichiometry (C:P and C:N) noted an additional 11-20 ppm reduction driven by an
125 enhanced ocean biological C storage (Matsumoto et al., 2020; Ödalen et al., 2020).

126 Here we confirm those results, but we identify additional mechanisms that increase C
127 storage. Larger primary producer biomasses are supported through improved cohabitation
128 between PFTs. We also identify and quantify the DOC component of biological C storage, which
129 responds similarly to variable stoichiometry as the dissolved inorganic C (DIC) inventory. The
130 resulting LGM climate simulations are closer to reconstruction estimates from observed $p\mathrm{CO_2}$
131 data than simulations without flexible stoichiometry (Bereiter et al., 2015; Ivanovic et al., 2016;
132 Kageyama et al., 2017). Our results suggest that the LGM biological carbon storage was stronger
133 than previous fixed-stoichiometry simulations suggested and likely contributed to the ocean's
134 LGM $p\mathrm{CO_2}$ sequestration (Galbraith & Martiny, 2015; Galbraith & Skinner, 2020; Sigman &
135 Boyle, 2000).

## 2. Materials and Methods

2.1. Model Description

This study uses the University of Victoria Earth System Climate Model (UVic-ESCM) version 2.9, a three-dimensional ocean general circulation model (GCM) coupled to single-layer atmospheric energy-moisture balance, land surface with dynamic vegetation, and dynamic-thermodynamic sea ice modules (Meissner et al., 2003; Mengis et al., 2020; Weaver et al., 2001). The ocean has a coarse resolution of $3.6° \times 1.8°$ horizontally with 19 vertical levels. Coupled to UVic-ESCM is the Model of Ocean Biogeochemistry and Isotopes (MOBI) version 2.1_08 which simulates interactive nutrient cycles (phosphate (PO_4), nitrate (NO_3), iron (Fe), and silicon (Si)), their associated particulate and dissolved organic phases, oxygen, carbon, detritus, and four PFTs: P_O, diazotrophs (P_{Diaz}) as our N-fixers, P_{Diat}, and zooplankton (P_Z) (Figure 1) (Muglia et al., 2017; Somes et al., 2010; Somes & Oschlies, 2015). Plankton growth rates are Monod functions of nutrients, temperature, and light (Sarmiento & Gruber, 2006). They are structured to consume dissolved organic P (DOP) when it is more plentiful than PO_4; this is not so for DON and NO_3 (Somes & Oschlies, 2015). C:N is 7:1 for all biological variables. In the fixed stoichiometry (*Control*) model, N:P is 16:1 for all plankton except for P_{Diaz} for which it is 40:1. For P_{Diat}, a C:Si of 7.7:1 is used.

While whole ocean P and Si are conserved, the N inventory responds interactively to imbalances between N fixation and denitrification (Kvale et al., 2021). Water column and benthic denitrification schemes, which respire organic matter in suboxic environments ($O_2 < 5$ μM), are described by Somes & Oschlies (2015). N isotopes are traced through the model and are sensitive to biological processes (Schmittner et al., 2013; Somes et al., 2010). Because portions of the ocean C cycling depend on the N cycling, C and Alkalinity are not strictly conserved. Calcium carbonate ($CaCO_3$) and silicon cycling are based on modified models of (Kvale et al., 2015) and (Kvale et al., 2021), respectively. Where applicable, modeled nutrient fields were initialized from World Ocean Atlas, 2013 datasets (H. Garcia et al., 2013; Letscher et al., 2013; Mather et al., 2008).

Upon mortality, plankton's particulate organic matter (POM) is divided into labile, semi-labile, and semi-recalcitrant categories for the mass exchange between various inventories. The

165   labile POM fraction quickly recycles into inorganic nutrients, the semi-labile into dissolved

166   organic matter (DOM), and the semi-recalcitrant fraction is retained as detrital POM. Particulate

167   organic C (POC) and DOC are implicitly calculated and traced, using C:N, from PON and DON

168   which can remineralize into the explicitly traced DIC. Thus, POC is a source to DOC and DIC,

169   and DOC is a source to DIC. Surface ocean DIC is also regulated by the air-sea gas exchange

170   and is reduced during autotrophy and calcite production. The simulated DOC represents the

171   semi-labile fraction of the observed DOC inventory. We do not simulate the fully recalcitrant

172   DOC fraction described in Lønborg et al. (2020; Somes & Oschlies, 2015).

173
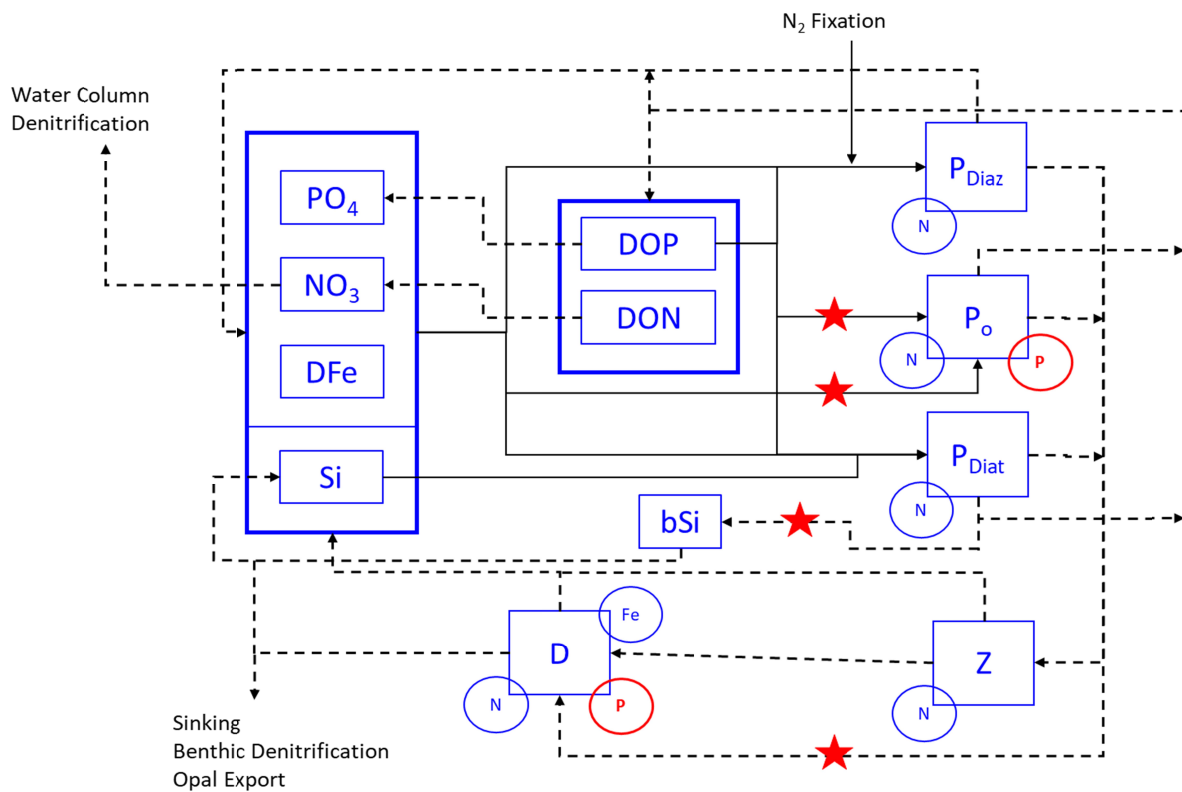
174   **Figure 1.** Schematic of MOBI's PFTs and biogeochemical cycles relevant to this study. The red

175   stars indicate where variable stoichiometric schemes were applied. VarP:N is applied at nutrient

176   uptake, while VarSi:N is applied during the implicit computation of biogenic silica. The star on

177   the pathway to the detritus (D) indicates that the VarP:N scheme is communicated to this

178   inventory. The red circled "P" indicates the new prognostic tracers added to MOBI to enable

179   computation of phosphorus content. Solid black lines indicate the flow of nutrients to each

180   plankton group, while the dashed lines show the flow back into the organic and inorganic

181   inventories.

2.1.1. Variable P:N

183   Because N is the basic currency for the biological variables in this model, we converted

184   the variable P:C model of Galbraith and Martiny (2015) (hereafter GM15) to a variable P:N

185   model using the constant C:N (Figure 2 and equation 1). For analysis purposes, we use the more

186   intuitive reciprocal (N:P) and the C:P multiple. Tanioka and Matsumoto's (2017) C:P model is

187   neglected here due to its bias toward observed high C:P values at low PO_4. Our P_O, to which

188   variable N:P is applied, inhabit and are the predominant PFT in the low PO_4 domain.

189    $$P:N\ (\text{‰})\ =42\text{‰}+48.3\text{‰}\ m^3 mmol^{-1}\times [PO_4(mmol\ m^{-3})] \tag{1}$$

190   The observations analyzed by GM15 indicate stable C:N ratios over a broad range of

191   surface nutrient concentrations, except for the most oligotrophic waters where little primary

192   production occurs. A variable C:N scheme would thus have little effect on our simulations.

193   Intracellular resource allocation models coupled to GCMs show conflicting results on the

194   stability of C:N, however, their C:P still varies substantially (Inomura et al., 2022; Pahlow et al.,

195   2020). For this reason, and to keep the model computationally efficient, we assume constant C:N

196   throughout every simulation.

197   Our variable N:P model is only applied to MOBI's P_O. While we recognize the diversity

198   in particle types (e.g., living and nonliving) in the data collected by Martiny et al. (2013) and

199   used to develop the GM15 P:C equation, we also recognize it as a broad, first-order estimation.

200   We then apply it only to the P_O, which is intended to be a representation of unspecialized surface

201   autotrophic plankton, for the following reasons. The P:C observations are biased towards

202   oligotrophic (low PO_4) waters except for the Bering Sea (Martiny et al., 2013). Consequently, the

203   observations preferentially occurred in low silicate environments, implying that siliceous

204   phytoplankton may not be a significant constituent in the collected material (Gregg & Casey,

205   2007). Thus, the variable N:P model is not extended to our P_{Diat}. Eutrophic (high PO_4) P:C

206   observations are generally at higher latitudes and may then carry a seasonal bias. MOBI also uses

207   the N:P of the well-studied *Trichodesmium* for the simulated P_{Diaz} N:P (P:C of 3.57‰) (Sañudo-

208   Wilhelmy et al., 2004; White et al., 2006). This species inhabits oligotrophic waters and thus

209   could constitute some of GM15's P:C data. However, there is substantial variability in the

210   observed P:C values at low PO_4 concentrations, and only a minority of these data points are

211   similar to the P_{Diaz} 3.57‰ value. Further, the binned log-transformed means of the data are also

212   substantially higher than this value. Thus, it is unlikely that P_{Diaz} make up any significant portion

213   of the data analyzed by Martiny et al. (2013).

214   Oceanic heterotroph stoichiometry has been found to be generally more constant and so

215   we do not apply any variability to our P_Z simulations (Galbraith & Martiny, 2015; Ho et al.,

216   2020). Because the P_Z N:P remains fixed, grazing on P_O or detritus is turned off when they have

217   a higher N:P (i.e., a low P content) at low PO_4 concentrations (equation S14). Conversely, in

218   eutrophic waters when P_O or detritus N:P is lower, P_Z only uptake enough P biomass to remain at

219   the constant ratio (N:P = 16:1) with the uptake of the N biomass. The excess P biomass, from

220   this process, is directly routed to the detritus P inventory through "sloppy feeding", a similar

221   convention as used for P_{Diaz} (Somes & Oschlies, 2015).

222   Two new prognostic equations were implemented in MOBI to explicitly calculate the

223   phosphorus content of both the P_O and the resulting detritus (Figure 1, equations S10 and S12).

224   The latter allows the scheme to affect the biological carbon pump. The variable N:P alters

225   nutrient uptake ratios by proportionally utilizing PO_4 or DOP with respect to the NO_3 according

226   to equation 1 (equations S7 and S8). Two new diagnostic equations were then added to calculate

227   the N:P of P_O (N:P_{PO}) and detritus (N:P_{Detr}) at every timestep (equation S13), which are

228   subsequently used to calculate the P loss from them (e.g., predation, mortality, remineralization,

229   etc.) (J. Moore et al., 2004).

230   **2.1.2. Variable Si:N**

231
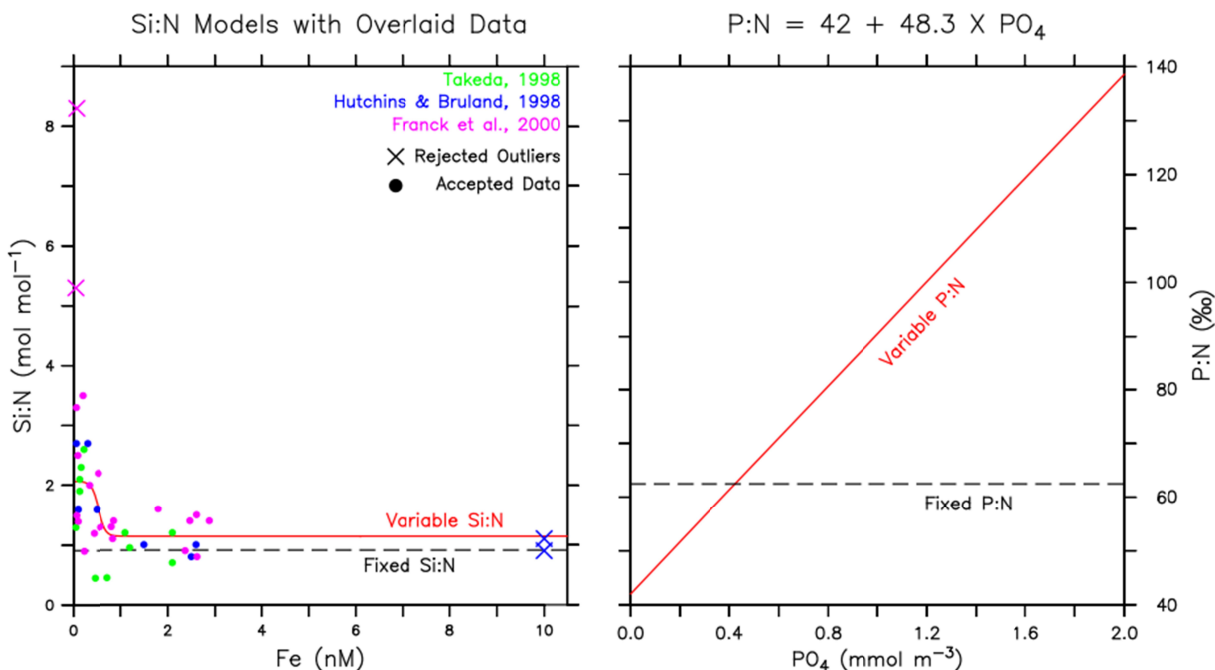
Figure 2. The variable Si:N and P:N models. Left, the variable Si:N was developed from the
overlaid data points collected from Franck et al., (2000); Hutchins & Bruland,(1998); and
Takeda, (1998). The dashed line is the fixed Si:N from Aumont et al. (2003). The rejected pink
outliers were removed as they would increase the maximum Si:N asymptote at low Fe above the
majority of the other data points, leading to increased Si consumption and further reducing the
accuracy of simulated Si concentrations. The blue outliers were discarded because they do not
significantly impact the minimum Si:N asymptote and were only achieved with artificial Fe
additions during P_{Diat} culture experiments. Further, Fe at these concentrations is rare in our
simulations and is not present in the observed data used to initialize and validate the model.
Right, the variable P:N model adapted from Galbraith and Martiny (2015) in red, overlaid with
the fixed ratio in the Control simulation.

243   P_{Diat} Si:N data, in relation to Fe availability, was compiled from three studies to develop a
predictive variable Si:N model (Franck et al., 2000; Hutchins & Bruland, 1998; Takeda, 1998).
A hyperbolic tangent was fit to the data where the mean Si:N was determined at low Fe
concentrations (<0.5 nM) and at high Fe concentrations (≥ 0.5 nM) to define the upper and

247   lower asymptotes, respectively. Other parameters were determined to achieve the most

248   statistically accurate model possible. The resulting variable Si:N model (Figure 2) is:

249    $$Si:N \left(\frac{mol}{mol}\right) = -0.46 \times tanh\left(6.9\, nM^{-1} \times [Fe\,(nM)] - 3.7\right) + 1.6 \qquad (2)$$

250   Equation 2 exhibits similar Si:N values at high Fe as other variable models, except for

251   Holzer et al.'s HYPR experiment (2019; Matsumoto et al., 2013; Matsumoto et al., 2020). While

252   we did not test these exponential models, our Si:N model does allow silica leakage,

253   complimenting their EXP1 and EXP2 findings. Conversely, because we address the large data

254   scatter at low Fe through averaging and outlier rejection, our Si:N model predicts a significantly

255   lower maximum Si:N value than those studies. The variable Si:N scheme serves to regulate the

256   P_{Diat} consumption of Si in addition to the model's preexisting nutrient limitation framework.

257   Biogenic Si is implicitly calculated from the N biomass of P_{Diat} and is only used subsequently in

258   the calculations of opal production and dissolution.

259   **2.2. General Experiment Design**

260   The effects of the VSMs on ocean biogeochemistry were isolated through four different

261   model versions. In *Control*, all stoichiometric ratios are held constant for all PFTs. Note, the N:P

262   of P_{Diaz} differs from that of other plankton but remains constant. Model *VarP:N* applies equation

263   1 to the P_O and allows this variability to affect the N:P of detritus. The detritus N:P is different

264   from that of the P_O because detritus receives input from all PFTs. Model *VarSi:N* retains *VarP:N*

265   and applies equation 2 to the P_{Diat}. The fourth model, *Tuned*, is identical to *VarSi:N*, except that

266   DOP and DON, referred to collectively as DOM, remineralization rates were accelerated five-

267   fold. This model is an initial attempt at tuning and results in more realistic DOM distributions.

268   Extensive model tuning has not been attempted here and is beyond the scope of this study.

269   PI and LGM simulations are performed with each model version. The PI simulations

270   were ran for 4,000 model years to reach a climatic and biogeochemical steady state solution.

271   Throughout this spin-up, pCO2 was fixed at a preindustrial value of 277 ppm (Bauska et al.,

272   2015). Subsequently, each simulation was ran for an additional 1,000 years with prognostic

273   variable pCO$_2$ enabled, though these remained close to PI values. LGM boundary conditions

274   were then identically applied and each model ran for an additional 5,000 years with prognostic

275   pCO$_2$ (Matsumoto et al., 2020), thus allowing the quantification of variable stoichiometry effects

276   on pCO$_2$ and climate. Analyses were performed on the PI and LGM variable pCO$_2$ simulations.

2.2.1. Last Glacial Maximum Simulation

278   LGM boundary conditions are the same as those set forth, and described in detail, by

279   Muglia et al. (2018) except for enabling prognostic pCO$_2$, which can moderate the simulated

280   climate, and neglecting the reduced sedimentary Fe flux along continental boundaries that was

281   driven by the lower LGM sea levels (Muglia et al., 2017). Tangential simulations exploring the

282   effect of these reduced sedimentary Fe fluxes, in relation to variable stoichiometry, are discussed

283   in section S4. Briefly, the LGM boundary conditions applied identically to all model

284   configurations are: elevated Fe fertilization from increased dust fluxes (south of 35°S these are

285   increased ten-fold), one salinity unit is added to every ocean grid box to account for lower LGM

286   sea levels but the ocean volume remains unchanged, wind stress fields from the PMIP multi-

287   model mean anomaly, decreased southern hemisphere moisture diffusion to increase Antarctic

288   Bottom Water production and meridional extent (Muglia et al., 2018; Muglia & Schmittner,

289   2015), orbital parameters for 21kya (Kageyama et al., 2017), prescribed ICE-6G ice sheets

290   (Peltier et al., 2015), and reduced radiative forcing at the top-of-atmosphere energy budget due to

291   lower atmospheric methane concentrations (Ramaswamy et al., 2001).

2.3. Caveats

293   There are several important caveats with the model results and the subsequent

294   experiments presented here. Firstly, the terrestrial carbon cycle does not include interactive

295   permafrost, peat, and lithologic weathering. Additionally, a portion (402 Pg) of the land C

296   inventory is instantaneously removed from the earth system with the implementation of the LGM

297   ice sheet mask (Cox, 2001; Meissner et al., 2003). This C is assumed to be buried under the ice

298   and the magnitude is consistent with prior research (Jeltsch-Thommes et al., 2019; Zeng, 2003).

299   The Atlantic Meridional Overturning Circulation (AMOC) strength in the LGM remains

300   uncertain (Muglia et al., 2018). While model results closely match some proxy reconstructions,

301   we cannot assume that the AMOC configuration is correct. We also note that the variable

302   stoichiometry effects on accurately simulating different climate states does depend, sometimes

303   strongly, on how other biologically relevant processes are simulated (section S4).

304   Several additional simplifications exist in MOBI that may affect our results. P_{Diaz} do not

305   contribute their higher C:N:P to the exported POM and are instead remineralized (J. Moore et al.,

306   2004; Somes & Oschlies, 2015). While our P_{Diaz} have a significantly different C:N:P of

307   280:40:1, their biomass, relative to other PFTs, is not large. Allowing the excess P_{Diaz} N (and

308   thereby C) to be captured in the detritus inventory increased the global weighted average N:P by

309   1.2:1 and the export ~ 0.5 Pg C year^{-1} more. The rerouting of this N to the detritus degraded the

310   accuracy of simulated surface PO_4 and NO_3 when compared to observations and so was

311   neglected. Additionally, the ocean model lacks interactive ocean sediments; organic matter is

312   instantly remineralized at the benthic interface and returned to the water column.

313   There is a significant amount of uncertainty in our DOC quantifications due to the

314   extreme complexity and variability that exists in its sources and heterotrophic processing

315   (Lønborg et al., 2020; Wagner et al., 2020). In MOBI, DOM is simply a parameterized fraction

316   of POM and its recycling varies by temperature. This may explain why the PI DOC is too low

317   compared to prior estimates in *Control, VarP:N, and VarSi:N* (Williams & Druffel, 1987).

318   Alternatively, Somes and Oschlies (2015) suggest the underestimation may be driven by DOM

319   stoichiometry variations. Thus, to achieve the observed quantities, a C:N of 11 is needed to

320   accurately convert DON to DOC. While *Tuned* better matches DON and DOP observations, its

321   DOC is significantly lower than the other simulations and would then require a C:N of 74.

322   Revising the model's DOM cycling is beyond this study's scope; we continue to use a C:N of 7

323   for DOC computations.

324   **3. Model Validation**

325   **3.1 Surface Nutrients**

326   On a global average, *VarP:N* leads to a deterioration of simulated PO_4 and NO_3

327   distributions, however, most of the error is confined to the Arctic and Southern Oceans (SO).

328   Tuning reverts most of those changes and demonstrates that a model with variable stoichiometry

329   can perform as well as a model with fixed stoichiometry. Introducing *VarSi:N*, conversely,

330   improves simulated Si distributions substantially. Thus, the *Tuned* simulation performs the best,

331   comprehensively. The Taylor diagram (Figure 3) provides a statistical synopsis by plotting the

332   normalized standard deviation (σ) (normalized by the σ of the observations) of a given nutrient

333   on the radial axis against a simulation's correlation (R) and the uncertainty-corrected root mean

334   square error (RMSE) on the azimuthal axis (Muglia et al., 2018; Taylor, 2001). A perfect

335   simulation would then have a σ and R equal to one, a RMSE of zero, and be collocated with the

336   black dots on the plot. Table S1 details the statistical metrics of the simulated nutrient

337   distributions relative to observed data from the World Ocean Atlas, 2013 (H. Garcia et al., 2013).

338
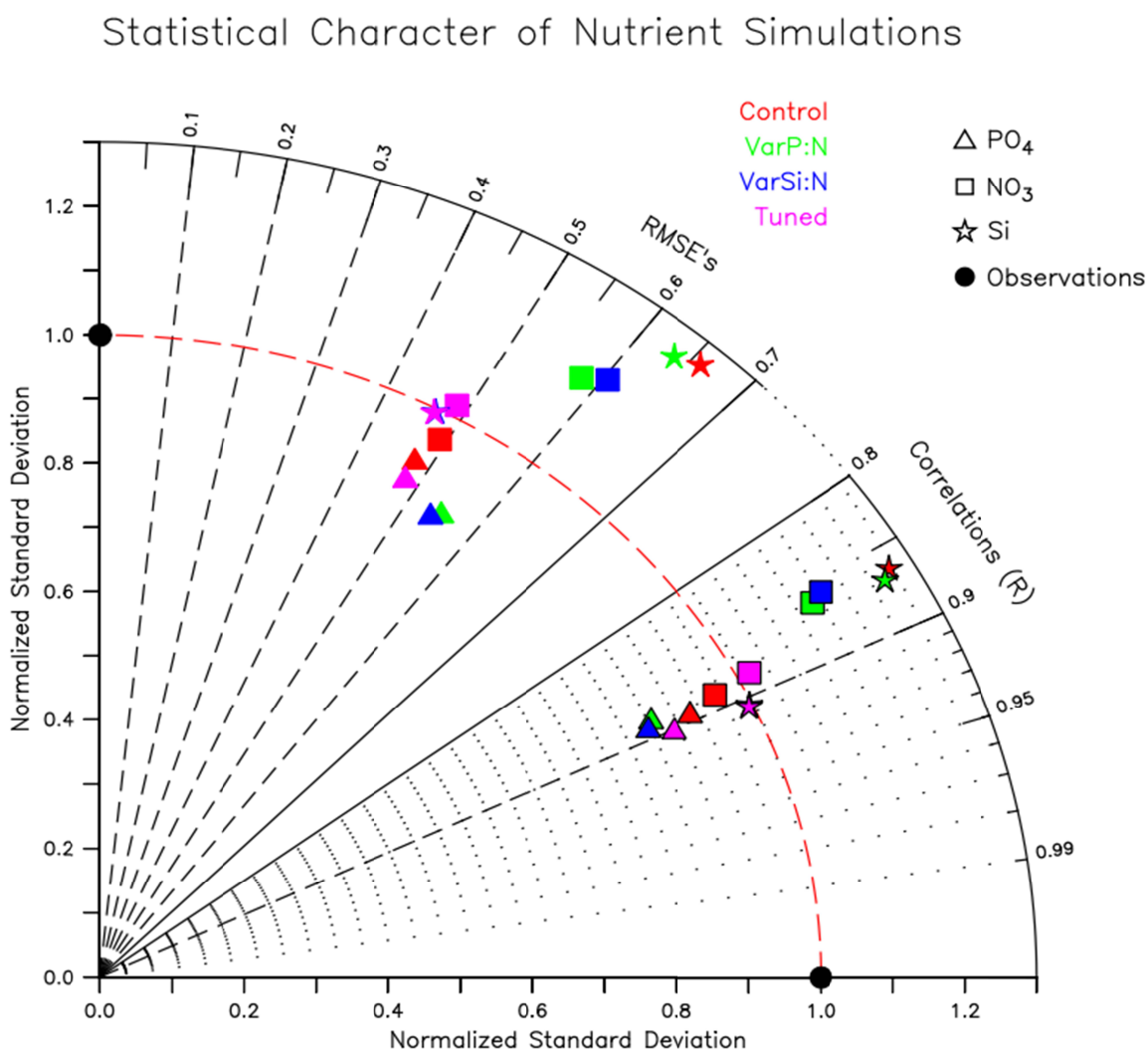
339   **Figure 3.** Taylor plot of surface simulated nutrient statistical performance. Perfect performance

340   is indicated by both black circles, thus the proximity to the respective circle can be used to assess

341   a model data point's performance. The dashed red arc indicates a model's nutrient standard

342   deviation matching that of the observed. Symbols with a black outline are plotted against the

343   correlation azimuthal axis, while those without outlines are plotted against the RMSE axis. The

344   statistical performance of surface Si simulations in VarSi:N and the Tuned models are extremely

345   similar and visual distinction here is difficult.

346   Contrary to the global perspective, the VSMs had both improving and degrading effects

347   on simulating nutrient spatial distributions, Figure 4 (H. Garcia et al., 2013; Letscher et al., 2013;

348   Mather et al., 2008). Surface NO_3 concentrations improved from the *Control* simulation due to

349   *VarP:N* almost everywhere except at high latitudes. Primary production increases cause more

350   particulate organic N (PON) export to the deep ocean, resulting in waters upwelling with higher

351   NO_3 (Figure S7). Thus, Southern Ocean NO_3, between 30°S and 60°S, now better matches the

352   observations but is still too high closer to the Antarctic margin. Increased simulated NO_3 in the

353   Pacific equatorial and Benguela upwelling currents also improve representations (Figure S1).

354   However, these areas, in addition to the Northwest Pacific, Bering Sea, and the northern Indian

355   Ocean, are still underestimated by *VarP:N* as compared to observations. In the Northeast

356   Atlantic and the Arctic, NO_3 is overestimated by the model. Model resolution and isolation of the

357   Arctic Ocean from the Pacific leads to unrealistically high nutrient concentrations there.

358   However, model-observation differences in ice-covered polar oceans may also be due to seasonal

359   biases in the observations, which lack winter data. The North Atlantic NO_3 overestimation, an

360   increase from the *Control* experiment, is caused by *VarP:N* reducing the PO_4 limitation there and

361   allowing more N-fixation, discussed later.
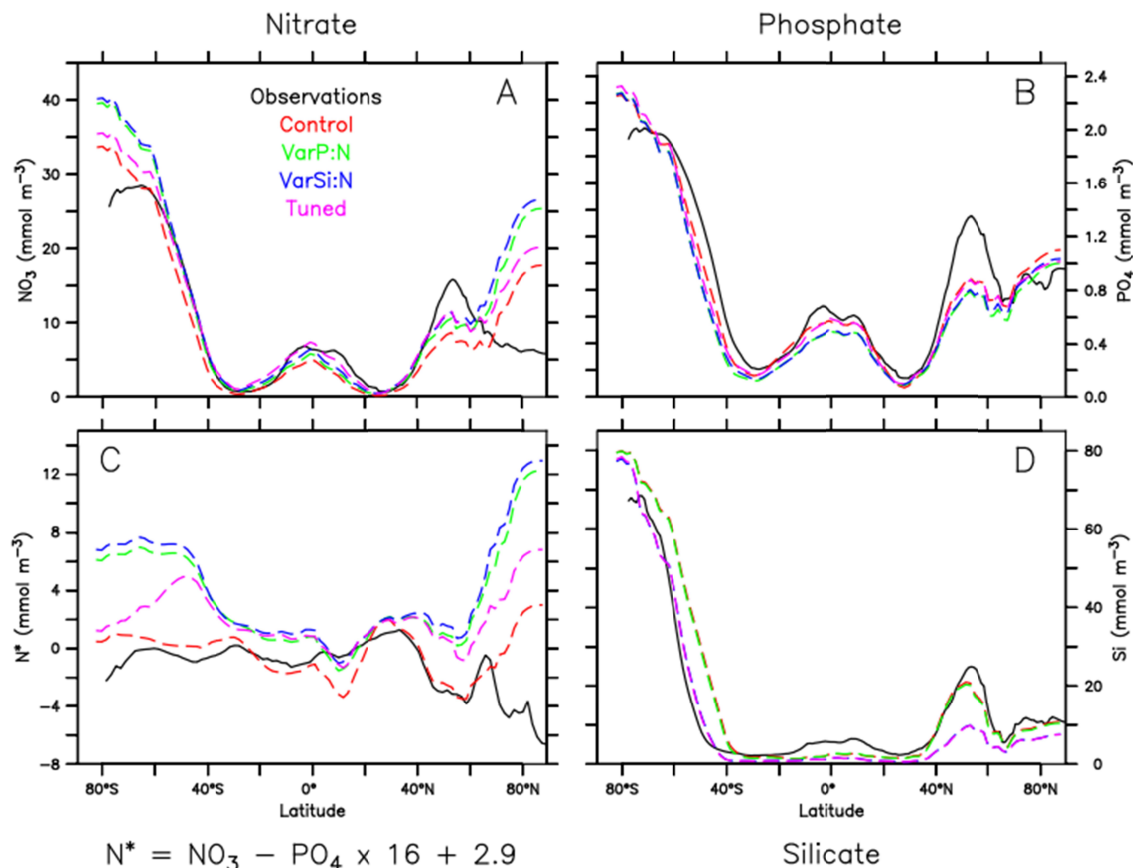
Figure 4. Zonally averaged surface nutrient concentration comparison. Observation are from the World Ocean Atlas, 2013 (H. Garcia et al., 2013). N^* expresses the deviation of the ambient $NO_3:PO_4$ from the fixed plankton N:P based on the assumption that these ratios are coupled (Redfield, 1934, 1958).

The *Tuned* model increased the extent of the elevated NO_3 concentrations, compared to the *Control*, in the tropical Pacific equatorial upwelling region. However, this area still underestimates in the East Pacific. The tuning decreased NO_3 in the Southern and Arctic Oceans, which improves the agreement with observations there, but had little effect on the NO_3 concentrations in the Bering Sea. Briefly, *VarP:N* degraded $\delta^{15}N$ simulations in the PI and LGM due to the increased export of organic matter, which upon microbial respiration depleted O_2 concentrations, thus increasing denitrification in the interior ocean and inciting more N isotope fractionation (section S5 and Figure S7). The *Tuned* model reduced the $\delta^{15}N$ inaccuracies, compared to the *Control*, in the surface ocean and only slightly degraded representations in the interior.

377   In contrast to NO_3, PO_4 concentrations were slightly reduced across all latitudes (Figure

378   4B) in response to *VarP:N*, amplifying the biases from the *Control* (Figure S2). Although P_O are

379   now more P frugal in oligotrophic environments, their increased P use in eutrophic regions and

380   the improved cohabitation with P_{Diaz} overcame this effect, leading to reduced ambient

381   concentrations. Model tuning returns simulation accuracy to approximately that of the *Control*.

382   Regardless, when considering the global C-fixation perspective, the simulated PO_4

383   underestimation is a lesser concern since PO_4 is only a limiting nutrient after Fe and NO_3

384   (discussed later), indicating that our primary producers and associated carbon pump are

385   predominantly controlled by other nutrient availabilities.

386   **3.2 Deviations from Fixed Stoichiometry (N*)**

387   Deviations from constant stoichiometry may be captured through $N^* = NO_3 - 16 \times PO_4 +$

388   2.9 (mmol m^{-3}), but N* is controlled by many processes in addition to stoichiometry (Gruber &

389   Sarmiento, 1997; Monteiro & Follows, 2012; Sarmiento & Gruber, 2006; Weber & Deutsch,

390   2010). Figure 4C shows N* only in the surface ocean to avoid denitrification influences but

391   upwelling sites may still imprint interior denitrification errors on N*. Surface N* is susceptible

392   to N-fixation which is confined between 40°S and 40°N. All model versions have preferential

393   DOP remineralization but it lacks the spatial variability seen in observations (Clark et al., 1998;

394   Monteiro & Follows, 2012). The cause, whether it be PO_4 or NO_3 inaccuracies (section S1.3), of

395   model departures from observed N* alternate by latitude and regionally. In all model versions,

396   there is a relative excess of NO_3 at the high latitudes (>60°), in the northwest North Pacific and

397   the North Atlantic, along with relatively too little PO_4 in the midlatitudes and tropics (Figures S5

398   – S6).

399   The *Control* simulation reproduces the meridional distribution of N* most accurately

400   overall. N* errors in the VSMs mostly stem from inaccuracies in N cycling outside of the

401   euphotic zone, as indicated by relatively high NO_3 at upwelling sites (Figure S5). The excess N

402   stimulates P_{Diat} growth, increasing the P consumption across the SO nutrient gradient (~ 65 –

403   35°S), and yields excess N* there (Figure 4C and S11). Under *VarP:N*, P_O are only a majority of

404   the population at PO_4 concentrations lower than ~0.1 mmol m^{-3} and are less than 20% of the

405   population at concentrations greater than ~0.55 mmol m^{-3} (Figure 5). Thus, the areas where P_O

406   are most prevalent, generally between 10 and 40°N and °S (Figure 4C and Figure S13),

407   correspond to the most accurate PO_4 and N* simulations while under *VarP:N* and are not likely

408   the direct cause of the high-latitude N* errors. The other experiments show similar patterns.

409   Alternatively, deep ocean circulations may be inaccurate and cause too much nutrient storage at

410   depth. As suggested by Weber and Deutsch (2010), flexible P_{Diat} N:P may alleviate the SO

411   nutrient gradient error by increasing P consumption at high PO_4 and decreasing it at low PO_4.

412   This, along with further tuning of the N cycle, is likely needed to reduce VSM N* biases.

413   Briefly, the North Atlantic (>40°N) is another notable area of elevated N* values that are driven

414   by higher mid-latitude N-fixation in *VarP:N* which, subsequently, causes more NO_3 to be

415   advected northward.
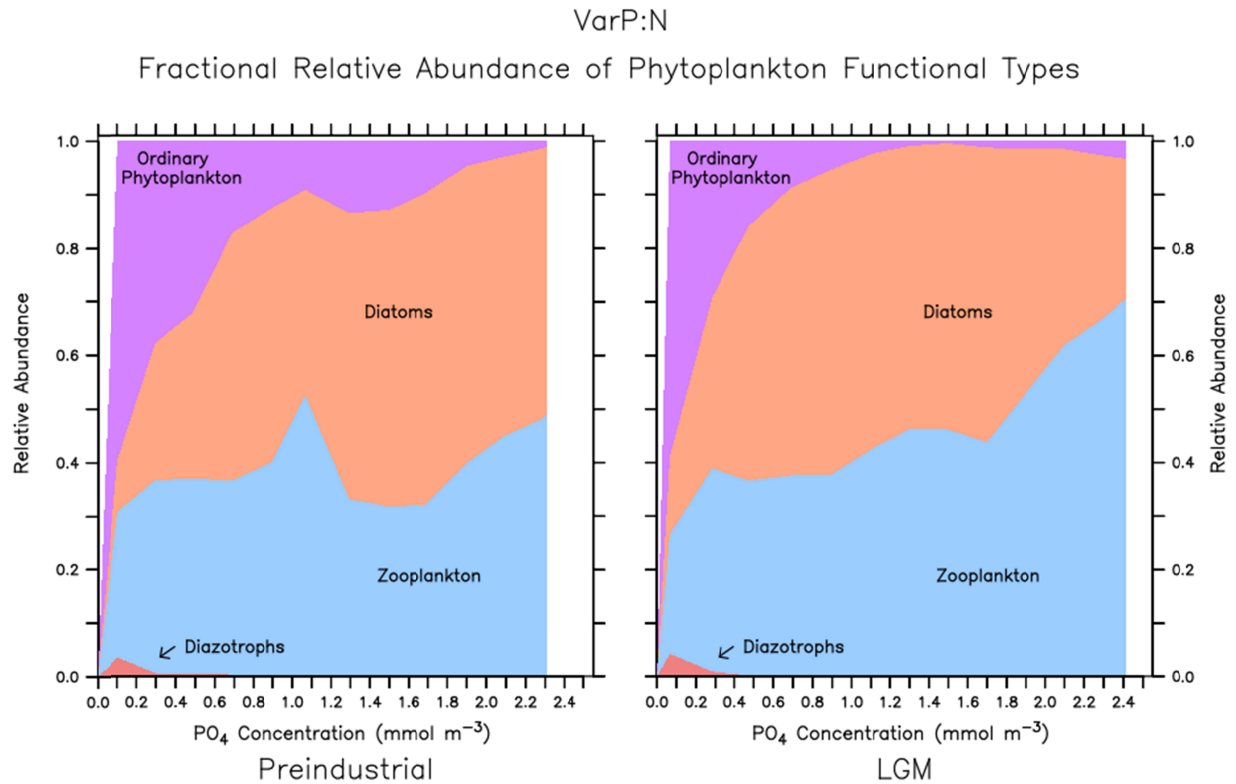
Figure 5. The fractional relative abundance of each PFT against PO_4 concentrations. Note that
the P_O are dominant only at the lowest PO_4 concentrations. Thus, the effects of VarP:N on
biological C export is through two factors. It allows P_O to adjust to their nutrient environment but
also that it is implemented on a PFT that generally occupies oligotrophic waters causing the
variable N:P scheme to increase global C export. The vertical thickness of each color indicates

422   the relative abundance of the PFT and they are overlaid to sum to one. See Figure S12 for the

423   Control.

424   *VarSi:N* improved the simulated surface Si distributions by moving the Si gradient in the

425   SO further south. However, north of 40°S, surface Si concentrations were slightly decreased

426   compared to the *Control*, enhancing the model's widespread underestimation. The largely Fe-

427   limited PI ocean drives higher Si uptake in *VarSi:N*. Notably, areas of *VarSi:N*'s Si

428   underestimation are generally not inhabited with P_{Diat}, and no other simulated PFTs use Si

429   (Gregg & Casey, 2007). The areas of important underestimation are the northwest North Pacific

430   and the Bering Sea, in which P_{Diat} do reside (Figure S3). The persistent nutrient error in this

431   region is attributed to a well-known modeled circulation discrepancy (Kvale et al., 2021; Somes

432   et al., 2017; Weaver et al., 2001).

433   **3.3 Implications of Model Tuning**

434   Preliminary model tuning was performed after *VarP:N* and *VarSi:N* with the intent of

435   improving the accuracy of PI nutrient distributions. Since DOM was overestimated in all

436   experiments*,* remineralization rates were increased 5-fold (Figure S4). While we note that

437   observations of DOM are spatially limited and carry uncertainty, the increased remineralization

438   rates did reduce the overestimation of the *Control* run to more reasonable values (Figure S4)

439   (Letscher et al., 2013; Mather et al., 2008). After tuning, simulated DOP is slightly

440   underestimated (~0.1 mmol m^{-3}) in the mid-latitude North and South Atlantic, to which the

441   available observations are restricted. DON observations include more data transects in the Indian

442   and Pacific Oceans. DON generally overestimates (~5 mmol m^{-3}) observations slightly in all

443   three ocean basins, except for the SO, where observations are slightly underestimated (~1 mmol

444   m^{-3}). These DON errors should then be considered in our DOC quantifications. These are

445   improvements, nonetheless, to the overestimated DOM values of the *Control*.

446   Additionally, the preliminary tuning drove slight improvements in inorganic nutrient

447   simulations, making the *Tuned* simulation the most accurate comprehensively (Figures S1 – S3).

448   While tuning does cause a remarkable improvement in simulated O_2 concentrations due to less

449   interior microbial respiration (Figure S7), the simulated interior ocean NO_3 is still too high,

450   although it is reduced relative to *VarP:N* and *VarSi:N*. The upwelling of NO_3 in the SO then

451   remains elevated above observations (Figure 4B). Tuning restored the PO$_4$ simulation accuracy

452   to approximately that of the *Control* while retaining the *VarP:N* and *VarSi:N* schemes. There are

453   a few areas of slight PO$_4$ improvement over the *Control* in the mid-latitudes and the tropics

454   (Figure S2). However, the *Tuned* model did not improve the strength or location of the SO PO$_4$

455   gradient. It underestimates the concentrations and places the gradient too far south. The *Control*

456   simulation remains the most accurate in this area.

457   4. Results

458   4.1. Changes in Ocean C Storage

459   Because of more C-laden organic matter and larger total primary producer biomass, the C

460   export out of the euphotic zone into the deep ocean is increased by the VSMs (Table 1, S2, and

461   S3). While each experiment has slightly different global C budgets, a symptom of the PI model

462   spin-up, C inventory differences between them are almost entirely realized within the ocean

463   (Table 2). Thus, our simulated oceans have larger C inventories in PI *VarP:N* and *VarSi:N,* than

464   the *Control*. The *Tuned* model has a slightly smaller inventory caused by the rapid processing of

465   DOC into DIC which then limits ocean C uptake from the PI atmosphere during the spin-up

466   (Figure 6).

467   **Table 1.** Global Quantifications.

PI	P$_O$ C:N:P	Export production C:N:P	Carbon export (Pg/yr)	PO$_4$ export (Pg/yr)
Control	112 : 16 : 1	112 : 16 : 1	8.8	0.62
VarP:N	141 : 20 : 1	130 : 19 : 1	9.4	0.60
VarSi:N	138 : 19 : 1	133 : 19 : 1	9.4	0.60
Tuned	134 : 19 : 1	128 : 18 : 1	9.6	0.64
LGM				
Control	112 : 16 : 1	112 : 16 : 1	7.1	0.50
VarP:N	155 : 22 : 1	141 : 21 : 1	7.7	0.45
VarSi:N	151 : 22 : 1	148 : 21 : 1	8.0	0.44
Tuned	149 : 21 : 1	146 : 21 : 1	8.3	0.46

468   *Note.* P$_O$ and EP C:N:P is the globally weighted average. EP C:N:P, C, and P export are

469   calculated from detritus at the base of the euphotic zone (120 m).

470
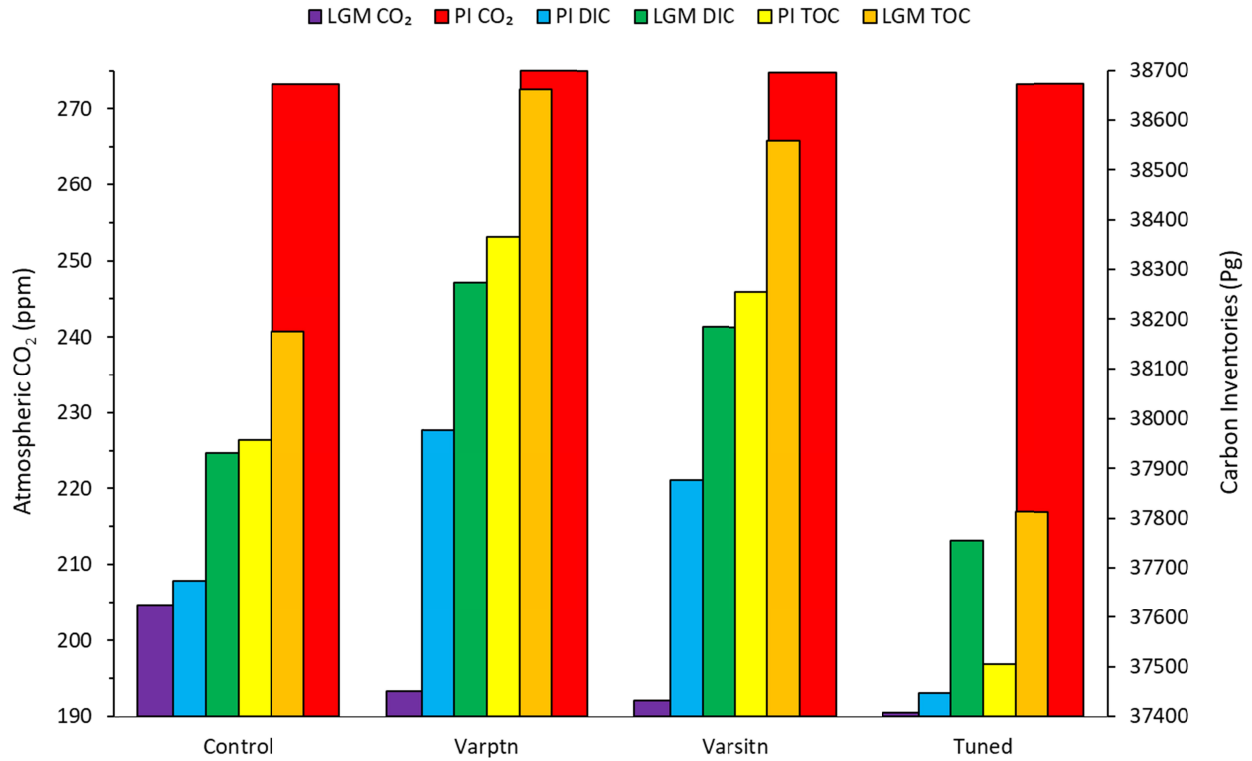
Figure 6. Comparison of pCO₂, DIC, and Total Ocean Carbon inventories in the PI and LGM.
The two pCO₂ variables use the left vertical axis, while all others use the right axis. TOC is the
sum of DIC, DOC, and POC.

Table 2. Differences in C inventories between models.

	$p\mathrm{CO}_2$ (ppm)	Ocean total carbon (Pg)	Ocean DIC (Pg)	Ocean DOC (Pg)	DOC:DIC (‰)	Land carbon (Pg)
PI:						
VarP:N – Control	2	410	304	106	2.72	4
VarSi:N – Control	1	299	203	96	2.50	3
Tuned – Control	0	-451	-227	-223	-5.91	0
LGM:						
VarP:N – Control	-11	488	342	146	3.75	-47
VarSi:N – Control	-13	384	253	130	3.37	-52
Tuned – Control	-14	-361	-177	-185	-4.86	-58
LMG-PI:						
Control[a]	-69	218	257	-38	-1.05	-73
VarP:N[a]	-82	296	295	2	-0.02	-122
VarSi:N[a]	-83	303	307	-4	-0.18	-127
Tuned[a]	-83	308	307	1	0.00	-130
VarP:N – Control[b]	-13	78	38	40	1.03	-49
VarSi:N – Control[b]	-14	85	50	34	0.88	-54
Tuned – Control[b]	-14	90	50	39	1.06	-57

475   *Note.* The PI is the top section and the LGM is the middle section. The top of the bottom

476   section ([a]) shows how a variable changes between climate states, while below that ([b]) shows the

477   relative difference of those changes. E.g., VarP:N – Control = (VarP:N, LGM – PI) – (Control,

478   LGM – PI). Notable here is that the VSMs manifested their increased LGM C storage through

479   relatively larger increases in their DIC and DOC inventories. See Table S3.

480   The LGM ocean is more oligotrophic than the preindustrial. This is largely due to slower

481   respiration, driven by cooler temperatures, and a weaker thermohaline circulation, which reduces

482   the nutrient replenishment from upwelling waters (Buchanan et al., 2016; Galbraith & Skinner,

483   2020; Matsumoto, 2007; Toggweiler, 1999; Yvon-Durocher et al., 2010). Conversely, higher

484   LGM atmospheric dust fluxes yielded more Fe fertilization to primary producers and furthered

485   nutrient consumption (Muglia et al., 2018). Our LGM configuration captures these

486   characteristics which affect stoichiometry, net primary production (NPP), and carbon cycling

487   (Muglia et al., 2018; Somes & Oschlies, 2015). Thus, our VSMs respond interactively to the

488   LGM conditions, producing substantial differences in the C inventories, compared to *Control,*

489   between the LGM and PI (Table 2). The global C budget for each experiment is approximately

490   conserved between the PI and LGM climate states.

491   The modeled total ocean carbon (TOC) inventory is the summation of DIC, POC, and

492   DOC. Carbon storage increases in the LGM ocean, relative to the PI, are largely realized in the

493   DIC inventories. In the *Control*, the global ocean DIC inventory increases by 257 Pg C (Figure

494   6, Table 2, and S3), with all other experiments seeing larger (307-295 Pg C) increases. POC

495   decreased in the LGM ocean by 13% in the *Control* and 7% in the VSMs. The smaller POC

496   reductions in the VSMs lead to LGM *VarP:N* boasting 26% more POC over the *Control*. The

497   depression of P_{Diat} in *VarSi:N* weakens this difference to 24% with similar values for the *Tuned*

498   model. Finally, DOC reduced by 13% in the *Control,* but the VSMs are approximately

499   unchanged. The LGM DOC is larger in *VarP:N* (and *VarSi:N*) by 60% (54%) than the *Control*.

500   The *Tuned* model DOC inventory is much smaller than the other models due to the accelerated

501   DOM remineralization, but this is compensated for by having the largest DIC increase from the

502   PI of any experiment.

503   The DOC invariance in the VSMs is driven by their larger LGM biomasses which

504   increase DOC sourcing via mortality (Table S2). By linearizing the DOC source and sink terms,

505   it is shown that the LGM-PI mortality changes (in particular, the P_O mortalities) are positive in

506   these experiments, whereas they are negative in the *Control* (Table S4). This contradicts the

507   temperature influence, wherein, the VSMs have greater LGM-PI temperature reductions and are

508   colder than the *Control* which slows plankton mortality and DOC recycling (sink term) rates.

509   However, the difference in VSM biomass-induced mortality changes compared to the *Control*'s

510   changes is larger than the comparative difference in the temperature influences on mortality

511   (Table S4). Further, while the VSMs' recycling rates do decrease and decrease more than the

512   *Control*, their larger DOC inventories, driven by larger biomasses, overwhelm the temperature-

513   reducing effect. Lastly, the VSMs' DOC:DIC show that DOC increases relatively more than

514   DIC, wherein the *Control* DOC:DIC is 7.4‰ (Table 2). While the ratio decreases for all models

515   in the LGM, from the PI, the VSMs reduce much less than the *Control*, denoting the remarkable

516   importance of DOC change between climate states.

517   Ultimately, the VSMs increase the ocean C storage from the LGM – PI *Control* model

518   with 38 - 50 Pg more DIC and 34 - 40 Pg more DOC (Table 2). Thus, we identify the DOC

519   response as an important, but thus far overlooked in variable stoichiometry modeling studies,

520   biological C storage mechanism. Figure S17 exemplifies these C changes with zonal averaged

521   cross-sections, wherein *VarP:N* DOC increases from the *Control* in the surface layers. Surplus

522   DOC is subsequently transported into the interior at downwelling sites but remains in the upper

523   cell of the overturning circulation while eventually degrading into DIC. Conversely, DIC is

524   relatively increased by *VarP:N* in the deep layers due to increased POC export. SO upwelling

525   draws the increased DIC to the surface where enhanced outgassing can occur, but this is

526   outweighed by the DIC reduction across all other latitudes leading to a net pCO$_2$ intake. Some

527   relatively reduced DIC is physically transported into the interior with deep water formation, but

528   additions from POC remineralization throughout the water column soon reverse the deficit into a

529   surplus of DIC.

530   The additional surface ocean C fixation and subsequent sequestration aided in further

531   ocean C uptake from the atmospheric and land inventories. *VarP:N* reduced the LGM pCO$_2$ from

532   204.7 ppm in the *Control* to 193.3 ppm. The reduction was continued by *VarSi:N* and *Tuned* to

533   192.1 and 190.5 ppm, respectively. From this and the discussed C inventory changes, the

534   variable Si:N scheme and model tuning have notably smaller C cycle impacts than *VarP:N*.

535   Each simulation did not have the same pCO_2 at the end of the respective PI simulation but the

536   *Tuned* model has the largest pCO_2 decrease of 82.8 ppm (see Figure 6 and Table 2). *VarP:N* and

537   *VarSi:N* have 81.6 and 82.6 respectively, while the *Control* has only a 69 ppm reduction. The

538   LGM pCO_2 in the VSMs are notably more consistent with ice core data than in the *Control*

539   (Bereiter et al., 2015; Ivanovic et al., 2016).

540   Beyond surface C sequestration, the VSMs reduce surface alkalinity slightly through

541   increases in $CaCO_3$ production, via P_O, and N-fixation. Changes in the ocean's pH buffer

542   capacity, as indicated by DIC:alkalinity, may then be partially responsible for the increased

543   drawdown (Egleston et al., 2010). The ratio changes little in the PI between each experiment, but

544   does more so, albeit still meagerly, in the LGM experiments (Table S3). While DIC and

545   alkalinity both slightly reduce in the surface ocean (not shown), surface DIC change is the

546   dominant effect and increases ocean CO_2 ingassing. We do not focus our analysis on this small

547   effect any further though.

548   The VSMs also restrict the land carbon inventories further than the *Control*. The lower

549   pCO_2 increased the C limitation for terrestrial primary producers and lowered global

550   temperatures (Ciais et al., 2012; Gerhart & Ward, 2010; Harrison & Prentice, 2003; Ödalen et

551   al., 2020; Prentice et al., 2011). The LGM *Control* sees a 73 Pg reduction in the terrestrial carbon

552   inventory, ignoring the ice sheet burial (Table 2 and S3). The VSMs substantially restrict it by a

553   further 67% (i.e., 49 Pg) for the *VarP:N*, 74% for *VarSi:N*, and 78% for the *Tuned* model. These

554   reductions are still smaller than prior estimates and could be caused by UVic's incomplete

555   terrestrial C cycle (Ciais et al., 2012). The TOC inventory increases are then summations of

556   carbon losses in the atmospheric and terrestrial inventories (Figure 6 and Table S3). Although

557   the model's global carbon inventory is not strictly conserved, there is only 1 - 4 Pg of

558   unaccounted for C gain during the LGM simulations, which is four orders of magnitude smaller

559   than the global C inventory.

560 **4.2. Export Production**

561   The variable N:P scheme creates regions of relatively enhanced or degraded carbon

562 fixation by primary producers, which then redefines the spatial distribution of carbon export to

563 the deep ocean. The obvious caveat to this is that the highest primary producer biomasses are

564 generally in the eutrophic regions where the C and N content of P_O is not as large relative to P. In

565 oligotrophic areas, which cover a larger ocean fraction, biomasses are low, although P_O carry

566 more C and N relative to P (Figures S1 and S2). The total effect on global export production

567 (EP) is then determined by the competing effects of these regions (Figure S14). Note that the P_O

568 ratio is different from the C:N:P of EP, which also depends on the stoichiometry of other PFTs

569 (Figures 7 and 8). The efficiency of the global biological C pump, represented by the weighted

570 C:P of EP (equation 3), increases due to PI *VarP:N* by ~18 C units, with small additions from

571 *VarSi:N*, and slight weakening from *Tuned* model due to the eutrophication caused by increased

572 DOM remineralization (Figure 7).

573 $$C:P|_{global\ EP|_{-120m}} = \left[\frac{1}{\int (EP|_{-120m})\ dA} \times \int \left(N:P_{EP|_{-120m}} \times EP|_{-120m} \right) dA \right] \times C:N \qquad (3)$$

574 The increase in the C pump's efficiency drives more net C export in the VSMs than in the fixed

575 model (Table 1). Even though the *Tuned* C:P indicates a lower efficiency compared to *VarP:N*

576 and *VarSi:N*, the higher nutrient availability supports a larger primary producer biomass (Table

577 S2) and thus a larger C export.
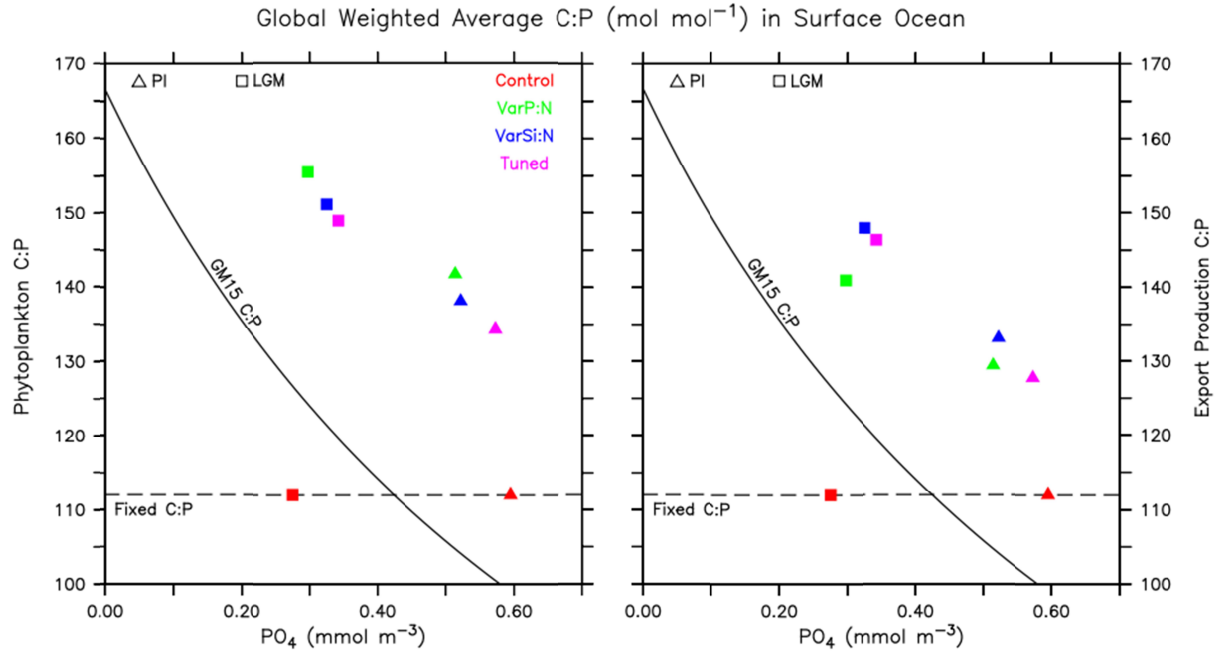
Figure 7. Global weighted average C:P of P_O in the surface ocean (0 – 120 m), left, and EP (at 120 m) which is the weighted C:P contribution of each PFT via the detritus, right. These follow equation 3 methods. The horizontal axis is the unweighted surface average PO_4 that varies slightly between each model due to the perturbations each scheme has on the simulated nutrient cycles.

The VSMs export downward more C per unit P (higher C:N:P) in the relatively oligotrophic LGM ocean than in the PI (Figure 7). Thus, the ocean C inventory increases relative to the LGM *Control*, through larger C EP (Tables 1 and 2). Notably, the P EP is slightly lower in *VarP:N*, in contrast to the C EP, but this does not indicate reduced biology as the P NPP and total biomass increase (Table 3 and S2). *VarP:N* caused a 26% increase in the LGM export C:P relative to the *Control*; *VarSi:N* an additional 5%, with the *Tuned* simulation decreasing it slightly by 1%. While the amount of C exported (Pg year^{-1}) to the deep ocean decreases in all LGM experiments, relative to their PI states, the VSMs show a smaller C export reduction than the LGM-PI *Control* because of the higher C:P's (Table 1). The sluggish ocean overturning counteracts the effects of reduced LGM C exports and increases deep ocean carbon storage (Galbraith & Skinner, 2020; Muglia et al., 2018; Toggweiler, 1999).
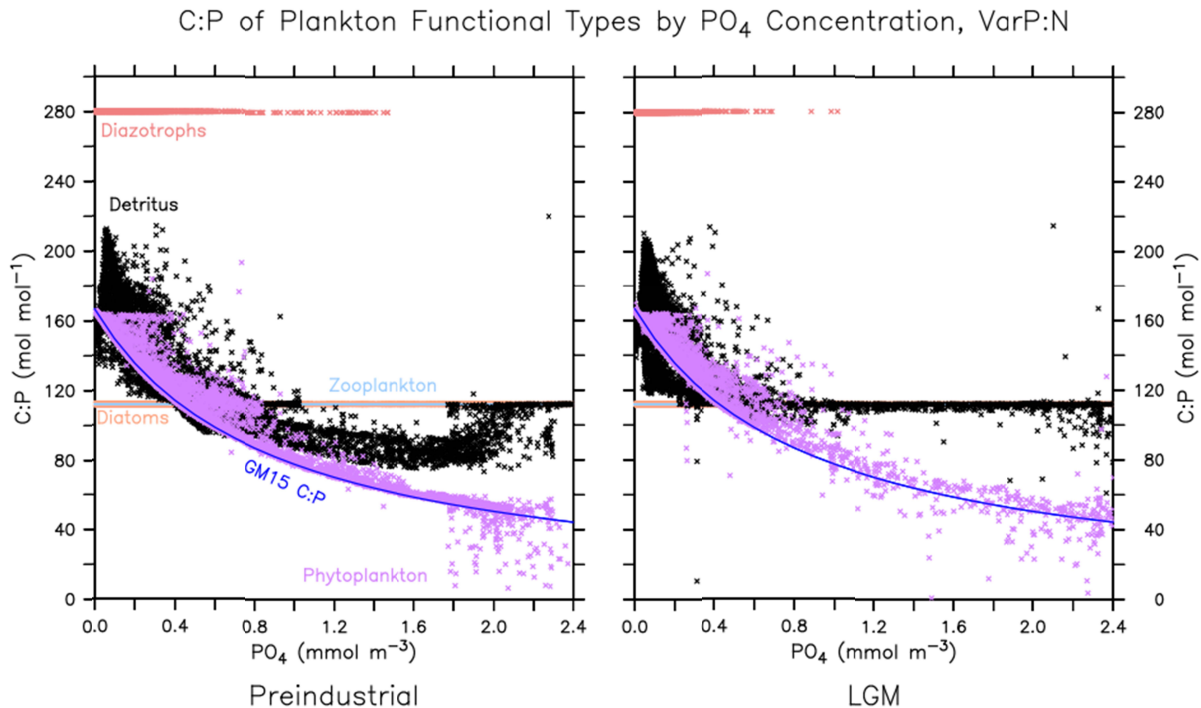
Figure 8. C:P of each PFT across simulated PO_4 concentrations. The detritus relationship is the weighted contribution of each PFT to it. The detritus C:P returns to nearly the Control ratio at high LGM PO_4 due to the significantly lower P_O and P_{Diaz} relative abundance there, Figure 5.

In PI *VarP:N*, zonal weighted average EP C:P, following equation 3, distributions match the configuration of the north and south oligotrophic subtropical gyres with the highest C:N:P between 177–168 : 25–24 : 1 (Figure 9). These ratios are not directly comparable to the weighted P_O C:N:P which is computed over different depths. In the tropics, EP C:N:P in *VarP:N* is depressed to about 124:18:1 by the eutrophic eastern Pacific equatorial upwelling waters. As expected, in the nutrient replete SO, the C:N:P ratios of EP fall below the *Control* value to ~98:14:1 mol/mol (Figure 9). Here, our results are consistent with those of Weber and Deutsch (2010) showing very similar values but *VarP:N*'s latitudinal gradients are slightly sharper (Figure 9). *VarSi:N* and *Tuned* closely match *VarP:N* except for the tropics where the *Tuned* model's greater eutrophy reduces P_O C:N:P as indicated by increases in P_O NPP (Figures 7, 9, and S9). In the LGM ocean, these patterns generally continue, but ratios tend to be higher due to enhanced oligotrophy. Additionally, with the LGM weaker upwelling in the eastern tropical Pacific and the Southern Ocean, the southern subtropical gyre broadens with peak EP C:P values

612 shifting north. Thus, a spatial expansion of efficient C export occurs there while the northern

613 gyre largely remains unchanged.

614
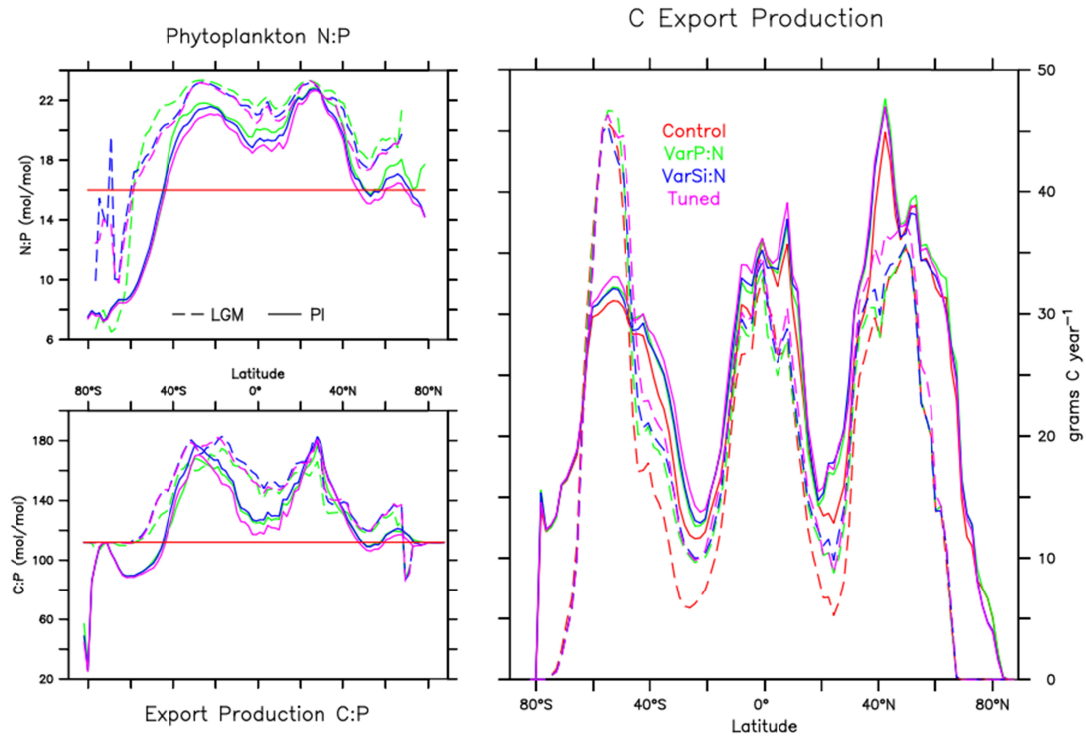
Figure 9. Zonal average P_O N:P weighted by biomass in the surface ocean (0 - 120 m), top left.
The bottom left is the same but for EP C:P computed at 120 m. Average C EP is on the right
computed at the same level.

Table 3. Globally integrated annual NPP for PI and LGM oceans.

PI	NO$_3$ NPP (Tmol yr^{-1})	PO$_4$ NPP (Tmol yr^{-1})	P$_O$ N NPP (Tmol yr^{-1})	P$_O$ P NPP (Tmol yr^{-1})	P$_{Diat}$ N NPP (Tmol yr^{-1})	P$_{Diaz}$ N NPP (Tmol yr^{-1})
Control	754.3	46.5	433.3	27.1	302.5	18.4
VarP:N	853.1	47.3	521.6	27.7	301.6	29.7
VarSi:N	854.9	47.1	642.4	34.9	183.0	29.6
Tuned	873.6	49.8	664.8	37.6	185.5	23.0
LGM						
Control	471.2	29.1	261.7	16.4	199.1	10.4
VarP:N	575.2	29.5	361.1	17.0	191.9	22.4
VarSi:N	583.7	29.5	438.4	21.3	122.8	22.7
Tuned	594.8	30.7	455.4	22.5	123.5	16.0

619 *Note.* The P NPP for P$_{Diat}$ and P$_{Diaz}$ are the same as the provided values multiplied by their

620 corresponding fixed P:N (1/16 and 1/40, respectively).

621   **4.3. Primary Producers**

622   Two effects of the VSMs on phytoplankton communities can be distinguished as
623   physiological and taxonomical changes (Matsumoto et al., 2020). Physiological effects arise
624   directly from alterations in the elemental composition of the phytoplankton. However, this also
625   changes the nutrient consumption ratios, which, in the presence of particular nutrient limitations,
626   can alter the competition between the different PFTs. This leads to two PFT, here P_o and P_{Diaz},
627   cohabitating more harmoniously. Such shifts in the phytoplankton communities are referred to as
628   taxonomic effects. Each of these effects tends to increase the biological C storage. Below, the
629   VSMs' effects are compared to the *Control*, whether PI or LGM, unless explicitly stated
630   otherwise.

631   **4.3.1. Variable P:N Physiological Changes**

632   Due to the plasticity of the P cellular quota in *VarP:N*, P_O inhabiting PO_4 depleted
633   regions are more enriched with N, and thus C, compared to P (Figure 2). Conversely, in PO_4
634   replete regions, they are less enriched. The global weighted average C:P of P_O, following
635   equation 3, in PI *VarP:N* increased to 141:1 from the *Control*'s 112:1 (Table 1, Figures 7 - 8).
636   This slightly underestimates the global observed mean of 146:1, but it may be due to the model
637   capturing high-latitude eutrophic regions where observations are absent (Martiny et al., 2013).
638   The new C:Ps indicate the larger influence of oligotrophic regions in the global average, which
639   supports a net 7% C export increase. P export, conversely, decreases slightly by 3%. The more
640   oligotrophic LGM exacerbates the N enrichment increasing P_O ratios to 155:1. The depression of
641   P_{Diat} prevalence caused by *VarSi:N* makes more P available and reduces the ratios by 8 and 4
642   units in the PI and LGM, respectively, but the net C export remained unchanged as P_O grew in
643   their place. Model tuning had a similar effect in the PI and LGM climates where increased
644   retention of N and P in the surface ocean drove slightly reduced C:Ps of 134:1 and 149:1,
645   respectively (Table 1). However, the tuning also supported more total NPP and so the PI and
646   LGM C export increased by an additional 2% and 9 %, respectively, from *VarP:N* (Table 3).
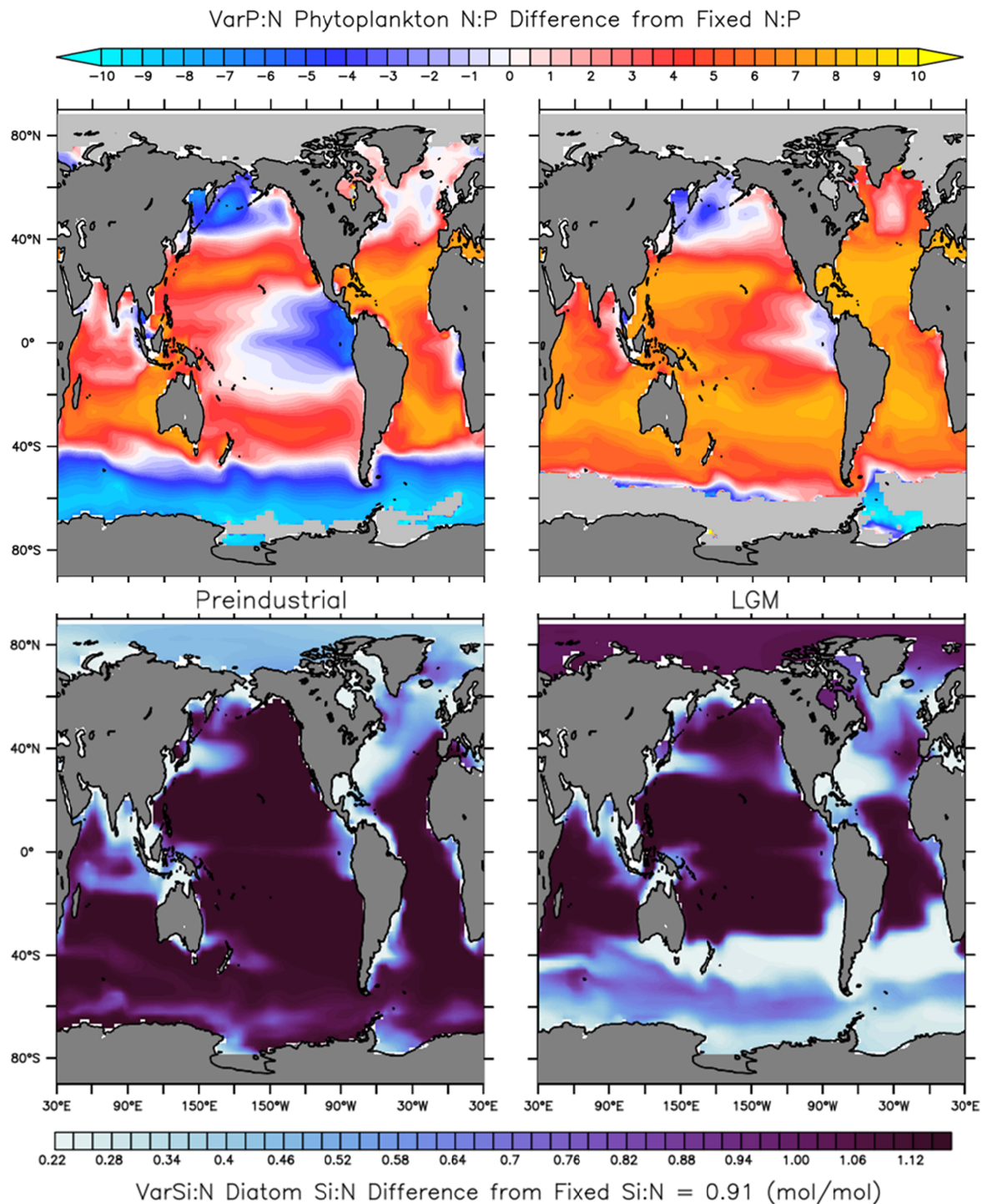
Figure 10. Stoichiometric ratio comparison. Top panels: Difference of P_O N:P under VarP:N as compared to the fixed (Control) ratio (16:1) for the PI (left) and LGM (right) simulations. The light grey colors are erroneous values caused by near-zero P_o concentrations. Bottom panels: Variable P_{Diat} Si:N in the surface ocean (0-120 m) differenced by the fixed Si:N. Light colors

652   also indicate Fe replete waters nearby the Fe source regions. The dustier LGM climate state is

653   also reflected, bottom right, with more Fe intrusion into the interior basins and the enhanced Fe

654   fertilization occurring in the SO south of 35°S.

655   P_O N:P in *VarP:N* displays more positive values in the oligotrophic regions and more

656   negative values in eutrophic regions (Figure 10). Via the fixed C:N = 7 relation, the higher N:P

657   regions indicate areas of more efficient carbon fixation, which is communicated to the deep

658   ocean through EP. Zonally averaging these ratios provides a simpler comparison of each

659   experiment. The weighted average N:P of P_O, following equation 3, in the PI surface oligotrophic

660   subtropical gyres display a value of ~ 23-21:1 (C:P = ~ 161-147:1). In the SO eutrophic waters,

661   N:P values fall far below the fixed N:P, as low as 7:1 adjacent to Antarctica (Figure 9).

662   Most of the PI zonal pattern is carried into the LGM, although south of 20°N the

663   magnitudes increase by 1-6 units in the LGM. The bimodal-like shape is also depressed in LGM

664   *VarP:N* as compared to the PI (Figure 9). The eutrophic upwelling region in the Eastern tropical

665   Pacific is the main cause of the bimodal feature in the PI, driving N:P ratios down. With weaker

666   ocean overturning in the LGM, less PO_4 is upwelled in the eastern tropical Pacific resulting in

667   higher N:P than the PI. In a small region near the most intense LGM upwelling, *VarP:N* ratios

668   still fall below the fixed N:P (Figure 10) but this feature is counterbalanced by higher N:P in the

669   western Pacific and the eastern Atlantic boundary at approximately the same latitudes. The

670   weaker upwelling has the effect of expanding the oligotrophy in the LGM Pacific, thereby

671   expanding the efficiency of the C pump there (i.e., higher C:P), particularly with the subtropical

672   gyres (Figures 9, S15, and S16). The bimodal-like N:P pattern is slightly returned in the *VarSi:N*

673   and *Tuned* experiments. In these runs, slightly more nutritious waters are upwelled in the eastern

674   Pacific driving lower N:P in this latitudinal band (Figure 9).

675   **4.3.2. Variable P:N Taxonomic Shifts**

676   Because Po are almost never P limited, their new P frugality does little to increase their

677   NPP. Their growth is predominantly limited by NO_3 and Fe (Figure 11). P_{Diaz}, however, are

678   generally P limited after Fe and never NO_3 limited. In *VarP:N*, the excess P left behind by P_O

679   fertilizes P_{Diaz}, whose NPP increases by 61% in the PI and 115% in the LGM, consistent with

680   prior research (Table 3) (C. Moore et al., 2013). Notably, the models overestimates prior global

681   C NPP estimations by ~24 - 14 Pg year[-1] (Field et al., 1998). The P_o abundance is much larger

682   than P_{Diaz}, which also has a low P requirement (N:P = 40:1) (Figure 5 and S13). Thus, the P

683   transfer to P_{Diaz} is relatively substantial. In turn, P_{Diaz} fix more N_2, if not Fe limited, and over the

684   timescales of biological cycling fertilize the N-limited P_O (Figure 11) (Buchanan et al., 2019a;

685   Capone et al., 2005; Mills & Arrigo, 2010; Wu et al., 2000). P competition between the two still

686   exists, it is simply reduced here, and they still compete for Fe (Somes et al., 2010). The improved

687   P_O-P_{Diaz} cohabitation then supports a larger biomass and biological C pump (Table 1 and S2).

688
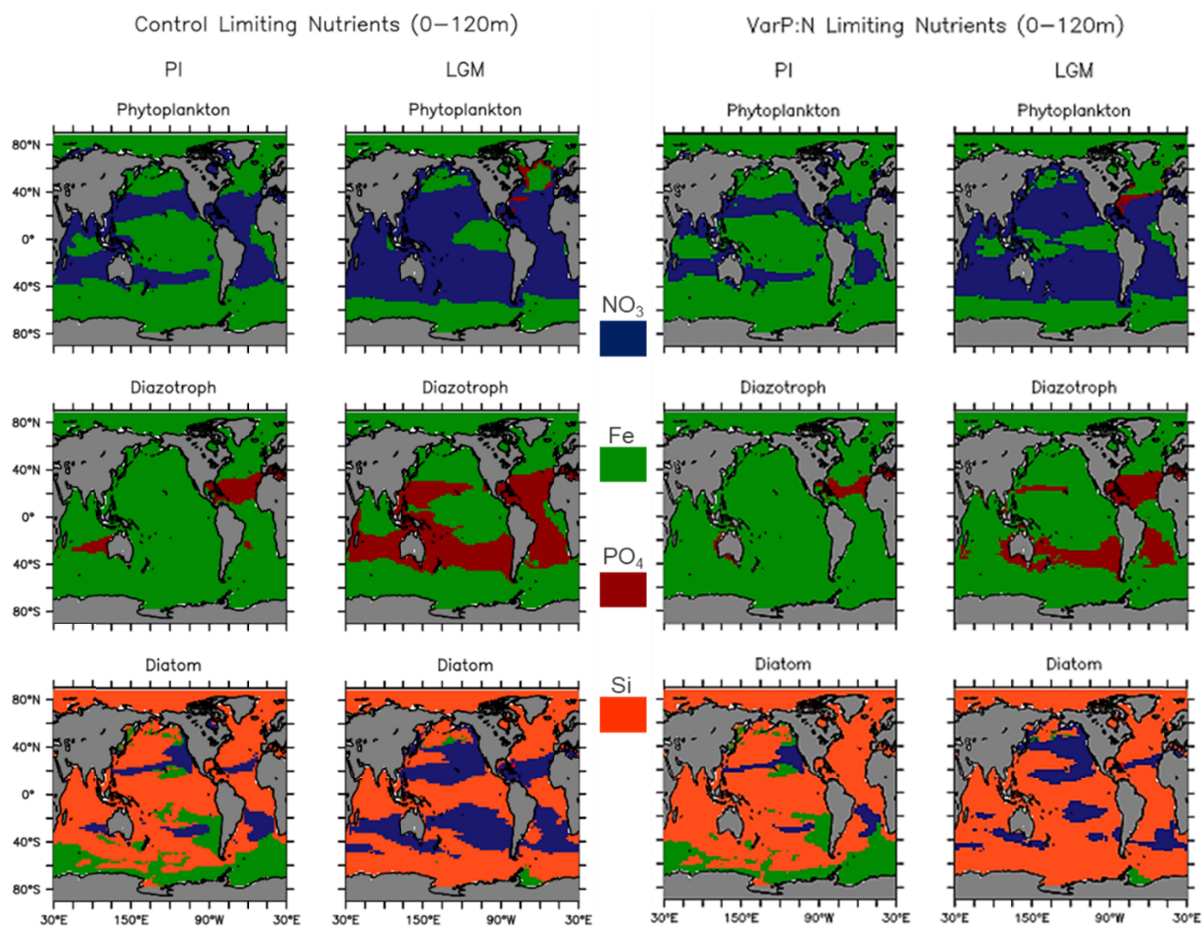
Figure 11. Primary limiting nutrients for each PFT in the surface ocean (0 – 120m). The P_{Diaz} P

690   limitation decreases due to VarP:N while the N limitation decreases for P_o and P_{Diat}. The dustier

691   LGM decreases the Fe limitation for all between the PI and LGM simulations.

692   Spatially P_{Diaz} NPP/biomass increases correlate well with P_O N NPP/biomass increases

693   which are in the Indonesian archipelago and the tropical/midlatitude western Atlantic (Figure

694   12). The cohabitation is also visualized with collocated increases in NO_3 and DON (Figures S1

695   and S4). Finally, the increases in P_{Diaz} NPP, in *VarP:N*, correlate very well with their P limitation

696   from the *Control* (Figure 12) indicating that their P limitation is relieved with *VarP:N*. The

697   exception to this is in the North Atlantic at ~20°N (J. Moore et al., 2004). Here, the P_{Diaz} are still

698   strongly limited by P even after *VarP:N*, consistent with observations (Figure 11) (Wu et al.,

699   2000). In the increased P_O-P_{Diaz} cohabitation regions, there is a mixture of P_{Diat} NPP changes, but

700   these are exceedingly smaller than the increases seen in P_O and P_{Diaz} (Figure 12, S9, and S11).

701   P_{Diat} population size is similar to P_O so the increases in P_O and P_{Diaz} productivity are not likely

702   driven by P_{Diat} population decreases. The reduced P competition between the two PFT is then the

703   most likely driver of the simultaneous growth increases. Additionally, the P_{Diat} N limitation is

704   slightly reduced in P_o-P_{Diaz} improved cohabitation areas (Figure 11). While the N limitation is

705   replaced with a Si limitation, mitigating P_{Diat} growth, the relief still evidences increased P_{Diaz} N-

706   fixation induced by more P availability.

707   Diazotroph NPP (mmol N m^{-3} s^{-1}) contoured with Control PO_4 Limitation, VarP:N−Control
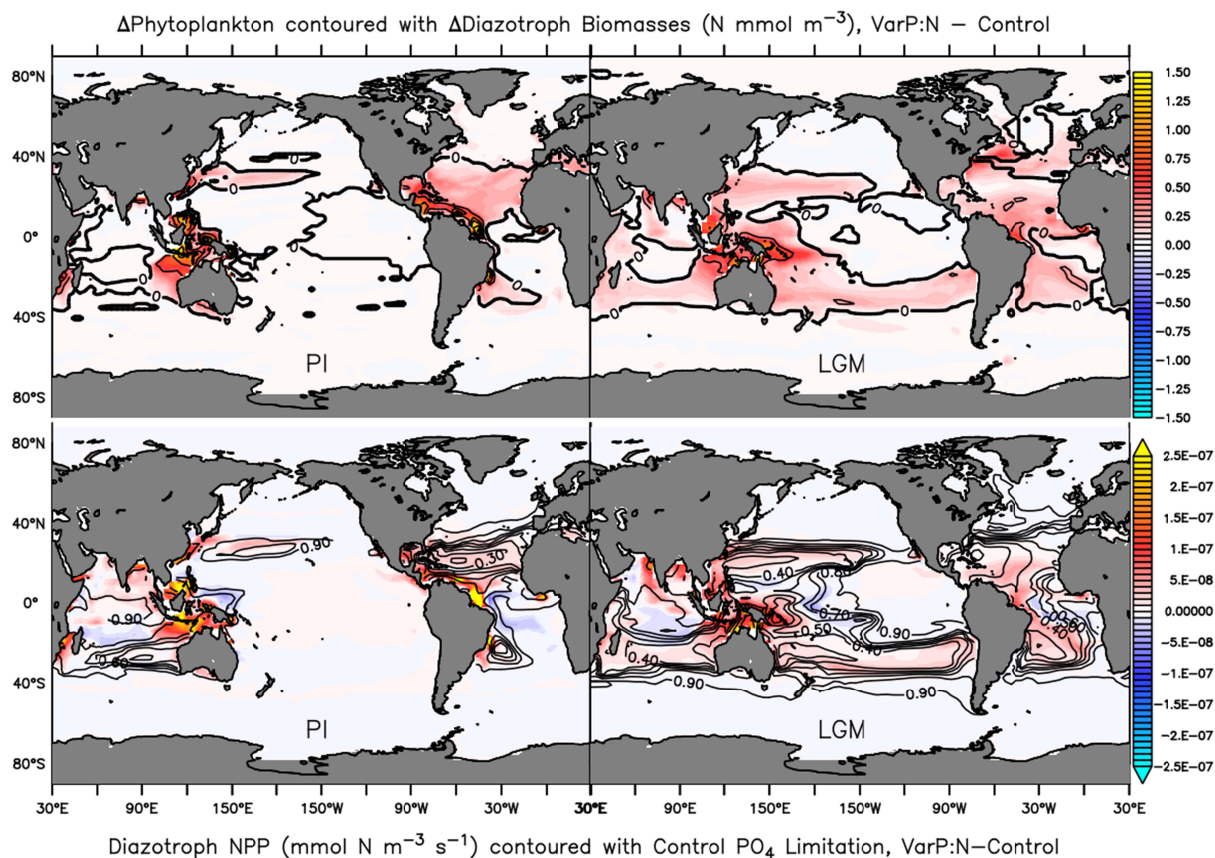
708   **Figure 12.** Biomass and growth changes in the surface ocean (0 – 120 m). The left column is PI

709   simulations, and the right is LGM. Top row: The change in P_O biomass between VarP:N and the

710   Control in the surface ocean. Contours of P_{Diaz} biomass changes are overlaid on the same scale,

711   where solid lines indicate positive values. Bottom row: Change in P_{Diaz} NPP between VarP:N

712   and the Control. Contoured lines are P_{Diaz} PO_4 limitation (from 0, meaning complete nutrient

713   limitation, to 1, meaning no nutrient limitation) from the Control. Thus, increases in P_{Diaz} NPP

714   occurring in areas that were previously PO_4 limited indicate where the VarP:N model relieved

715   the PO_4 limitation.

716   Of course, P_O and P_{Diaz} cohabitate in other regions but the nutrient collaboration may not

717   occur because either the P_{Diaz} are not sufficiently P limited or there is too strong of a Fe

718   limitation for either PFT. E.g., several areas of changing P_O P NPP do not coincide with changes

719   in N NPP, namely the tropical eastern Pacific cold tongue and the Indian Ocean, (Figure S9). In

720   these areas, the P NPP changes in response to equation 1, however, the N NPP remains nearly

721   unchanged because P_O and P_{Diaz} are predominantly limited by Fe (Figures 10 and 11) (Wu et al.,

722   2000). P_O consume Fe faster than the P_{Diaz}, which grow slower, leaving them Fe limited and

723   suppressing the usual cohabitation (Großkopf and LaRoche, 2012; Meyer et al., 2016; Tyrrell,

724   1999; Ward et al., 2013). Similar behavior continues in the *VarSi:N* and *Tuned* experiments.

725   The LGM *VarP:N* also incited regions of improved cohablation, increasing NPP totals

726   (Table 3). In the more oligotrophic LGM ocean, lower PO_4 concentrations initially made P_{Diaz}

727   more P limited than in the PI *Control* but the frugal P_O P consumption in *VarP:N* still

728   substantially relieved the limitation (Figure 11). The response is also aided by the increased

729   LGM Fe fertilization (Buchanan et al., 2019a). The spatial extent of the LGM cohabitation

730   exceeds that seen in the PI ocean but is generally bound to regions where P_{Diaz} are not Fe limited

731   (Figures 11 and 12). Compared to the PI, LGM P_O and P_{Diaz} NPP increases extend far into the

732   Pacific subtropical gyres and dominate most of the Atlantic (Figure 12).

733   The *VarP:N* model, then, prevents the N NPP reductions seen in the *Control* simulation

734   between the LGM and PI climate states. The higher LGM Fe dust fluxes relieve P_{Diaz} Fe

735   limitation (Figure 11), increasing N-fixation to nearly PI values (Table 4) (Buchanan et al.,

736   2019a). N NPP is then reduced (LGM to PI) by only 32-33% for the VSMs, compared to the

737   *Control*'s 38% reduction. The LGM-PI P NPP reduction was approximately equal across all

738   experiments, indicating more C-laden organic material.

739   **Table 4.** Global N and P inventories and fluxes.

PI:	Surface NO$_3$ ($\times 10^4$ Tg)	Total NO$_3$ ($\times 10^6$ Tg)	Surface PO$_4$ ($\times 10^4$ Tg)	N-fixation (Tg yr^{-1})	Water column denitrification (Tg yr^{-1})	Benthic denitrification (Tg yr^{-1})
Control	1.6	2.7	0.2	256.6	149.9	102.8
VarP:N	2.0	3.1	0.2	414.7	279.3	129.4
VarSi:N	2.2	3.2	0.2	412.7	275.2	130.7
Tuned	2.1	2.8	0.2	320.7	195.9	121.5
LGM:						
Control	0.9	2.6	0.1	145.9	92.6	66.5
VarP:N	1.1	2.6	0.1	313.6	267.6	86.8
VarSi:N	1.2	2.7	0.1	318.2	271.9	89.6
Tuned	1.3	2.9	0.1	224.3	155.4	86.3

740   The accelerated DON remineralization in the *Tuned* model, which causes higher net P$_O$ P

741   consumption, tempers the improved P$_O$-P$_{Diaz}$ cohabitation but it is mainly at the expense of P$_{Diaz}$

742   whose original growth is reduced by ~36 and 61% in the PI and LGM, respectively (Table 3).

743   The surface *Tuned* DOP inventory is smaller with little change to the PO$_4$ inventory, leading to a

744   P$_{Diaz}$ NPP reduction from an increased P limitation and returning it to near *Control* values (Table

745   4 and Figure S8). Conversely, P$_O$ N and P NPP increases between 33 and 36% in both *Tuned*

746   climate states.

747   **4.3.3. Variable P:N N Cycle Changes**

748   The improved P$_O$-P$_{Diaz}$ cohabitation strongly impacted the global N cycle. Increased P$_{Diaz}$

749   in *VarP:N* accelerates PI N-fixation by 62% which increased total N NPP and primary producer

750   biomass by 13% and 16%, respectively (Table 4, S2, and S3). The resulting increase in export

751   and remineralization of organic matter causes more deoxygenation and increased water column

752   denitrification by 86%, mainly in the Pacific and Indian Oceans (Table 4 and Figure S22).

753   Smaller increases (26%) occurred in benthic denitrification. While these lead to only a 15%

754   increase in the global NO$_3$ inventory, the NO$_3$ of the euphotic zone increased by 25%, thus

755   providing N limitation relief. P$_{Diat}$'s Si limitation largely limits their response to the excess N and

756   so mainly P$_O$ N NPP increases by 20% globally, with little change in their P NPP (Table 3). This

757   cohabitation-induced N-fixation thus supports more P$_O$ with flexible stoichiometry and enhances

758   C EP.

759   The increased P_{Diaz} activity induced by *VarP:N* altered the LGM NO_3 budget even more

760 than the PI. Globally, N-fixation increased by ~115% compared to the *Control* (Table 4). The

761 resulting NPP and EP increase caused further depletion of oxygen at depth where organic

762 material is respired (Figure S7). The lower O_2 levels are particularly important in the North

763 Pacific, where they crossed the denitrification threshold. *VarP:N*, consequently, causes an

764 increase in denitrification in the LGM (Figure S25) which counteracts the N-fixation increase

765 (Somes et al., 2010). Water column denitrification increased by 189% from the LGM *Control*,

766 much more than in the PI (Table 4 and Figure S22). Benthic denitrification showed a similar

767 increase as the PI of 30%. Even with the widespread expansion of P_{Diaz} and their N-fixation, the

768 global LGM *VarP:N* N inventory slightly decreased by ~ 0.7% from the LGM *Control*. In the

769 euphotic zone, however, the NO_3 inventory increased by 27%, slightly higher than the PI

770 changes.

771   The *Tuned* model reduced N-fixation and denitrification from the *VarP:N* by the

772 accelerated remineralization of DON, which fertilizes the P_O further than P_{Diaz}-sourced N alone.

773 The increased P_O growth in *Tuned* reduces PO_4 availability for P_{Diaz}, whose NPP and N-fixation

774 drop by 22% in the PI. However, the *Tuned* simulation still has 25, 31, and 18% larger N

775 fixation, water column, and benthic denitrification, respectively, compared to the *Control*

776 simulation (Table 4). Thus, the global and surface ocean NO_3 inventories are larger than the

777 *Control* and similar to *VarP:N*. This pattern continues into the LGM but the above numbers are

778 roughly doubled. The *Tuned* LGM NO_3 budget is then slightly larger (12%) than in LGM

779 *VarP:N*, while in the PI it was slightly smaller. The *Tuned* model slightly reduces the total

780 primary producer biomass but it increases the prevalence of flexible stoichiometry P_O, which

781 ultimately yields more C EP. While NPP generally decreased during the LGM relative to the PI

782 (Table 3), variable N:P allows phytoplankton communities to better adapt to the oligotrophic

783 LGM conditions.

784   **4.3.4. Variable Si:N**

785   In *VarSi:N*, P_{Diat} are enriched in Si relative to N in Fe-limited areas and depleted in Si in

786 high-Fe areas, per equation 2. This relation is especially important in the largely Fe-limited PI

787 ocean, Figure 10. *VarSi:N* increases P_{Diat} Si limitation and decreases their global NPP and

788 biomass by about 39% (Table 3, S2, and Figure 11 versus S8). In the LGM, *VarSi:N* causes a

789   36% reduction despite the increased LGM dust fertilization supplying additional Fe to the

790   surface ocean and lessening the P_{Diat} Si requirement (Conway et al., 2015; Lambert et al., 2015;

791   Muglia et al., 2017, 2018). Note, even at the highest Fe concentrations, *VarSi:N* dictates a higher

792   Si:N than the fixed Si:N scheme (Figures 2 and 12).

793   With P_{Diat} as a smaller component of the global plankton community, P_O grow in their

794   place. The P_O thus see an increase of ~12% in relative abundance, and a 23% (26%) increase in

795   N (P) NPP, whereas P_{Diaz} changes are small (Table 3 and Table S2). LGM *VarSi:N* leads to a

796   similar 21% (25%) increase in P_O N (P) NPP. The increased PO_4 availability from the reduced

797   P_{Diat} presence decreases the P_O C:P by 8 in the PI and 4 in the LGM, but this has a small effect

798   on the C EP in either climate state (Table 1 and S2). The C:P of EP changes little in the PI, but in

799   the LGM it increases by 7 due to *VarSi:N*. This occurs, counter to the C:P of P_O, because less

800   P_{Diat}, which have C:P of 112:1, exist to be exported. Instead, more P_O with flexible C:P are

801   exported and their ratios are generally higher than 112:1. The primary advantage of the variable

802   Si:N scheme is in constraining the Si and P_{Diat} simulations, but does not have as large of a C

803   cycle influence as *VarP:N*.

804   Fe-replete waters are generally along the continental margins and P_{Diat} Si:N values are

805   low and approach the fixed Si:N prescribed in the *Control* and *VarP:N* simulations (Figure 10).

806   However, most of the PI ocean is Fe limited, driving high Si:N values and causing enhanced Si

807   consumption of the already limited Si (Figures 11 and S8). Thus, P_{Diat} growth is inhibited, and

808   only P_O grow in their place since P_{Diaz} is slower growing than P_O (Table S2, Figures S11 and

809   S13). The trade-off between P_{Diat} and P_O is clearly seen in zonal plots of each PFTs relative

810   abundance in the plankton community. I.e., where P_{Diat} prevalence decreases, P_o increase. These

811   are also areas of PO_4 concentrations below 1 mmol m^{-3}, indicating that *VarSi:N* has a larger

812   influence on communities in oligotrophic regions (Figures 4 and 5). The more available nutrients

813   induced by *VarSi:N* are not reflected in the nutrient plots due to immediate P_O consumption but

814   they cause a decrease in the P_O C:N:P ratios between 20° and 40°S in the PI and LGM oceans.

815   This is the northernmost extent of the surface Si gradient in the *Control*, which, after *VarSi:N,* is

816   moved south.

817   With the exception of the higher southern latitudes, P_{Diat} Si:N values are mostly

818   unchanged between the PI and LGM. South of 35°S, enhanced dust Fe fluxes decrease Si:N

819   values to a minimum, which should allow more P_{Diat} NPP than is seen in the PI (Figure S11)

820   (Conway et al., 2015; Muglia et al., 2018). However, the reduced surface Si in the LGM (Table

821   S5), paired with more extensive sea ice, which encroaches into the primary P_{Diat} habitat (Figure

822   S13, PI versus LGM for the green P_{Diat} curve), reduces SO P_{Diat} and negates the effects of a

823   reduced LGM Si requirement caused by higher Fe fluxes. Thus, in the PI P_{Diat} NPP remains

824   largely unaffected by *VarSi:N* in the SO but in the LGM it decreases.

825   *VarSi:N* and *Tuned* support the Silicic Acid Leakage Hypothesis (SALH) where during

826   the LGM excess Si escapes the SO via surface waters, subducts into mode waters, and resurfaces

827   in the equatorial East Pacific (Brzezinski et al., 2002; Holzer et al., 2019; Matsumoto et al.,

828   2002, 2014). Figure S18 (A and B) accordingly, show *VarSi:N*'s transport of this relatively

829   increased Si, compared to *VarP:N*. The SALH postulates that, in response, more siliceous

830   phytoplankton grow in the Pacific, displacing other PFT (Figure S18, D). Decreases in the

831    $CaCO_3$:POC export denote the taxonomic shift there from calcifiers (included in P_o) to P_{Diat}

832   (Figure S18, C) (Holzer et al., 2019; Matsumoto et al., 2014). Globally, *VarSi:N* shows relatively

833   lower P_O biomass in the LGM and relatively more P_{Diat} biomass. Thus, the leakage presumably

834   enhances ocean C uptake and storage by limiting $CaCO_3$ production which increases alkalinity.

835   Our results support this but find that the SALH has a smaller global effect on the LGM ocean C

836   storage than our variable N:P model. *p*CO2 further reduces by only 1 ppm relative to *VarP:N*'s

837   13 ppm reduction and TOC increases by 7 Pg compared to *VarP:N*'s 78 Pg relative increase

838   (Table 2). *VarSi:N*'s global C export change, 0.3 Pg year^{-1}, is larger though compared to

839   *VarP:N*'s zero change (Table 1).

840   Matsumoto et al. (2014) presented three possible mechanisms to induce the Si leak. They

841   are enhanced SO Fe fertilization decreasing Si:N, more expansive sea ice that limits P_{Diat} growth,

842   and weaker SO overturning that removes SO trapping. Our model includes the enhanced Fe flux

843   and the increased sea ice in the LGM. The SO westerly wind stress is effectively unchanged

844   from the PI, however, confirming their conclusion that it may not be a required trigger

845   (Matsumoto et al., 2014). A detailed investigation of the SALH is beyond this research and we

846   do not investigate the sensitivities or causes therein.

847   **5. Discussion**

848   The ubiquitous fixed phytoplankton stoichiometry assumption has been shown to limit

849   model performance, predominantly through the spatial smoothing of the biological C pump

850   (Matsumoto et al., 2020; Ödalen et al., 2020). The results presented here, among other studies,

851   suggest that the implementation of variable stoichiometry can not only affect the simulations of

852   the biological pump but also the structure of phytoplankton communities through taxonomic

853   shifts and changes in nutrient limitations. Thus, the inclusion of variable stoichiometry in global

854   climate models can enhance ocean C storage through larger DIC and DOC inventories causing a

855   further 13 – 14 ppm drawdown of pCO$_2$ between the LGM and PI climate states. Per our results,

856   we stress the importance of the DOC inventory response to variable stoichiometry, which has

857   been overlooked previously. While the DOC inventory is much smaller than the DIC, it responds

858   by a similar magnitude as DIC to the GM15 model. In the following section, we compare our

859   results to prior research and find that they are consistent, suggesting that our quantifications of C

860   inventories, fluxes, and changes are reasonable.

861   From the PI climate state to the LGM, Matsumoto et al.'s (2020) pCO$_2$ reduced by 34

862   ppm under fixed C:N:P whereas our results show a 69 ppm reduction that is closely matched by

863   Ödalen et al.'s (2020) 64 ppm reduction. These pCO$_2$ reductions strongly depend on the

864   configuration of forcing conditions implemented in a given model for LGM simulations (as

865   suggested in section S4). However, the effects of variable stoichiometry on pCO$_2$ are similar

866   across these studies. Matsumoto et al.'s (2020) GM15 framework was responsible for an

867   additional 11 ppm drawdown and their power law model a 20 ppm drawdown. Ödalen et al.'s

868   GM15 scheme was responsible for a slightly higher reduction of 16 ppm while our schemes vary

869   between 13 and 14 ppm.

870   The differences in pCO$_2$ response may partly stem from different biogeochemical

871   simulation methods. For example, MOBI normally, though unrealistically, instantaneously

872   disassociates the P$_{Diat}$'s soft tissue from their silica frustules and routes it to the detritus

873   inventory, which has a slower sinking velocity (~3 times) than the simulated biogenic silica

874   (Zúñiga et al., 2021). The accelerated sinking of P$_{Diat}$ POM, via silica ballasting, could add ~3.7

875   to 1.3 Pg C year^{-1} to the deep ocean inventory (section S3.1 and Table S5), and presumably cause

876 a further 3-6 ppm pCO$_2$ reduction, putting our model roughly between the power law and GM15

877 quantifications (Matsumoto et al., 2020; Ödalen et al., 2020, respectively).

5.1. Carbon Export and Ocean Storage

879 At the PI steady state, the VSMs have higher export C:N:P (Figure 7 and Table 1) than

880 Ödalen et al.'s (2020) C:P of 121:1, who uses GM15 in the model cGENIE. Tanioka &

881 Matsumoto (2017), using a stoichiometric power law for C:P in the MESMO2 model, found a

882 notably lower PI ratio of 103:15:1. In subsequent studies, these authors substantially revised the

883 power law scheme and also tested the GM15 relation in MESMO2 (Matsumoto et al., 2020;

884 Tanioka & Matsumoto, 2020). The new power law produced 113:16:1 and the GM15 scheme

885 107:16:1.

886 While Matsumoto et al. (2020) suggest that low export C:N:P in their findings, is driven

887 by the lack of preferential nutrient remineralization, the cGENIE model also carries this

888 simplification but better matches our model, which does include it. Although, the cGENIE and

889 MOBI similarity could be induced by cGENIE only having one PFT, and thus a more expansive

890 application of GM15's variable C:P, which may overcome the lack of preferential nutrient

891 remineralization. Another possibility for the C:P difference between these studies is likely a

892 symptom of GM15 implementation methods, in which Matsumoto et al. (2020) applied it to all

893 PFTs, thus inciting nutrient frugality everywhere, creating an excess of PO$_4$, and lowering ratios.

894 Finally, the performance of stoichiometric schemes could be sensitive to the differences in

895 simulated biogeochemical processes and inventories between the models. For example, we have

896 shown that the increased P$_O$-P$_{Diaz}$ cohabitation partly explains the increases in ocean C

897 sequestration in *VarP:N*. However, this process is partly controlled by Fe availability. Thus,

898 when a different LGM sub-grid bathymetry mask adjusts sedimentary Fe fluxes and reduces both

899 the global and euphotic zone Fe inventories, the implications of our VSMs are not as profound

900 (section S4 and Table S6). The biogeochemistry in MESMO2 and cGENIE could be different

901 from MOBI's and so cause the differences in the variable stoichiometry effects. Further testing is

902 needed to discover the sensitivities of any given stoichiometry model to variations in simulated

903 biogeochemical processes and inventories.

904   The LGM climate state, with oligotrophic surface waters, increases the stoichiometric

905   ratios across these studies. *VarP:N* EP C:P increases by 11 C units in the LGM, which is smaller

906   than expected, per equation 1, based on the PO_4 change but is caused by the increased prevalence

907   of fixed stoichiometry PFTs (Figures 5, 7 and Table 1). Matsumoto et al.'s (2020) LGM GM15

908   C:P is substantially lower than ours at 120:1 but their C:P ratios increase by approximately the

909   same magnitude between the PI and LGM as our simulations. Conversely, their power law model

910   induces a 27-unit C:P increase, bringing it to about the same ratio as *VarP:N*. Ödalen et al.'s

911   (2020) LGM GM15 experiment sees a similar increase to *VarP:N* at 13 units. The *VarSi:N* and

912   *Tuned* experiments show increases of 15 and 18 C units, respectively.

913   The EP C:P change consequently alters the POC and POP export. The power law model

914   causes a smaller impact on C export (Matsumoto et al., 2020; Tanioka & Matsumoto, 2017,

915   2020). They found a 0.04 Pg C year^{-1} increase in the PI while our *VarP:N* shows a 0.59 Pg C

916   year^{-1} increase (Table 1) (Tanioka & Matsumoto, 2017). Subsequently, Matsumoto et al.'s (2020)

917   PI C export shows a 0.4 Pg C year^{-1} power law increase and 0.1 Pg C year^{-1} decrease under

918   GM15. The 2020 power law revision brings the two models into much better agreement with

919   respect to absolute numbers, but their usage of GM15 produces a carbon export change, relative

920   to the fixed-ratio simulations, that is of opposite sign to our results. All our simulations are

921   consistent with observation-derived estimations though the range is broad (Boyd & Trull, 2007).

922   Buchanan et al., (2019b) briefly report an increase of 0.4 Pg yr^{-1} in PI C EP due to GM15 in the

923   CSIRO model.

924   From the PI to LGM, the *Control* POC and POP reduce by the same 19% (Table 1).

925   However, in *VarP:N*, the POP export reduced by 26% while the POC export only reduced by

926   17.6%. Thus, sinking organic particles are more carbon-laden and the biological C pump is more

927   efficient under *VarP:N* than the *Control*. Our remaining experiments, *VarSi:N* and *Tuned*, do not

928   substantially alter these results. Ödalen et al.'s (2020) GM15 scheme reports a similar LGM POC

929   export decrease, relative to the PI, of 5% less than their fixed stoichiometry simulation and 2%

930   larger of a POP decrease. Matsumoto et al.'s (2020) GM15 showed the same POC export

931   reduction but with a 5% larger POP reduction. Alternatively, under the power law, the POP

932   reduced by a further 6%, compared to a fixed ratio simulation, and the POC export reduction was

933   12% less. Thus, the biological pump responds similarly across three different climate models if

934   the GM15 scheme is implemented contrary to the notably different C:Ps. Matsumoto et al.'s

935   (2020) annual C export decreases (LGM - PI) between 0.5 (power law), 1.1 (GM15), and 1.6 Pg

936   C yr^{-1} (fixed), compared to 1.4 Pg C yr^{-1} in our *Tuned* model and 1.7 Pg C yr^{-1} in our *Control*

937   experiment. Their GM15 LGM C EP quantification is very similar to our results, yet their power

938   law model changes little and is closer to our PI C EP (Table 1). Ödalen et al. (2020) did not

939   report any C export quantifications.

940   With the similarities of our findings to other studies which use unique ocean

941   biogeochemical and climate models, the quantifications of the biological carbon pump and the

942   effects of including realistic variable stoichiometry presented here are reasonable and likely good

943   approximations in the LGM climate. While our model carries some limitations and

944   approximations, we have exemplified how the configuration of a model's biogeochemistry may

945   influence these quantifications of the biological C pump and the effects variable stoichiometric

946   schemes may have on it. Further research on the sensitivities of variable stoichiometry schemes

947   to various biogeochemical processes is needed.

948   **6. Conclusions**

949   Variable stoichiometry schemes allow simulated primary producers to adapt to a variety

950   of nutrient environments consistent with observations. The variable N:P scheme implemented in

951   our ocean biogeochemistry model allowed P_O to exhibit P flexibility as the ambient PO_4

952   concentration varies. The P flexibility has two important consequences. First, the P_O P limitation

953   is reduced, allowing them to grow more in low-PO_4 environments, fix more C there, and become

954   relatively more C-laden. Second, the P_O PO_4 frugalness stokes an ecological response via

955   increased PO_4 availability for P_{Diaz}, leading to an improved cohabitation between P_O and P_{Diaz},

956   more net N and C fixation, and higher net C EP. The first consequence describes how N:P

957   flexibility enhances the biological C pump's efficiency (i.e., more C export per P), and the

958   second, how it can strengthen of the biological C pump by supporting a larger primary producer

959   biomass. While the variable Si:N scheme did not show the same strong influence over the C

960   pump, it does showcase how realistic modeling of nutrient quota ratios may improve

961   representations of biogeochemical cycles.

962   The LGM experiments suggest that the new nutrient flexibility allows the formation of

963   diverse phytoplankton communities, more responsive and interactive ocean biogeochemical

964   cycles, and increased ocean carbon storage with lower pCO$_2$. Our results, in addition to other

965   studies, then suggest that the robustness of model performance in various climate states may

966   depend, at least in part, on capturing the variability of ocean primary producers and their

967   community structures. We find that capturing these attributes leads to 78 – 90 Pg more ocean

968   carbon storage, realized through both the DIC and DOC inventories, in the LGM ocean as

969   compared to fixed stoichiometry. We identify the DOC response as a significant but previously

970   overlooked C storage mechanism in this context. Increased ocean C storage, thus, causes pCO$_2$

971   to be 13 – 14 ppm lower in the VSMs. Variable stoichiometry may then explain a notable portion

972   of the pCO$_2$ difference between the PI and LGM climates while unveiling important mechanisms

973   within primary producer communities and biogeochemical cycles that partly define the ocean

974   carbon cycle.

Open Research

983   Model code is publicly accessible at https://github.com/fillmann/variable-stoichiometry. Model

984   output, initialization and forcing data, simulation control, and restart files are publicly available

985   at https://doi.org/10.5281/zenodo.8161356.

References

987   Aumont, O., Maier-Reimer, E., Blain, S., & Monfray, P. (2003). An ecosystem model of the
988   global ocean including Fe, Si, P colimitations: An ecosystem model of the world ocean.
989   *Global Biogeochemical Cycles*, *17*(2). https://doi.org/10.1029/2001GB001745
990   Barnola, J. M., Raynaud, D., Korotkevicht, Y. S., & Lorius, C. (1987). Vostok ice core provides
991   160,000-year record of atmospheric CO$_2$. *Nature*, 329(6138), 408–408.

Bauska, T. K., Joos, F., Mix, A. C., Roth, R., Ahn, J., & Brook, E. J. (2015). Links between atmospheric carbon dioxide, the land carbon reservoir and climate over the past millennium. *Nature Geoscience*, *8*(5), 383–387. https://doi.org/10.1038/ngeo2422

Bereiter, B., Eggleston, S., Schmitt, J., Nehrbass-Ahles, C., Stocker, T. F., Fischer, H., et al. (2015). Revision of the EPICA Dome C CO_2 record from 800 to 600 kyr before present: Analytical bias in the EDC CO2 record. *Geophysical Research Letters*, *42*(2), 542–549. https://doi.org/10.1002/2014GL061957

Bisson, K., Siegel, D. A., & DeVries, T. (2020). Diagnosing Mechanisms of Ocean Carbon Export in a Satellite-Based Food Web Model. *Frontiers in Marine Science*, *7*, 505. https://doi.org/10.3389/fmars.2020.00505

Bouttes, N., Paillard, D., Roche, D. M., Brovkin, V., & Bopp, L. (2011). Last Glacial Maximum CO_2 and $\delta^{13}C$ successfully reconciled. *Geophysical Research Letters*, *38*. https://doi.org/10.1029/2010GL044499

Boyd, P. W., & Trull, T. W. (2007). Understanding the export of biogenic particles in oceanic waters: Is there consensus? *Progress in Oceanography*, *72*(4), 276–312. https://doi.org/10.1016/j.pocean.2006.10.007

Brovkin, V., Ganopolski, A., Archer, D., & Rahmstorf, S. (2007). Lowering of glacial atmospheric CO_2 in response to changes in oceanic circulation and marine biogeochemistry. *Paleoceanography*, *22*(4). https://doi.org/10.1029/2006PA001380

Brzezinski, M.A., Pride, C. J., Franck, V. M., Sigman, D. M., Sarmiento, J. L., Matsumoto, K., et al. (2002). A switch from $Si(OH)_4$ to NO_3^- depletion in the glacial Southern Ocean. *Geophysical Research Letters*, *29*(12), 5–1–5–4. https://doi.org/10.1029/2001GL014349

Buchanan, P. J., Chase, Z., Matear, R. J., Phipps, S. J., & Bindoff, N. L. (2019a). Marine nitrogen fixers mediate a low latitude pathway for atmospheric CO_2 drawdown. *Nature Communications*, *10*(1), 4611. https://doi.org/10.1038/s41467-019-12549-z

Buchanan, P. J., Matear, R. J., Chase, Z., Phipps, S. J., & Bindoff, N. L. (2019b). Ocean carbon and nitrogen isotopes in CSIRO Mk3L-COAL version 1.0: A tool for palaeoceanographic research. *Geoscientific Model Development*, *12*(4), 1491–1523. https://doi.org/10.5194/gmd-12-1491-2019

Buchanan, P. J., Matear, R. J., Lenton, A., Phipps, S. J., Chase, Z., & Etheridge, D. M. (2016). The simulated climate of the Last Glacial Maximum and insights into the global marine carbon cycle. *Climate of the Past*, *12*(12), 2271–2295. https://doi.org/10.5194/cp-12-2271-2016

Capone, D. G., Burns, J. A., Montoya, J. P., Subramaniam, A., Mahaffey, C., Gunderson, T., et al. (2005). Nitrogen fixation by *Trichodesmium* spp.: An important source of new nitrogen to the tropical and subtropical North Atlantic Ocean *Global Biogeochemical Cycles*, *19*(2). https://doi.org/10.1029/2004GB002331

Ciais, P., Tagliabue, A., Cuntz, M., Bopp, L., Scholze, M., Hoffmann, et al. (2012). Large inert carbon pool in the terrestrial biosphere during the Last Glacial Maximum. *Nature Geoscience*, *5*(1), 74–79. https://doi.org/10.1038/ngeo1324

Clark, L. L., Ingall, E. D., & Benner, R. (1998). Marine phosphorus is selectively remineralized. *Nature*, *393*(6684), 426–426. https://doi.org/10.1038/30881

Conway, T. M., Wolff, E. W., Röthlisberger, R., Mulvaney, R., & Elderfield, H. E. (2015). Constraints on soluble aerosol iron flux to the Southern Ocean at the Last Glacial Maximum. *Nature Communications*, *6*(1), 7850. https://doi.org/10.1038/ncomms8850

Cox, P.M. (2001). Description of the "TRIFFID" dynamic global vegetation model. Hadley Centre, Met Office, UK. https://jules.jchmr.org/sites/default/files/HCTN_24.pdf

Du, J., Haley, B. A., & Mix, A. C. (2020). Evolution of the Global Overturning Circulation since the Last Glacial Maximum based on marine authigenic neodymium isotopes. *Quaternary Science Reviews*, *241*, 106396. https://doi.org/10.1016/j.quascirev.2020.106396

Egleston, E. S., Sabine, C. L., & Morel, F. M. M. (2010). Revelle revisited: Buffer factors that quantify the response of ocean chemistry to changes in DIC and alkalinity. *Global Biogeochemical Cycles*, *24*(1). https://doi.org/10.1029/2008GB003407

Falkowski, P. (2012). The power of plankton. *Nature*, *483*(7387), S17-S20

Field, C. B., Behrenfeld, M. J., Randerson, J. T., & Falkowski, P. (1998). Primary Production of the Biosphere: Integrating Terrestrial and Oceanic Components. *Science*, *281*(5374), 237–240. https://doi.org/10.1126/science.281.5374.237

Flynn, K. J. (2010). Ecological modelling in a sea of variable stoichiometry: Dysfunctionality and the legacy of Redfield and Monod. *Progress in Oceanography*, *84*(1–2), 52–65. https://doi.org/10.1016/j.pocean.2009.09.006

Franck, V. M., Brzezinski, M. A., Coale, K. H., & Nelson, D. M. (2000). Iron and silicic acid concentrations regulate Si uptake north and south of the Polar Frontal Zone in the Pacific Sector of the Southern Ocean. *Deep-Sea Research II*, *47*(15-16), 3315-3338. https://doi.org/10.1016/S0967-0645(00)00070-9

Galbraith, E. D., Gnanadesikan, A., Dunne, J. P., & Hiscock, M. R. (2010). Regional impacts of iron-light colimitation in a global biogeochemical model. *Biogeosciences*, *7*(3), 1043-1064. https://doi.org/10.5194/bg-7-1043-2010

Galbraith, E. D., Kienast, M., & The NICOPP working group members. (2013). The acceleration of oceanic denitrification during deglacial warming. *Nature Geoscience*, *6*(7), 579–584. https://doi.org/10.1038/ngeo1832

Galbraith, E. D., & Martiny, A. C. (2015). A simple nutrient-dependence mechanism for predicting the stoichiometry of marine ecosystems. *Proceedings of the National Academy of Sciences*, *112*(27), 8199–8204. https://doi.org/10.1073/pnas.1423917112

Galbraith, E. D., & Skinner, L. C. (2020). The Biological Pump During the Last Glacial Maximum. *Annual Review of Marine Science*, *12*(1), 559–586. https://doi.org/10.1146/annurev-marine-010419-010906

Garcia, C. A., Baer, S. E., Garcia, N. S., Rauschenberg, S., Twining, B. S., Lomas, M. W., & Martiny, A. C. (2018). Nutrient supply controls particulate elemental concentrations and ratios in the low latitude eastern Indian Ocean. *Nature Communications*, *9*(1), 4868. https://doi.org/10.1038/s41467-018-06892-w

Garcia, H. E., Locarnini, R. A., Boyer, T. P., Antonov, J. I., Baranova, O. K., Zweng, M. M., et al. (2013). World Ocean Atlas 2013. Volume 4, Dissolved inorganic nutrients (phosphate, nitrate, silicate). *NOAA Atlas NESDIS 76,* https://doi.org/10.7289/V5J67DWD

Garcia, N. S., Sexton, J., Riggins, T., Brown, J., Lomas, M. W., & Martiny, A. C. (2018). High Variability in Cellular Stoichiometry of Carbon, Nitrogen, and Phosphorus Within Classes of Marine Eukaryotic Phytoplankton Under Sufficient Nutrient Conditions. *Frontiers in Microbiology*, *9*, 543. https://doi.org/10.3389/fmicb.2018.00543

Geider, R., & La Roche, J. (2002). Redfield revisited: Variability of C:N:P in marine microalgae and its biochemical basis. *European Journal of Phycology*, *37*(1), 1–17. https://doi.org/10.1017/S0967026201003456

1082 Gerhart, L. M., & Ward, J. K. (2010). Plant responses to low [CO_2] of the past. *New Phytologist*,
1083   *188*(3), 674–695. https://doi.org/10.1111/j.1469-8137.2010.03441.x
1084 Gregg, W. W., & Casey, N. W. (2007). Modeling coccolithophores in the global oceans. *Deep*
1085   *Sea Research Part II: Topical Studies in Oceanography*, *54*(5–7), 447–477.
1086   https://doi.org/10.1016/j.dsr2.2006.12.007
1087 Großkopf, T., & LaRoche, J. (2012). Direct and indirect costs of dinitrogen fixation in
1088   *Crocosphaera watsonii* WH8501 and possible implications for the nitrogen cycle.
1089   *Frontiers in Microbiology*, *3*. https://doi.org/10.3389/fmicb.2012.00236
1090 Gruber, N., & Sarmiento, J. L. (1997). Global patterns of marine nitrogen fixation and
1091   denitrification. *Global Biogeochemical Cycles*, *11*(2), 235–266.
1092   https://doi.org/10.1029/97GB00077
1093 Harrison, S. P., & Prentice, C. I. (2003). Climate and CO_2 controls on global vegetation
1094   distribution at the last glacial maximum: Analysis based on palaeovegetation data, biome
1095   modelling and palaeoclimate simulations. *Global Change Biology*, *9*(7), 983–1004.
1096   https://doi.org/10.1046/j.1365-2486.2003.00640.x
1097 Hildebrand, M., & Lerch, S. J. L. (2015). Diatom silica biomineralization: Parallel development
1098   of approaches and understanding. *Seminars in Cell & Developmental Biology*, *46*, 27–35.
1099   https://doi.org/10.1016/j.semcdb.2015.06.007
1100 Ho, P., Chang, C., Shiah, F., Wang, P., Hsieh, C., & Andersen, K. H. (2020). Body Size, Light
1101   Intensity, and Nutrient Supply Determine Plankton Stoichiometry in Mixotrophic
1102   Plankton Food Webs. *The American Naturalist*, *195*(4), E100–E111.
1103   https://doi.org/10.1086/707394
1104 Holzer, M., Pasquier, B., DeVries, T., & Brzezinski, M. A. (2019). Diatom physiology controls
1105   silicic acid leakage in response to iron fertilization. *Global Biogeochemical Cycles*,
1106   33(12), 1631– 1653. https://doi.org/10.1029/2019GB006460
1107 Houghton, R. A. (2007). Balancing the Global Carbon Budget. *Annual Review of Earth and*
1108   *Planetary Sciences*, *35*(1), 313–347.
1109   https://doi.org/10.1146/annurev.earth.35.031306.140057
1110 Hutchins, D. A., & Bruland, K. W. (1998). Iron-limited diatom growth and Si:N uptake ratios in
1111   a coastal upwelling regime. *Nature*, *393*(6685), 561–564. https://doi.org/10.1038/31203
1112 Inomura, K., Deutsch, C., Jahn, O., Dutkiewicz, S., & Follows, M. J. (2022). Global patterns in
1113   marine organic matter stoichiometry driven by phytoplankton ecophysiology. *Nature*
1114   *Geoscience*, *15*(12), 1034–1040. https://doi.org/10.1038/s41561-022-01066-2
1115 Ivanovic, R. F., Gregoire, L. J., Kageyama, M., Roche, D. M., Valdes, P. J., Burke, A., et al.
1116   (2016). Transient climate simulations of the deglaciation 21–9 thousand years before
1117   present (version 1) – PMIP4 Core experiment design and boundary conditions.
1118   *Geoscientific Model Development*, *9*(7), 2563–2587. https://doi.org/10.5194/gmd-9-2563-
1119   2016
1120 Jaccard, S. L., & Galbraith, E. D. (2012). Large climate-driven changes of oceanic oxygen
1121   concentrations during the last deglaciation. *Nature Geoscience*, *5*(2), 151–156.
1122   https://doi.org/10.1038/ngeo1352
1123 Jeltsch-Thommes, A., Battaglia, G., Cartapanis, O., Jaccard, S. L., & Joos, F. (2019). Low
1124   terrestrial carbon storage at the Last Glacial Maximum: constraints from multi-proxy
1125   data. *Climate of the Past*, *15*(2), 849–879. https://doi.org/10.5194/cp-15-849-2019
1126 Jiao, N., Herndl, G. J., Hansell, D. A., Benner, R., Kattner, G., Wilhelm, S. W., et al. (2010).
1127   Microbial production of recalcitrant dissolved organic matter: Long-term carbon storage

1128   in the global ocean. *Nature Reviews Microbiology*, *8*(8), 593–599.
1129   https://doi.org/10.1038/nrmicro2386
1130 Kageyama, M., Albani, S., Braconnot, P., Harrison, S. P., Hopcroft, P. O., Ivanovic, R. F., et al.
1131   (2017). The PMIP4 contribution to CMIP6 – Part 4: Scientific objectives and
1132   experimental design of the PMIP4-CMIP6 Last Glacial Maximum experiments and
1133   PMIP4 sensitivity experiments. *Geoscientific Model Development*, *10*(11), 4035–4055.
1134   https://doi.org/10.5194/gmd-10-4035-2017
1135 Khatiwala, S., Schmittner, A., & Muglia, J. (2019). Air-sea disequilibrium enhances ocean
1136   carbon storage during glacial periods. *Science Advances*, *5*(6), eaaw4981.
1137   https://doi.org/10.1126/sciadv.aaw4981
1138 Klausmeier, C. A., Litchman, E., & Levin, S. A. (2004). Phytoplankton growth and
1139   stoichiometry under multiple nutrient limitation. *Limnology and Oceanography*, *49*(4,
1140   part2), 1463–1470. https://doi.org/10.4319/lo.2004.49.4_part_2.1463
1141 Kohfeld, K. E., Quéré, C. L., Harrison, S. P., & Anderson, R. F. (2005). Role of Marine Biology
1142   in Glacial-Interglacial CO $_2$ Cycles. *Science*, *308*(5718), 74–78.
1143   https://doi.org/10.1126/science.1105375
1144 Kvale, K. F., Meissner, K. J., Keller, D. P., Eby, M., & Schmittner, A. (2015). Explicit Planktic
1145   Calcifiers in the University of Victoria Earth System Climate Model, Version 2.9.
1146   *Atmosphere-Ocean*, *53*(3), 332–350. https://doi.org/10.1080/07055900.2015.1049112
1147 Kvale, K., Keller, D. P., Koeve, W., Meissner, K. J., Somes, C. J., Yao, W., & Oschlies, A.
1148   (2021). Explicit silicate cycling in the Kiel Marine Biogeochemistry Model version 3
1149   (KMBM3) embedded in the UVic ESCM version 2.9. *Geoscientific Model Development*,
1150   *14*(12), 7255–7285. https://doi.org/10.5194/gmd-14-7255-2021
1151 Lafond, A., Leblanc, K., Legras, J., Cornet, V., & Quéguiner, B. (2020). The structure of diatom
1152   communities constrains biogeochemical properties in surface waters of the Southern
1153   Ocean (Kerguelen Plateau). *Journal of Marine Systems*, *212*, 103458.
1154   https://doi.org/10.1016/j.jmarsys.2020.103458
1155 Lambeck, K., Rouby, H., Purcell, A., Sun, Y., & Sambridge, M. (2014). Sea level and global ice
1156   volumes from the Last Glacial Maximum to the Holocene. *Proceedings of the National
1157   Academy of Sciences*, *111*(43), 15296–15303. https://doi.org/10.1073/pnas.1411762111
1158 Lambert, F., Tagliabue, A., Shaffer, G., Lamy, F., Winckler, G., Farias, L., et al. (2015). Dust
1159   fluxes and iron fertilization in Holocene and Last Glacial Maximum climates.
1160   *Geophysical Research Letters*, *42*(14), 6014–6023.
1161   https://doi.org/10.1002/2015GL064250
1162 Letscher, R. T., Hansell, D. A., Carlson, C. A., Lumpkin, R., & Knapp, A. N. (2013). Dissolved
1163   organic nitrogen in the global surface ocean: Distribution and fate. *Global
1164   Biogeochemical Cycles*, *27*(1), 141–153. https://doi.org/10.1029/2012GB004449
1165 Liefer, J. D., Garg, A., Fyfe, M. H., Irwin, A. J., Benner, I., Brown, C. M., et al. (2019). The
1166   macromolecular basis of phytoplankton C:N:P under nitrogen starvation. *Frontiers in
1167   Microbiology*, *10*, 763. https://doi.org/10.3389/fmicb.2019.00763
1168 Lønborg, C., Carreira, C., Jickells, T., & Álvarez-Salgado, X. A. (2020). Impacts of global
1169   change on ocean dissolved organic carbon (DOC) cycling. *Frontiers in Marine Science*,
1170   *7*, 466. https://doi.org/10.3389/fmars.2020.00466
1171 Lüthi, D., Le Floch, M., Bereiter, B., Blunier, T., Barnola, J.-M., Siegenthaler, U., et al. (2008).
1172   High-resolution carbon dioxide concentration record 650,000–800,000 years before
1173   present. *Nature*, *453*(7193), 379–382. https://doi.org/10.1038/nature06949

Marcott, S. A., Bauska, T. K., Buizert, C., Steig, E. J., Rosen, J. L., Cuffey, K. M., et al. (2014). Centennial-scale changes in the global carbon cycle during the last deglaciation. *Nature*, *514*(7524), 616–619. https://doi.org/10.1038/nature13799

Martiny, A. C., Pham, C. T. A., Primeau, F. W., Vrugt, J. A., Moore, J. K., Levin, S. A., & Lomas, M. W. (2013). Strong latitudinal patterns in the elemental ratios of marine plankton and organic matter. *Nature Geoscience*, *6*(4), 279–283. https://doi.org/10.1038/ngeo1757

Mather, R. L., Reynolds, S. E., Wolff, G. A., Williams, R. G., Torres-Valdes, S., Woodward, E. M. S., et al. (2008). Phosphorus cycling in the North and South Atlantic Ocean subtropical gyres. *Nature Geoscience*, *1*(7), 439–443. https://doi.org/10.1038/ngeo232

Matsumoto, K. (2007). Biology-mediated temperature control on atmospheric pCO$_2$ and ocean biogeochemistry. *Geophysical Research Letters*, *34*(20), L20605. https://doi.org/10.1029/2007GL031301

Matsumoto, K., Chase, Z., & Kohfeld, K. (2014). Different mechanisms of silicic acid leakage and their biogeochemical consequences. *Paleoceanography*, *29*(3), 238–254. https://doi.org/10.1002/2013PA002588

Matsumoto, K., Rickaby, R., & Tanioka, T. (2020). Carbon export buffering and CO$_2$ drawdown by flexible phytoplankton C:N:P under glacial conditions. *Paleoceanography and Paleoclimatology*, *35*(7). https://doi.org/10.1029/2019PA003823

Matsumoto, K., Tokos, K., Huston, A., & Joy-Warren, H. (2013). MESMO 2: a mechanistic marine silica cycle and coupling to a simple terrestrial scheme. *Geoscientific Model Development*, *6*(2), 477–494. https://doi.org/10.5194/gmd-6-477-2013

McKinley, G. A., Fay, A. R., Lovenduski, N. S., & Pilcher, D. J. (2017). Natural variability and anthropogenic trends in the ocean carbon sink. *Annual Review of Marine Science*, *9*(1), 125–150. https://doi.org/10.1146/annurev-marine-010816-060529

Meissner, K. J., Weaver, A. J., Matthews, H. D., & Cox, P. M. (2003). The role of land surface dynamics in glacial inception: A study with the UVic Earth System Model. *Climate Dynamics*, *21*(7–8), 515–537. https://doi.org/10.1007/s00382-003-0352-2

Mengis, N., Keller, D. P., MacDougall, A. H., Eby, M., Wright, N., Meissner, K. J., et al. (2020). Evaluation of the University of Victoria Earth System Climate Model version 2.10 (UVic ESCM 2.10). *Geoscientific Model Development*, *13*(9), 4183–4204. https://doi.org/10.5194/gmd-13-4183-2020

Meyer, J., Löscher, C. R., Neulinger, S. C., Reichel, A. F., Loginova, A., Borchard, C., et al. (2016). Changing nutrient stoichiometry affects phytoplankton production, DOP accumulation and dinitrogen fixation – a mesocosm experiment in the eastern tropical North Atlantic. *Biogeosciences*, *13*(3), 781–794. https://doi.org/10.5194/bg-13-781-2016

Meyerink, S. W., Ellwood, M. J., Maher, W. A., Dean Price, G., & Strzepek, R. F. (2017). Effects of iron limitation on silicon uptake kinetics and elemental stoichiometry in two Southern Ocean diatoms, *Eucampia antarctica* and *Proboscia inermis* , and the temperate diatom *Thalassiosira pseudonana*. *Limnology and Oceanography*, *62*(6), 2445–2462. https://doi.org/10.1002/lno.10578

Microsoft Corporation. (2018). Microsoft Powerpoint. Retrieved from https://office.microsoft.com/powerpoint

Mills, M. M., & Arrigo, K. R. (2010). Magnitude of oceanic nitrogen fixation influenced by the nutrient uptake ratio of phytoplankton. *Nature Geoscience*, *3*(6), 412–416. https://doi.org/10.1038/ngeo856

Monteiro, F. M., & Follows, M. J. (2012). On nitrogen fixation and preferential remineralization of phosphorus. *Geophysical Research Letters*, *39*(6), L06607. https://doi.org/10.1029/2012GL050897

Moore, C. M., Mills, M. M., Arrigo, K. R., Berman-Frank, I., Bopp, L., Boyd, P. W., et al. (2013). Processes and patterns of oceanic nutrient limitation. *Nature Geoscience*, *6*(9), 701–710. https://doi.org/10.1038/ngeo1765

Moore, J. K., Doney, S. C., & Lindsay, K. (2004). Upper ocean ecosystem dynamics and iron cycling in a global three-dimensional model. *Global Biogeochemical Cycles*, *18*(4), GB4028. https://doi.org/10.1029/2004GB002220

Moreno, A. R., Hagstrom, G. I., Primeau, F. W., Levin, S. A., & Martiny, A. C. (2018). Marine phytoplankton stoichiometry mediates nonlinear interactions between nutrient supply, temperature, and atmospheric CO_2; *Biogeosciences*, *15*(9), 2761–2779. https://doi.org/10.5194/bg-15-2761-2018

Moreno, A. R., & Martiny, A. C. (2018). Ecological stoichiometry of ocean plankton. *Annual Review of Marine Science*, *10*(1), 43–69. https://doi.org/10.1146/annurev-marine-121916-063126

Muglia, J., & Schmittner, A. (2015). Glacial atlantic overturning increased by wind stress in climate models. *Geophysical Research Letters*, *42*(22), 9862–9868. https://doi.org/10.1002/2015GL064583

Muglia, J., Skinner, L. C., & Schmittner, A. (2018). Weak overturning circulation and high Southern Ocean nutrient utilization maximized glacial ocean carbon. *Earth and Planetary Science Letters*, *496*, 47–56. https://doi.org/10.1016/j.epsl.2018.05.038

Muglia, J., Somes, C. J., Nickelsen, L., & Schmittner, A. (2017). Combined effects of atmospheric and seafloor iron fluxes to the glacial ocean. *Paleoceanography*, *32*(11), 1204–1218. https://doi.org/10.1002/2016PA003077

Nowicki, M., DeVries, T., & Siegel, D. A. (2022). Quantifying the carbon export and sequestration pathways of the ocean's biological carbon pump. *Global Biogeochemical Cycles*, *36*(3). https://doi.org/10.1029/2021GB007083

Ödalen, M., Nycander, J., Ridgwell, A., Oliver, K. I. C., Peterson, C. D., & Nilsson, J. (2020). Variable C∕P composition of organic production and its effect on ocean carbon storage in glacial-like model simulations. *Biogeosciences*, *17*(8), 2219–2244. https://doi.org/10.5194/bg-17-2219-2020

Pahlow, M., Chien, C.-T., Arteaga, L. A., & Oschlies, A. (2020). Optimality-based non-Redfield plankton–ecosystem model (OPEM v1.1) in UVic-ESCM 2.9 – Part 1: Implementation and model behaviour. *Geoscientific Model Development*, *13*(10), 4663–4690. https://doi.org/10.5194/gmd-13-4663-2020

Peltier, W. R., Argus, D. F., & Drummond, R. (2015). Space geodesy constrains ice age terminal deglaciation: The global ICE-6G_C (VM5a) model. *Journal of Geophysical Research: Solid Earth*, *120*(1), 450–487. https://doi.org/10.1002/2014JB011176

Petit, J. R., Jouzel, J., Raynaud, D., Barkov, N. I., Delaygue, G., Delmotte, M., et al. (1999). Climate and atmospheric history of the past 420,000 years from the Vostok ice core, Antarctica. *Nature*, *399*, 429-436.

Prentice, I. C., Harrison, S. P., & Bartlein, P. J. (2011). Global vegetation and terrestrial carbon cycle changes after the last ice age. *New Phytologist*, *189*(4), 988–998. https://doi.org/10.1111/j.1469-8137.2010.03620.x

Ramaswamy, V., Chanin, M.-L., Angell, J., Barnett, J., Gaffen, D., Gelman, M., et al. (2001). Stratospheric temperature trends: Observations and model simulations. *Reviews of Geophysics*, *39*(1), 71–122. https://doi.org/10.1029/1999RG000065

Redfield, A.C. (1934) On the Proportions of Organic Derivatives in Sea Water and Their Relation to the Composition of Plankton. *James Johnstone Memorial Volume, University Press of Liverpool*, 176-192.

Redfield, A.C. (1958) The Biological Control of Chemical Factors in the Environment. *American Scientist*, 46, 205-221.

Sañudo-Wilhelmy, S. A., Tovar-Sanchez, A., Fu, F.X., Capone, D. G., Carpenter, E. J., & Hutchins, D. A. (2004). The impact of surface-adsorbed phosphorus on phytoplankton Redfield stoichiometry. *Nature*, *432*(7019), 897–901. https://doi.org/10.1038/nature03125

Sarmiento, J. L., & Gruber, N. (2006). *Ocean Biogeochemical Dynamics*. Princeton University Press.

Schmittner, A., Gruber, N., Mix, A. C., Key, R. M., Tagliabue, A., & Westberry, T. K. (2013). Biology and air–sea gas exchange controls on the distribution of carbon isotope ratios ($\delta^{13}C$) in the ocean. *Biogeosciences*, *10*(9), 5793–5816. https://doi.org/10.5194/bg-10-5793-2013

Schmittner, A., & Somes, C. J. (2016). Complementary constraints from carbon (^{13}C) and nitrogen (^{15}N) isotopes on the glacial ocean's soft-tissue biological pump. *Paleoceanography*, *31*(6), 669–693. https://doi.org/10.1002/2015PA002905

Séférian, R., Berthet, S., Yool, A., Palmiéri, J., Bopp, L., Tagliabue, A., et al. (2020). Tracking improvement in simulated marine biogeochemistry between CMIP5 and CMIP6. *Current Climate Change Reports*, *6*(3), 95–119. https://doi.org/10.1007/s40641-020-00160-0

Sigman, D. M., Hain, M. P., & Haug, G. H. (2010). The polar ocean and glacial cycles in atmospheric CO2 concentration. *Nature*, *466*(7302), 47–55. https://doi.org/10.1038/nature09149

Somes, C. J., & Oschlies, A. (2015). On the influence of "non-Redfield" dissolved organic nutrient dynamics on the spatial distribution of N_2 fixation and the size of the marine fixed nitrogen inventory. *Global Biogeochemical Cycles*, *29*(7), 973–993. https://doi.org/10.1002/2014GB005050

Somes, C. J., Schmittner, A., Galbraith, E. D., Lehmann, M. F., Altabet, M. A., Montoya, J. P., et al. (2010). Simulating the global distribution of nitrogen isotopes in the ocean. *Global Biogeochemical Cycles*, *24*(4), GB4019. https://doi.org/10.1029/2009GB003767

Somes, C. J., Schmittner, A., Muglia, J., & Oschlies, A. (2017). A Three-Dimensional Model of the Marine Nitrogen Cycle during the Last Glacial Maximum Constrained by Sedimentary Isotopes. *Frontiers in Marine Science*, 4. https://doi.org/10.3389/fmars.2017.00108

Tagliabue, A., Bopp, L., Roche, D. M., Bouttes, N., & Paillard, D. (2009). Quantifying the roles of ocean circulation and biogeochemistry in governing ocean carbon-13 and atmospheric carbon dioxide at the last glacial maximum. *Clim. Past*, *5,* 695 - 706, https://doi.org/10.5194/cp-5-695-2009

Takeda, S. (1998). Influence of iron availability on nutrient consumption ratio of diatoms in oceanic waters. *Nature*, *393*(6687), 774–777. https://doi.org/10.1038/31674

Tanioka, T., & Matsumoto, K. (2017). Buffering of ocean export production by flexible elemental stoichiometry of particulate organic matter. *Global Biogeochemical Cycles*, *31*(10), 1528–1542. https://doi.org/10.1002/2017GB005670

Tanioka, T., & Matsumoto, K. (2020). A meta-analysis on environmental drivers of marine phytoplankton C:N:P. *Biogeosciences*, *17*(11), 2939–2954. https://doi.org/10.5194/bg-17-2939-2020

Taylor, K.E. (2001). Summarizing multiple aspects of model performance in a single diagram. *Journal of Geophysical Research. D. Atmospheres*, *106*(D7), 7183–7192. https://doi.org/10.1029/2000JD900719

Tesdal, Galbraith, E. D., & Kienast, M. (2013). Nitrogen isotopes in bulk marine sediment: linking seafloor observations with subseafloor records. *Biogeosciences*, *10*(1), 101–118. https://doi.org/10.5194/bg-10-101-2013

Tierney, J. E., Poulsen, C. J., Montañez, I. P., Bhattacharya, T., Feng, R., Ford, H. L., et al. (2020). Past climates inform our future. *Science*, *370*(6517), aay3701. https://doi.org/10.1126/science.aay3701

Toggweiler, J. R. (1999). Variation of atmospheric CO_2 by ventilation of the ocean's deepest water. *Paleoceanography*, *14*(5), 571–588. https://doi.org/10.1029/1999PA900033

Tyrrell, T. (1999). The relative influences of nitrogen and phosphorus on oceanic primary production. *Nature*, *400*, 525-531.

Volk, T., & Hoffert, M. I. (1985). Ocean carbon pumps: analysis of relative strengths and efficiencies in ocean-driven atmospheric CO_2 changes. In E. T. Sundquist & W. S. Broecker (Eds.), *Geophysical Monograph Series* (pp. 99–110). American Geophysical Union. https://doi.org/10.1029/GM032p0099

Wagner, S., Schubotz, F., Kaiser, K., Hallmann, C., Waska, H., Rossel., et al. (2020). Soothsaying DOM: A current perspective on the future of oceanic dissolved organic carbon. *Frontiers in Marine Science*, *7*, 341. https://doi.org/10.3389/fmars.2020.00341

Ward, B. A., Dutkiewicz, S., Moore, C. M., & Follows, M. J. (2013). Iron, phosphorus, and nitrogen supply ratios define the biogeography of nitrogen fixation. *Limnology and Oceanography*, *58*(6), 2059–2075. https://doi.org/10.4319/lo.2013.58.6.2059

Weaver, A. J., Eby, M., Wiebe, E. C., Bitz, C. M., Duffy, P. B., Ewen, T. L., et al. (2001). The UVic earth system climate model: Model description, climatology, and applications to past, present and future climates. *Atmosphere-Ocean*, *39*(4), 361–428. https://doi.org/10.1080/07055900.2001.9649686

Weber, T. S., & Deutsch, C. (2010). Ocean nutrient ratios governed by plankton biogeography. *Nature*, *467*(7315), 550–554. https://doi.org/10.1038/nature09403

White, A. E., Spitz, Y. H., Karl, D. M., & Letelier, R. M. (2006). Flexible elemental stoichiometry in *Trichodesmium* spp. and its ecological implications. *Limnology and Oceanography*, *51*(4), 1777–1790. https://doi.org/10.4319/lo.2006.51.4.1777

Williams, P. M., & Druffel, E. R. M. (1987). Radiocarbon in dissolved organic matter in the central North Pacific Ocean. *Nature*, *330*(6145), 246–248. https://doi.org/10.1038/330246a0

Wu, J., Sunda, W., Boyle, E. A., & Karl, D. M. (2000). Phosphate depletion in the western North Atlantic Ocean. *Science*, *289*(5480), 759–762. https://doi.org/10.1126/science.289.5480.759

Yvon-Durocher, G., Jones, J. I., Trimmer, M., Woodward, G., & Montoya, J. M. (2010). Warming alters the metabolic balance of ecosystems. *Phil. Trans. R. Soc. B*, *365*(1549), 2117–2126. https://doi.org/10.1098/rstb.2010.0038

Zeng, N. (2003). Glacial-interglacial atmospheric CO2 change—The glacial burial hypothesis. *Advances in Atmospheric Sciences*, *20*(5), 677–693. https://doi.org/10.1007/BF02915395

Zúñiga, D., Sanchez-Vidal, A., Flexas, M. M., Carroll, D., Rufino, M. M., Spreen, G., et al. (2021). Sinking diatom assemblages as a key driver for deep carbon and silicon export in the Scotia Sea (Southern Ocean). *Front. Earth Sci.*, *9*, 579198. https://doi.org/10.3389/feart.2021.579198

References from the Supporting Information

Buchanan, P. J., Matear, R. J., Chase, Z., Phipps, S. J., & Bindoff, N. L. (2019). Ocean carbon and nitrogen isotopes in CSIRO Mk3L-COAL version 1.0: A tool for palaeoceanographic research. *Geoscientific Model Development*, *12*(4), 1491–1523. https://doi.org/10.5194/gmd-12-1491-2019

Galbraith, E. D., Gnanadesikan, A., Dunne, J. P., & Hiscock, M. R. (2010). Regional impacts of iron-light colimitation in a global biogeochemical model. *Biogeosciences*, 7(3), 1043-1064. https://doi.org/10.5194/bg-7-1043-2010

Galbraith, E. D., Kienast, M., & The NICOPP working group members. (2013). The acceleration of oceanic denitrification during deglacial warming. *Nature Geoscience*, *6*(7), 579–584. https://doi.org/10.1038/ngeo1832

Galbraith, E. D., & Martiny, A. C. (2015). A simple nutrient-dependence mechanism for predicting the stoichiometry of marine ecosystems. *Proceedings of the National Academy of Sciences*, *112*(27), 8199–8204. https://doi.org/10.1073/pnas.1423917112

Garcia, H. E., Locarnini, R. A., Boyer, T. P., Antonov, J. I., Baranova, O. K., Zweng, M. M., et al. (2013). World ocean atlas 2013. Volume 4, Dissolved inorganic nutrients (phosphate, nitrate, silicate). *NOAA Atlas NESDIS 76* https://doi.org/10.7289/V5J67DWD

Gruber, N., & Sarmiento, J. L. (1997). Global patterns of marine nitrogen fixation and denitrification. *Global Biogeochemical Cycles*, *11*(2), 235–266. https://doi.org/10.1029/97GB00077

Lambeck, K., Rouby, H., Purcell, A., Sun, Y., & Sambridge, M. (2014). Sea level and global ice volumes from the Last Glacial Maximum to the Holocene. *Proceedings of the National Academy of Sciences*, *111*(43), 15296–15303. https://doi.org/10.1073/pnas.1411762111

Letscher, R. T., Hansell, D. A., Carlson, C. A., Lumpkin, R., & Knapp, A. N. (2013). Dissolved organic nitrogen in the global surface ocean: Distribution and fate. *Global Biogeochemical Cycles*, *27*(1), 141–153. https://doi.org/10.1029/2012GB004449

Mather, R. L., Reynolds, S. E., Wolff, G. A., Williams, R. G., Torres-Valdes, S., Woodward, E. M. S., et al. (2008). Phosphorus cycling in the North and South Atlantic Ocean subtropical gyres. *Nature Geoscience*, *1*(7), 439–443. https://doi.org/10.1038/ngeo232

Muglia, J., Skinner, L. C., & Schmittner, A. (2018). Weak overturning circulation and high Southern Ocean nutrient utilization maximized glacial ocean carbon. *Earth and Planetary Science Letters*, *496*, 47–56. https://doi.org/10.1016/j.epsl.2018.05.038

Muglia, J., Somes, C. J., Nickelsen, L., & Schmittner, A. (2017). Combined Effects of Atmospheric and Seafloor Iron Fluxes to the Glacial Ocean. *Paleoceanography*, *32*(11), 1204–1218. https://doi.org/10.1002/2016PA003077

1397   Sarmiento, J. L., & Gruber, N. (2006). *Ocean biogeochemical dynamics*. Princeton University
1398   Press.
1399   Schmittner, A., & Somes, C. J. (2016). Complementary constraints from carbon (^{13}C) and
1400   nitrogen (^{15}N) isotopes on the glacial ocean's soft-tissue biological pump.
1401   *Paleoceanography*, *31*(6), 669–693. https://doi.org/10.1002/2015PA002905
1402   Somes, C. J., & Oschlies, A. (2015). On the influence of "non-Redfield" dissolved organic
1403   nutrient dynamics on the spatial distribution of N_2 fixation and the size of the marine
1404   fixed nitrogen inventory. *Global Biogeochemical Cycles*, *29*(7), 973–993.
1405   https://doi.org/10.1002/2014GB005050
1406   Somes, C. J., Schmittner, A., Galbraith, E. D., Lehmann, M. F., Altabet, M. A., Montoya, J. P., et
1407   al. (2010). Simulating the global distribution of nitrogen isotopes in the ocean. *Global
1408   Biogeochemical Cycles*, *24*(4). https://doi.org/10.1029/2009GB003767
1409   Tagliabue, A., Bopp, L., Roche, D. M., Bouttes, N., & Paillard, D. (2009). Quantifying the roles
1410   of ocean circulation and biogeochemistry in governing ocean carbon-13 and atmospheric
1411   carbon dioxide at the last glacial maximum. *Clim. Past*, *5,* 695 - 706,
1412   https://doi.org/10.5194/cp-5-695-2009
1413   Tesdal, Galbraith, E. D., & Kienast, M. (2013). Nitrogen isotopes in bulk marine sediment:
1414   linking seafloor observations with subseafloor records. *Biogeosciences*, *10*(1), 101–118.
1415   https://doi.org/10.5194/bg-10-101-2013

Supporting Information for

Variable Stoichiometry Effects on Glacial/Interglacial Ocean Model Biogeochemical Cycles and Carbon Storage

Nathaniel J. Fillman[1], Andreas Schmittner[1], and Karin F. Kvale[2]

[1]College of Earth, Ocean, and Atmospheric Sciences, Oregon State University, Corvallis, OR, USA.
[2]Environmental Processes and Modelling, GNS Science, Lower Hutt, New Zealand.

Contents of this file

Introduction

We provide, here, further model validation and performance analysis against observed ocean biogeochemical datasets (Text S1, Figure S1–S7, and Table S1). Text S2 (Figures S8-S13 and Table S2) provides necessary model outputs to support and evidence statements made in the main text. Text S3 presents explicit modeled carbon inventory quantifications and distributions (Figures S14-S18 and Tables S3-S5), while further exploring the diatom model effects on ocean carbon stocks in Text S3.1. Text S4 explores the sensitivity of selected variable stoichiometry models to tertiary simulated biogeochemical processes (Figure S19 and Table S6). Text S5 compares simulated nitrogen isotopes to observed preindustrial and Last Glacial Maxima datasets (Figures S20-S25, Table S7). Lastly, Text S6 describes the relevant biogeochemical equations implemented or altered in the model (University of Victoria, Earth System Climate Model – Model of Ocean Biogeochemistry and Isotopes) for the variable stoichiometry configuration (Table S8).

Text S1. Variable Stoichiometry and Nutrient Simulations

S1.1: Statistical Performance of Simulated Surface Nutrients

　　Table S1 summarizes statistical metrics of the simulated nutrient distributions relative to observed data from the World Ocean Atlas, 2013 (Garcia et al., 2013; Letscher et al., 2013; Mather et al., 2008). R is the correlation coefficient; the *Tuned* experiment, here, generally outperforms all other simulations except for NO_3 where it is slightly less accurate than the *Control*. STDR expresses the ratio of standard deviations of the model data to observations measuring how well the model captures the natural variability. The *Tuned* model again performs the best comprehensively, except with the PO_4 simulations. Here, all model configurations struggle with the *Control* simulation capturing the variance best. However, out of the three variable stoichiometry model (VSM) configurations, the *Tuned* model is the most accurate. RMSE is the uncertainty-corrected root mean square error where the *Tuned* model configuration has the smallest error, but it is approximately matched by the *Control* experiment in the NO_3 simulations. Lastly, the RMS Prime is essentially the same as the RMSE but the bias of the global means of the observations and the models have been removed. The RMS Prime values are all exceedingly similar to the RMSE indicating the model global averages are all similar to the observed global mean. These statistical calculation methods were developed and described in Muglia et al. (2018).

Table S1. PI Surface (0-120 m) Nutrient Statistical Assessment.

NO_3	R	STDR	RMS prime	RMSE
Control	0.89	0.96	0.46	0.49
VarP:N	0.86	1.12	0.58	0.58
VarSi:N	0.86	1.17	0.60	0.60
Tuned	0.89	1.02	0.48	0.49
PO_4	R	STDR	RMS prime	RMSE
Control	0.89	0.92	0.45	0.48
VarP:N	0.89	0.86	0.46	0.55
VarSi:N	0.89	0.85	0.46	0.54
Tuned	0.90	0.89	0.44	0.48
Si	R	STDR	RMS prime	RMSE
Control	0.86	1.27	0.64	0.66
VarP:N	0.87	1.25	0.63	0.64
VarSi:N	0.90	1.00	0.44	0.47
Tuned	0.91	0.99	0.43	0.47

S1.2: Global Maps of Surface Nutrients
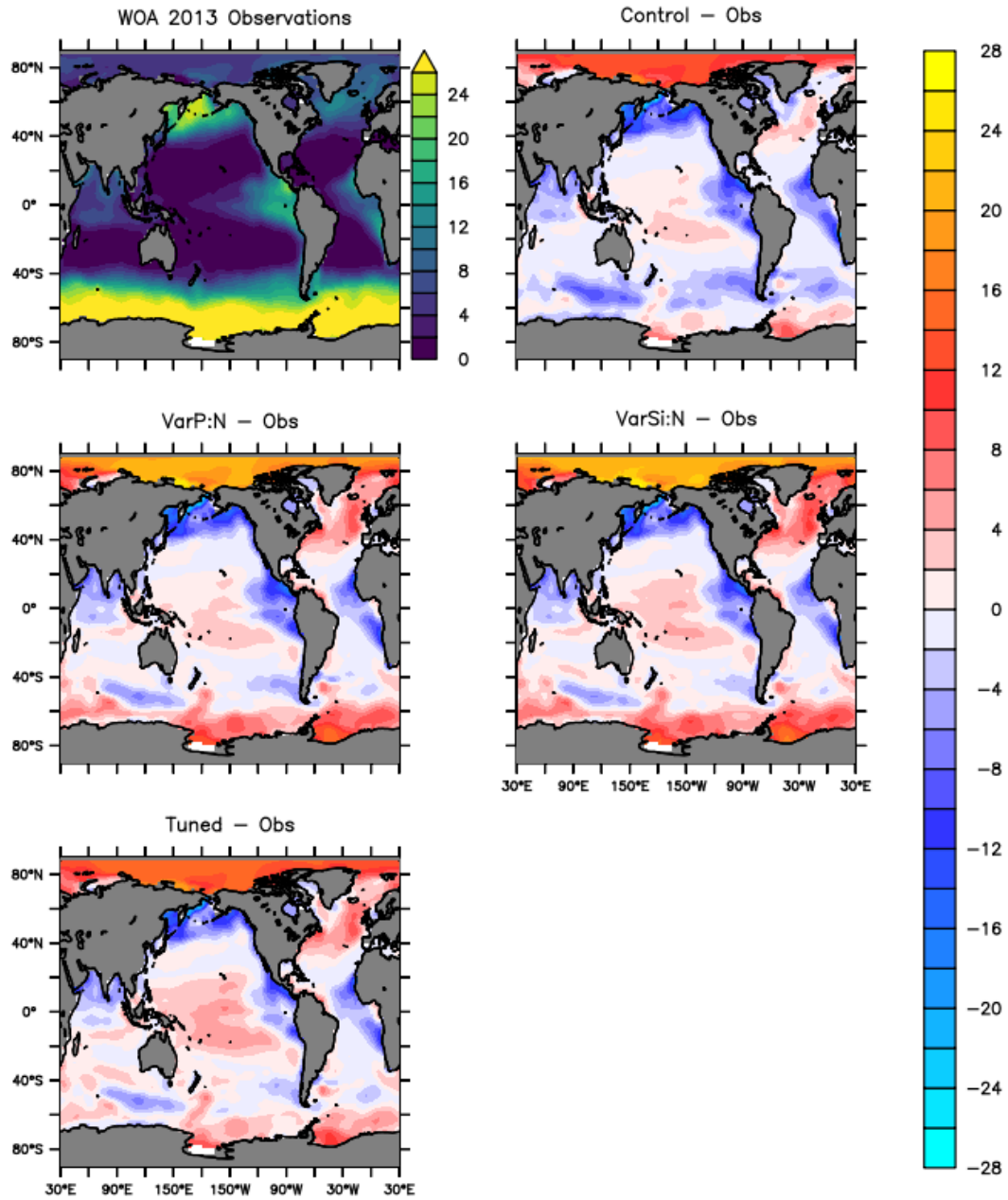
Figure S1. Surface Nitrate comparison.
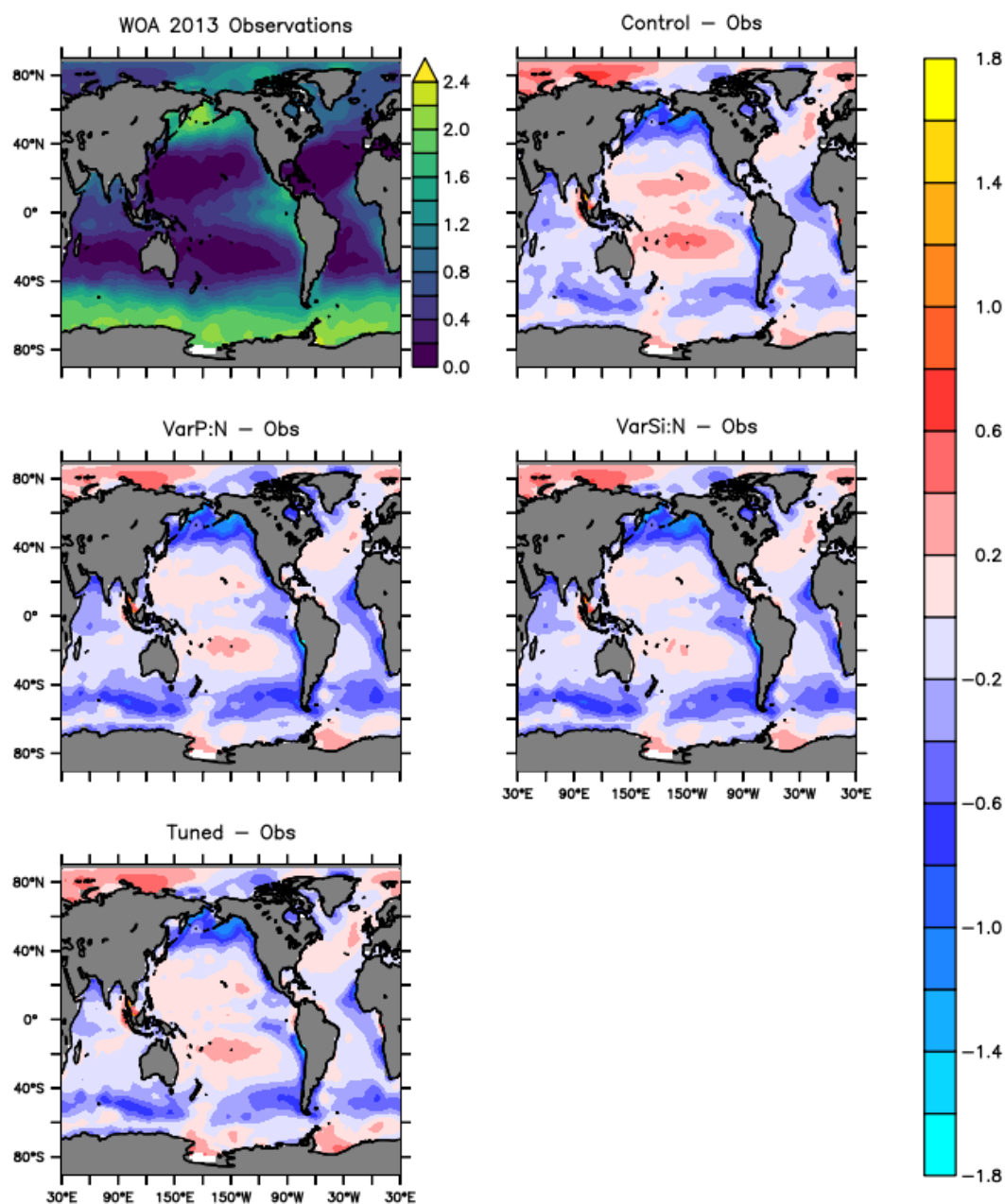
Figure S2. Surface Phosphate comparison.
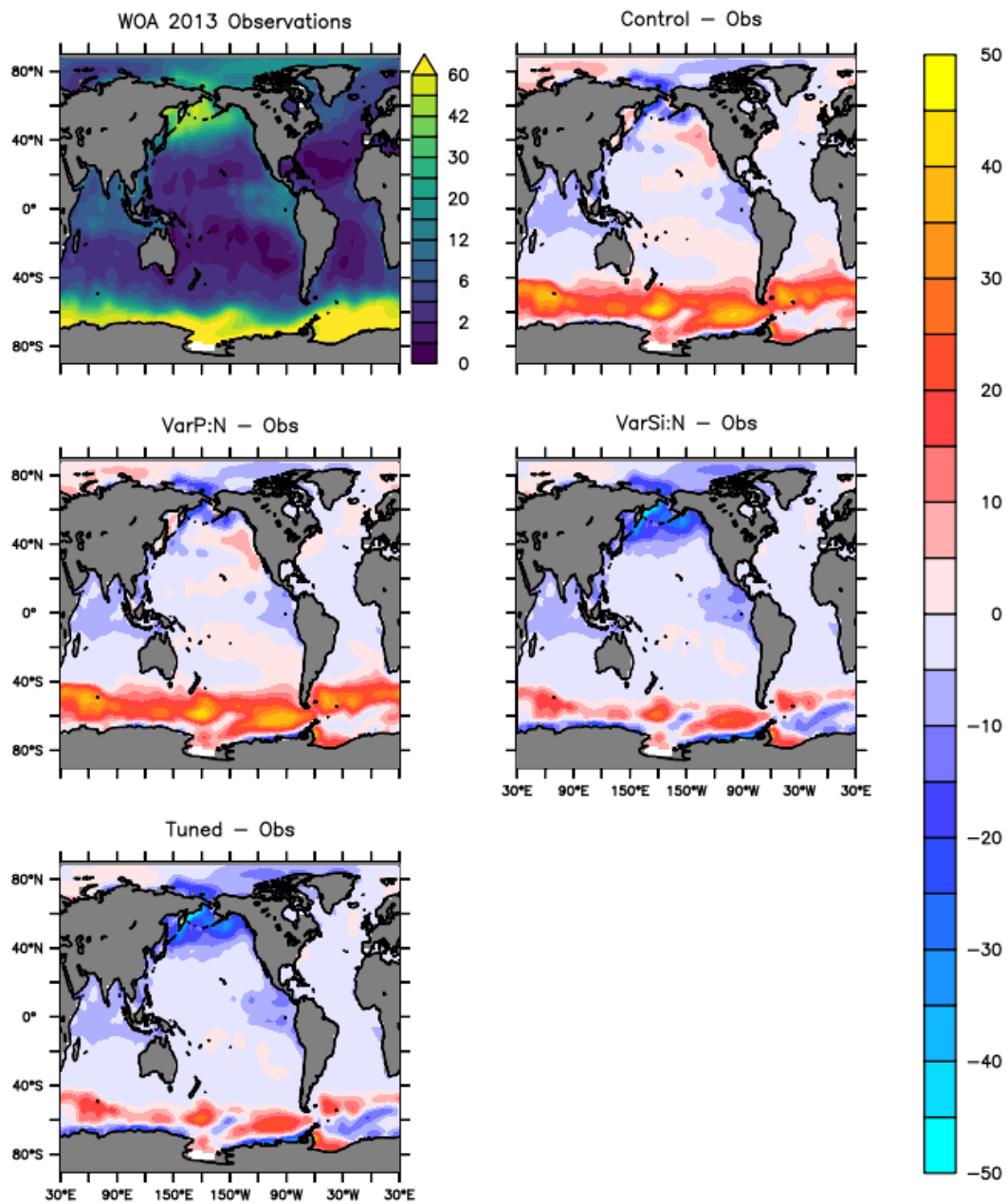
Figure S3. Surface Silicate comparison.
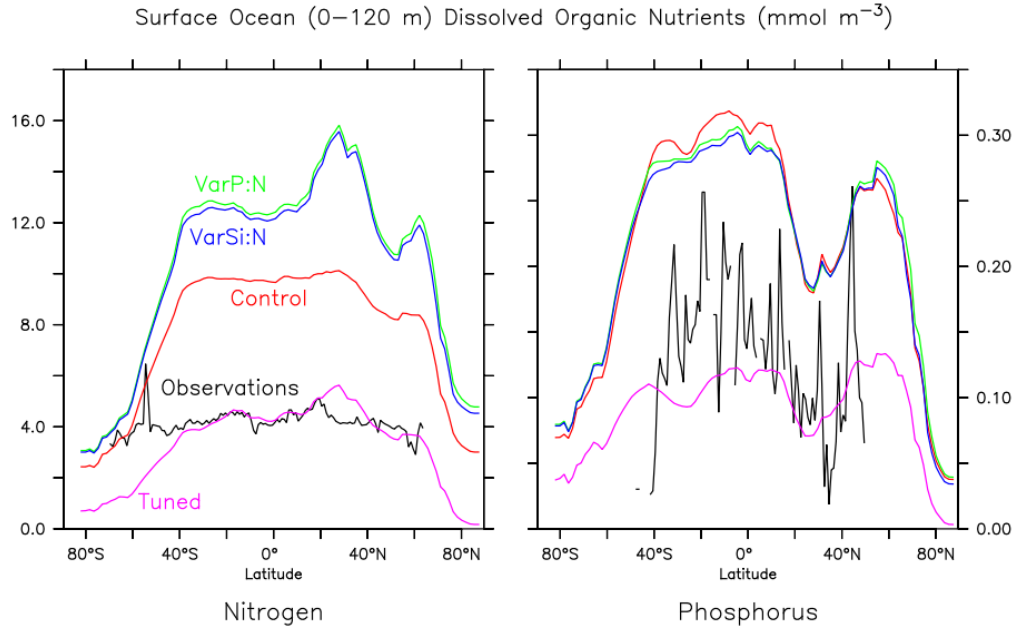
Figure S4. Dissolved organic nutrients, zonally averaged, with nitrogen (left) and phosphorus (right) in the surface ocean (0 – 120 m). Remineralization rates were increased 5-fold, resulting in the Tuned simulation better approximating the observations.

S1.3: N* Comparison and Analysis

N* is defined as (Gruber & Sarmiento, 1997; Sarmiento & Gruber, 2006):

$$N^* = NO_3 - 16 \times PO_4 + 2.9 \ (mmol \ m^{-3}) \tag{S1}$$

Calculating the absolute value of differences for N* comparisons:

$$|\Delta N^*| = |N^*_{model} - N^*_{obs}| = |(NO_3^{model} - 16 \times PO_4^{model}) - (NO_3^{obs} - 16 \times PO_4^{obs})| \tag{S2}$$

$$= |NO_3^{model} - NO_3^{obs} - 16 \times PO_4^{model} + 16 \times PO_4^{obs}|$$

$$= |(NO_3^{model} - NO_3^{obs}) - (16 \times PO_4^{model} - 16 \times PO_4^{obs})|$$

$$= |\Delta NO_3 - 16 \times \Delta PO_4|$$

Therefore, in the case that $\Delta NO_3 = 0$, ΔPO_4 exclusively causes ΔN^*:

$$|\Delta N^*| - |16 \times \Delta PO_4| = 0$$

Conversely, if $\Delta PO_4 = 0$, ΔNO_3 exclusively causes ΔN^*:

$$|\Delta NO_3| - |\Delta N^*| = 0$$
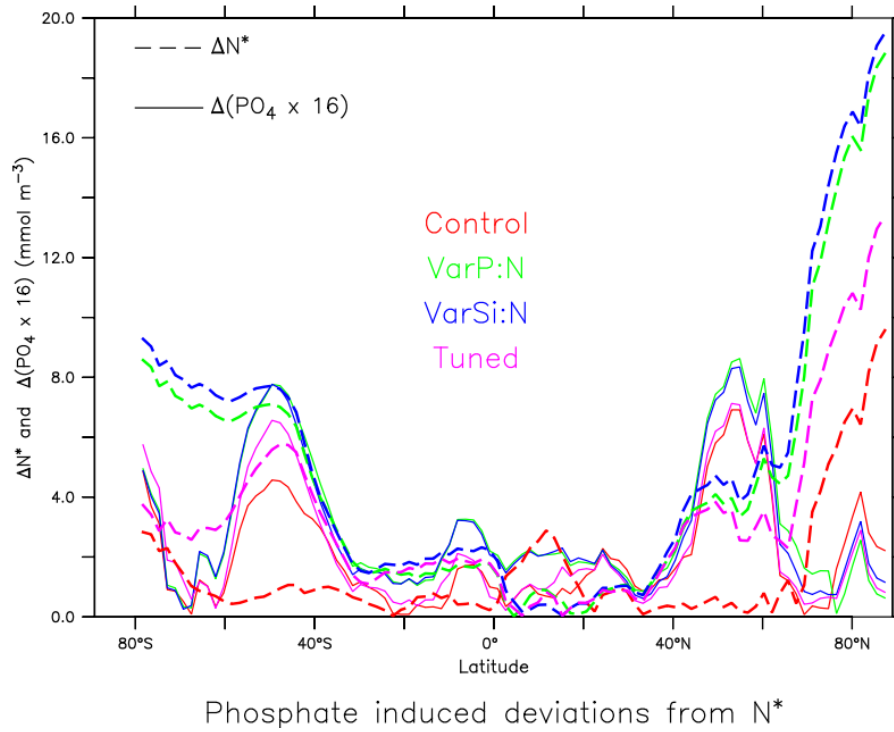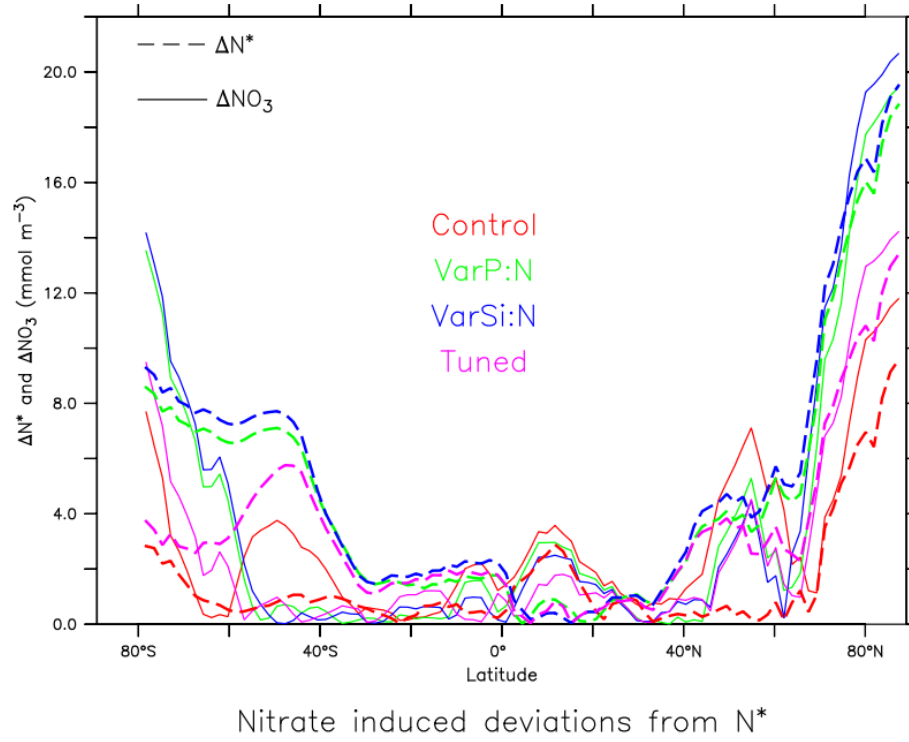
Figure S5. Deviations from observed zonally averaged N* values in each experiment caused by NO₃ (top) or PO₄ (bottom) simulation inaccuracies. The dashed lines show the absolute magnitude of the difference in N* between the observations and a given

experiment, whereas the solid lines show the NO$_3$ or PO$_4$ contribution to that difference. Thus, when two lines of a given color overlap, the corresponding nutrient is fully responsible for the N* deviation. See Equation S1 and S2, for calculation of N* differences.
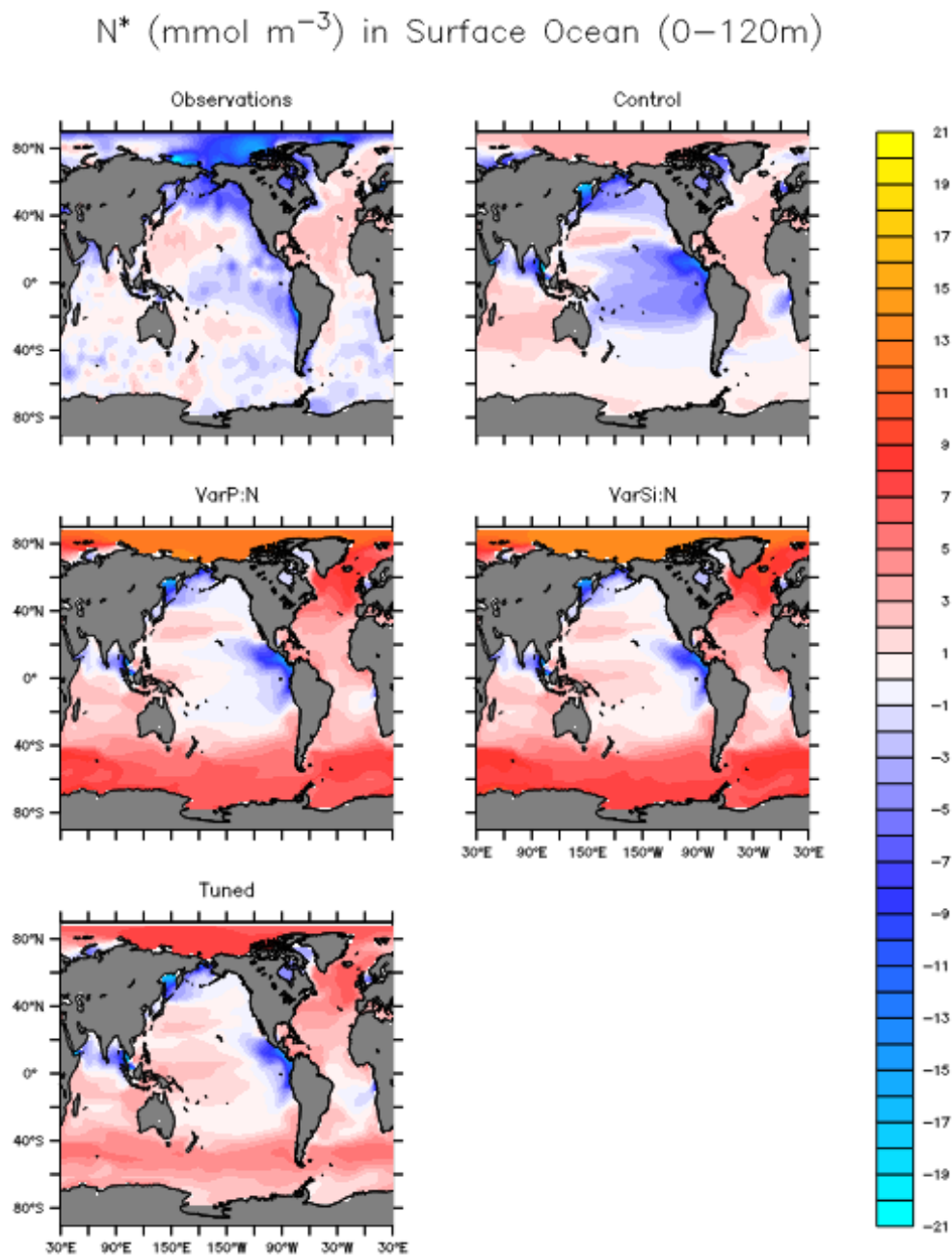
Figure S6. N* calculated from observation and simulations in the surface ocean (0 – 120 m). See Equation S1.

S1.4: Vertical Profiles of O₂ and NO₃
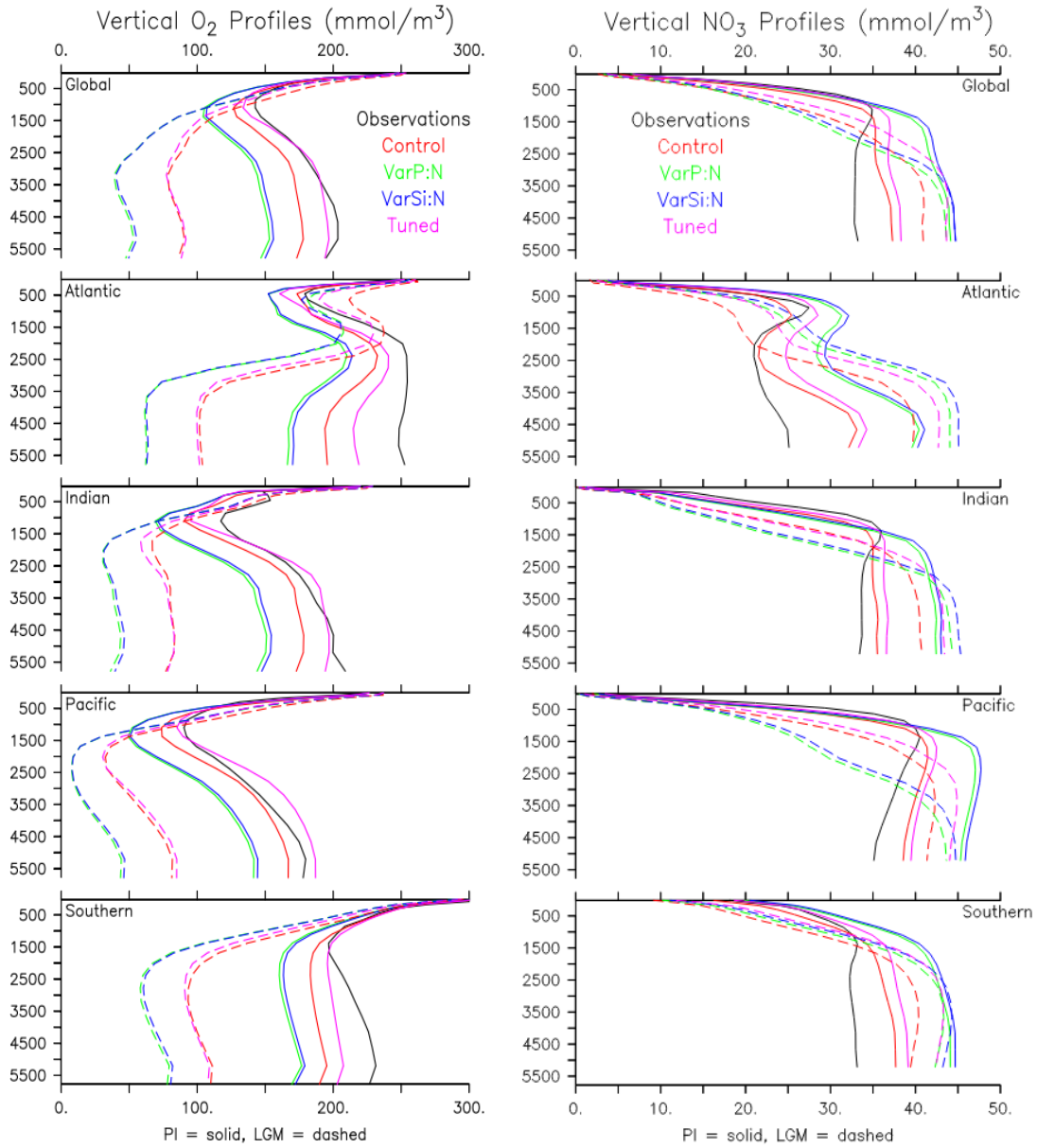
Figure S7. Vertical profiles of horizontally averaged O_2 and NO_3 in each ocean basin.

Text S2. Primary Producer Responses

S2.1: Global Limiting Nutrient Maps
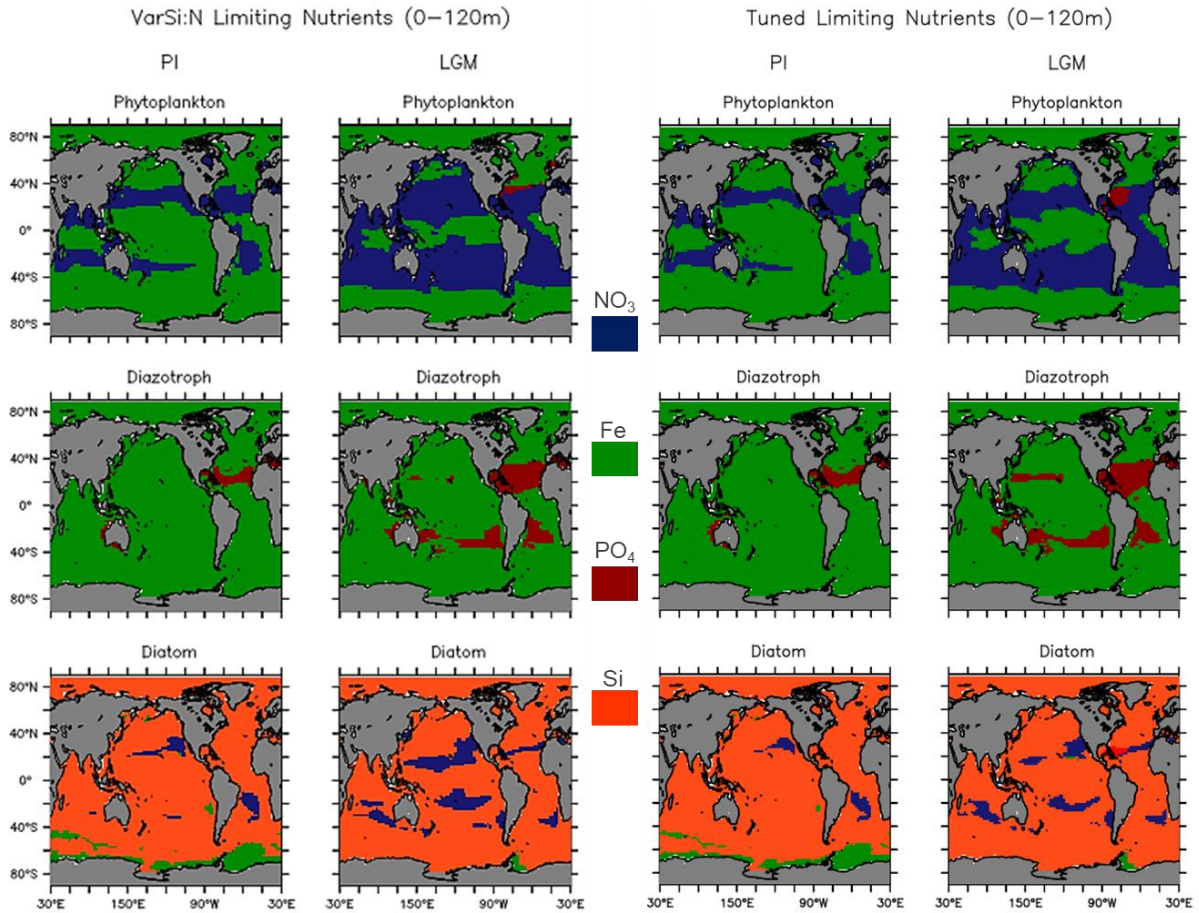
Figure S8. Primary limiting nutrients for each PFT in the surface ocean (0 – 120m). The accelerated DOM remineralization in Tuned decreases the P_O and P_{Diat} N limitation. Comparing VarSi:N to VarP:N (Figure 11), the P_{Diat} Si limitation is increased. The dustier LGM tends to decrease the Fe limitation for all between the PI and LGM simulations.

S2.2: NPP

Changes in NPP (mmol m^{-3} s^{-1})
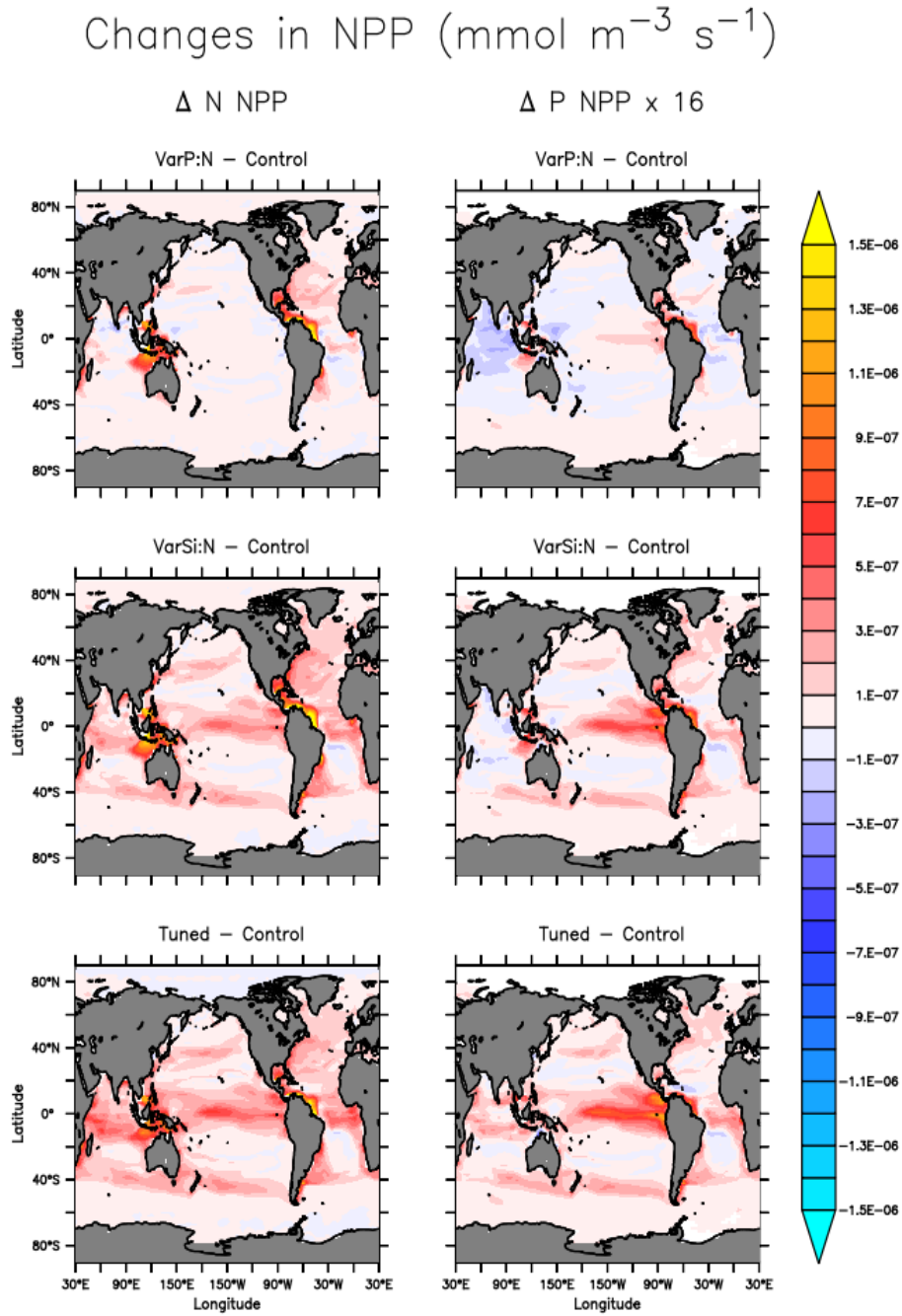
Figure S9. Changes in PI P$_O$ NPP between a given experiment and the Control. The left column of plots are the changes of NPP in N units, while the right are plots for P units recast (by a factor of 16) into pseudo-N units for easier comparison.
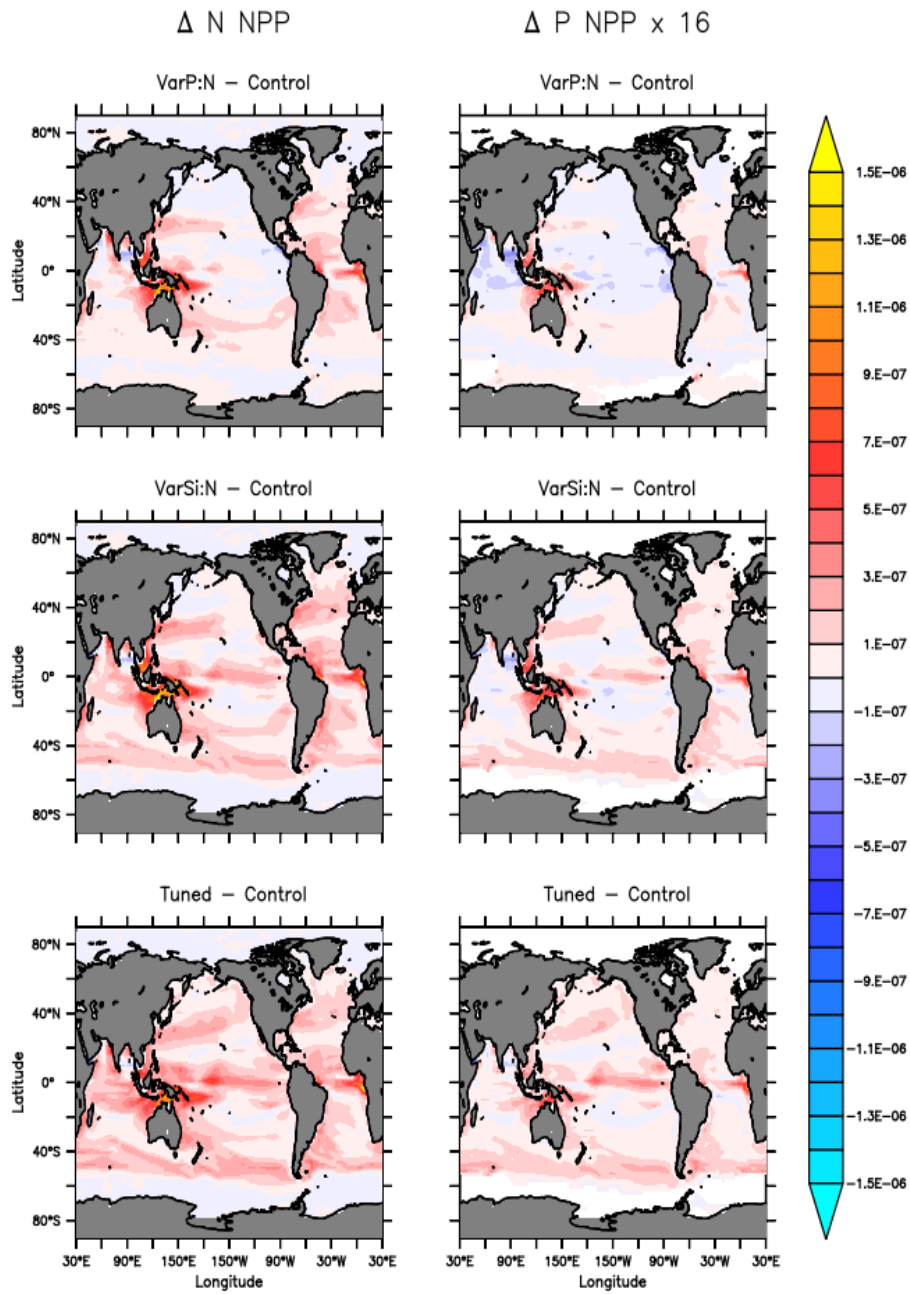
Figure S10. Changes in LGM P_O NPP between a given experiment and the Control. The left column of plots are the changes of NPP in N units, while the right are plots for P units recast (by a factor of 16) into pseudo-N units for easier comparison.
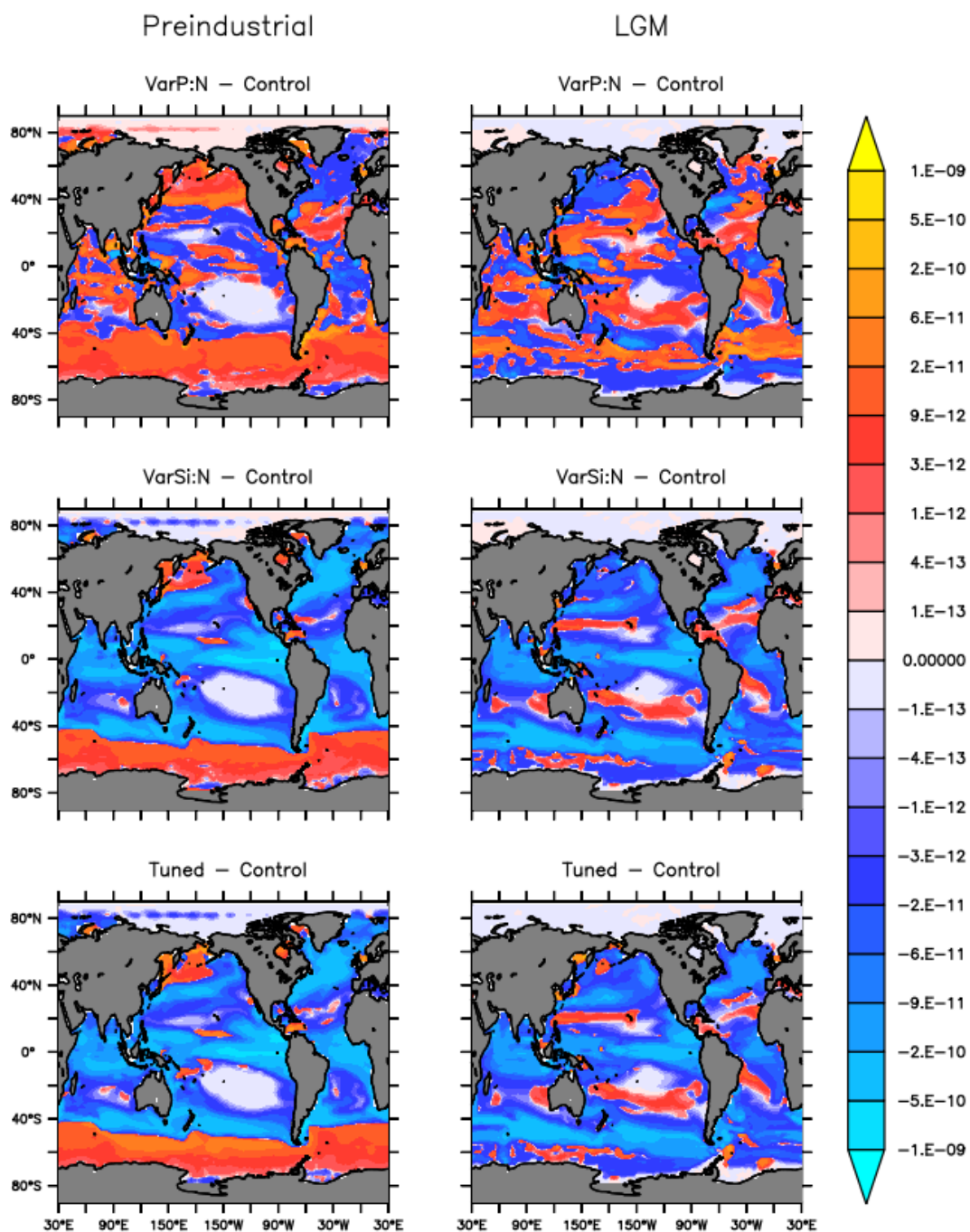
Figure S11. Changes in Diatom NPP in response to VarP:N (top row), VarSi:N (middle Row), and Tuned (bottom row) in the surface ocean (0-120 m) during the PI (left column) and LGM (right column). Note the logarithmic color scale.

S2.3: Relative Abundances

Table S2. Globally integrated plankton biomasses and relative abundances.

	Relative abundance (%)			Biomass (N Tmol)			
PI	P_O	P_{Diaz}	P_{Diat}	P_O	P_{Diaz}	P_{Diat}	P_Z
Control	44.1	1.9	54.0	4.0	0.2	4.9	5.7
VarP:N	54.8	3.7	41.5	6.4	0.4	4.9	5.5
VarSi:N	66.4	3.8	29.7	7.6	0.4	3.4	5.5
Tuned	66.9	2.9	30.2	7.6	0.3	3.4	5.7
LGM							
Control	41.5	2.0	56.6	3.1	0.2	4.2	4.7
VarP:N	58.6	4.5	36.9	6.7	0.5	4.2	4.4
VarSi:N	68.7	4.7	26.7	7.6	0.5	2.9	4.5
Tuned	69.5	3.3	27.2	7.5	0.4	2.9	4.6

Note. Relative abundances were calculated as the ratio of one PFT's biomass to the total biomass of all primary producers, excluding all zooplankton and detritus.
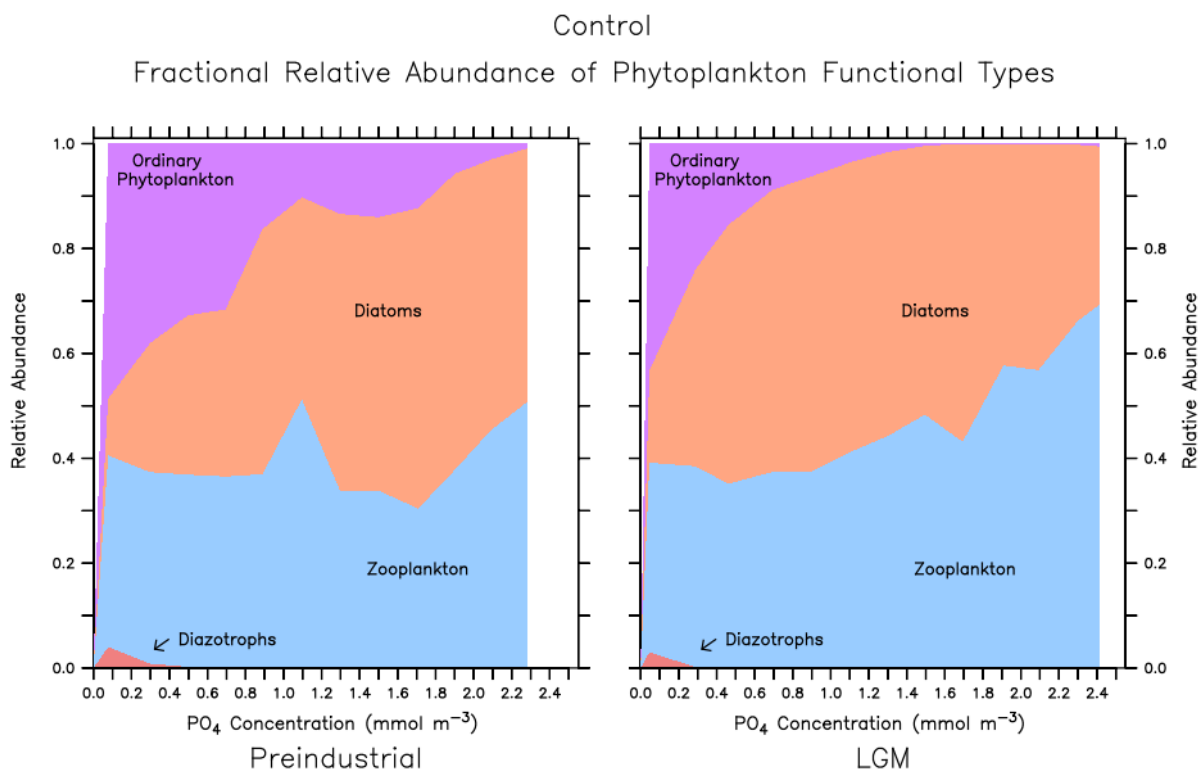
Figure S12. The relative abundance of each PFT against surface ocean (0-120 m) PO_4 concentrations in the Control.
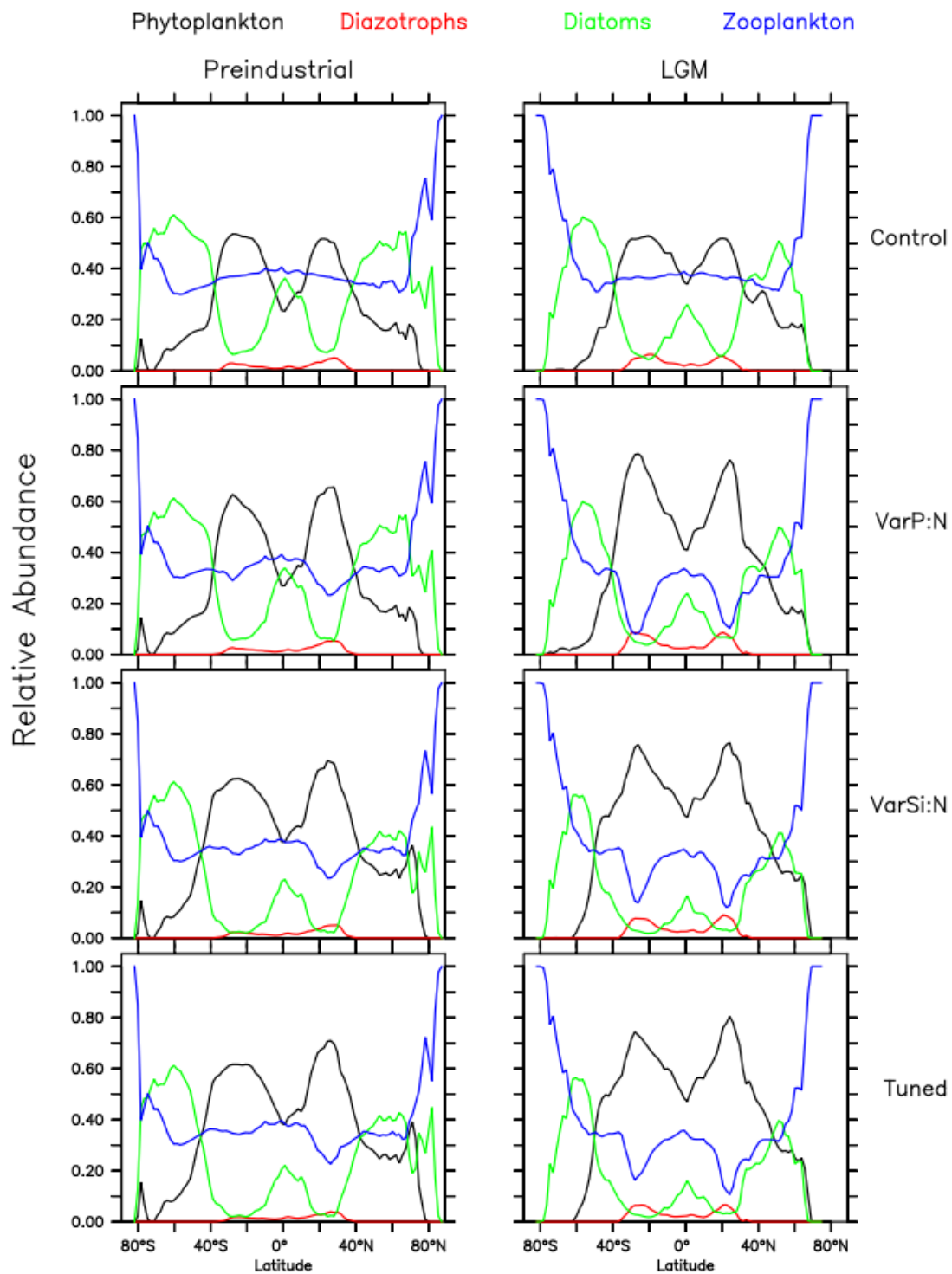
Figure S13. Zonally averaged relative abundance of each PFT in the surface ocean (0-120 m) in the PI (left column) and LGM (right column) oceans.

Text S3. Carbon Export Production and Associated Variables

Table S3. Global Carbon quantifications.

PI	pCO$_2$ (ppm)	pCO$_2$ (Pg)	Ocean total carbon (Pg)	Ocean DIC (Pg)	Ocean DOC (Pg)	Ocean POC (Pg)	DIC:Alkalinity (surface average)	Land carbon (Pg)
Control	273.3	573.9	37956	37674	280.1	1.5	0.8623	1808
VarP:N	274.9	577.3	38366	37978	385.6	1.7	0.8621	1812
VarSi:N	274.7	576.9	38255	37877	376.1	1.7	0.8623	1811
Tuned	273.3	573.9	37505	37447	56.9	1.7	0.8623	1808
LGM								
Control	204.7	429.9	38174	37931	242.0	1.3	0.8464	1334
VarP:N	193.3	405.9	38662	38273	387.5	1.6	0.8427	1287
VarSi:N	192.1	403.4	38558	38184	372.4	1.6	0.8426	1282
Tuned	190.5	400.1	37813	37754	57.4	1.6	0.8418	1276

*Note.* Land C does not include the 402 Pg of C buried under the ice in the LGM.
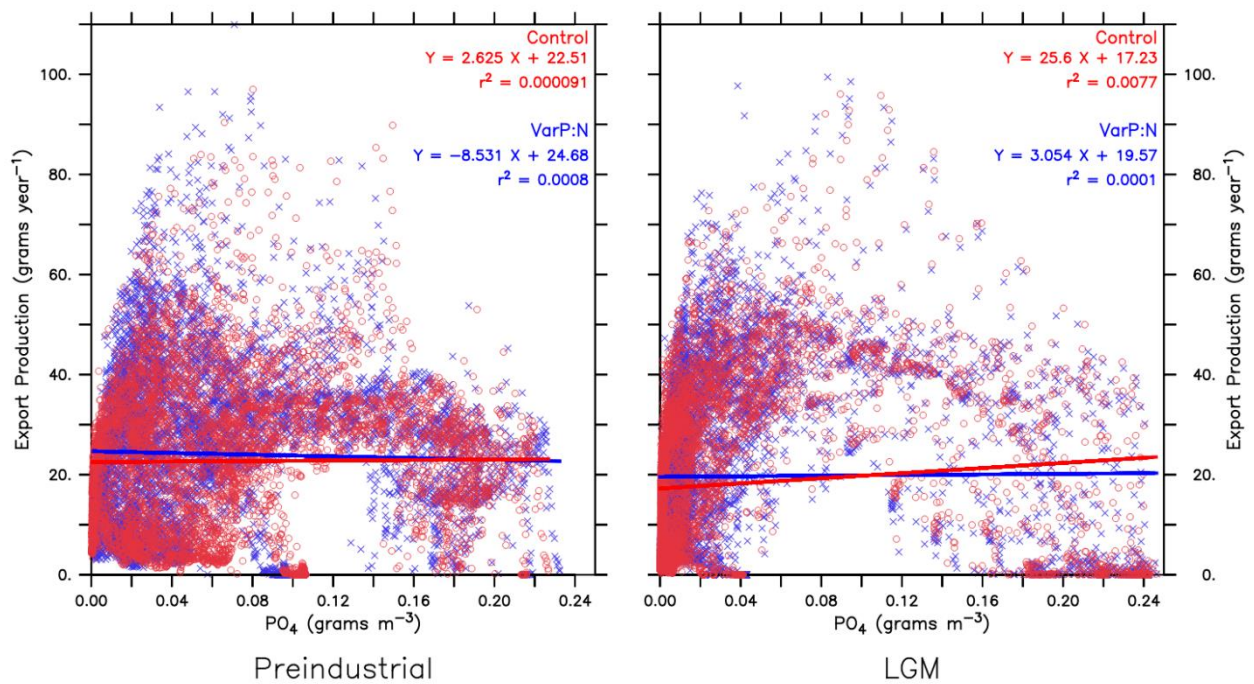
Figure S14. The relationship between C export and PO$_4$, which is used as a metric for oligotrophy. The PI is on the left with the Control in red and VarP:N in blue. The right is the same for the LGM. Based on the trendlines, VarP:N exports more C than the Control at low PO$_4$. This holds for most of the PI ocean but is only valid up to 1.0 g PO$_4$ m^{-3} in the LGM. However, more LGM grid points have low PO$_4$ than high. Thus, VarP:N

exports more C than the Control. Many other nutrient (NO$_3$, Fe, etc.) and environmental (light, temperature, etc.) variables regulate C export, hence the low r^2 values.
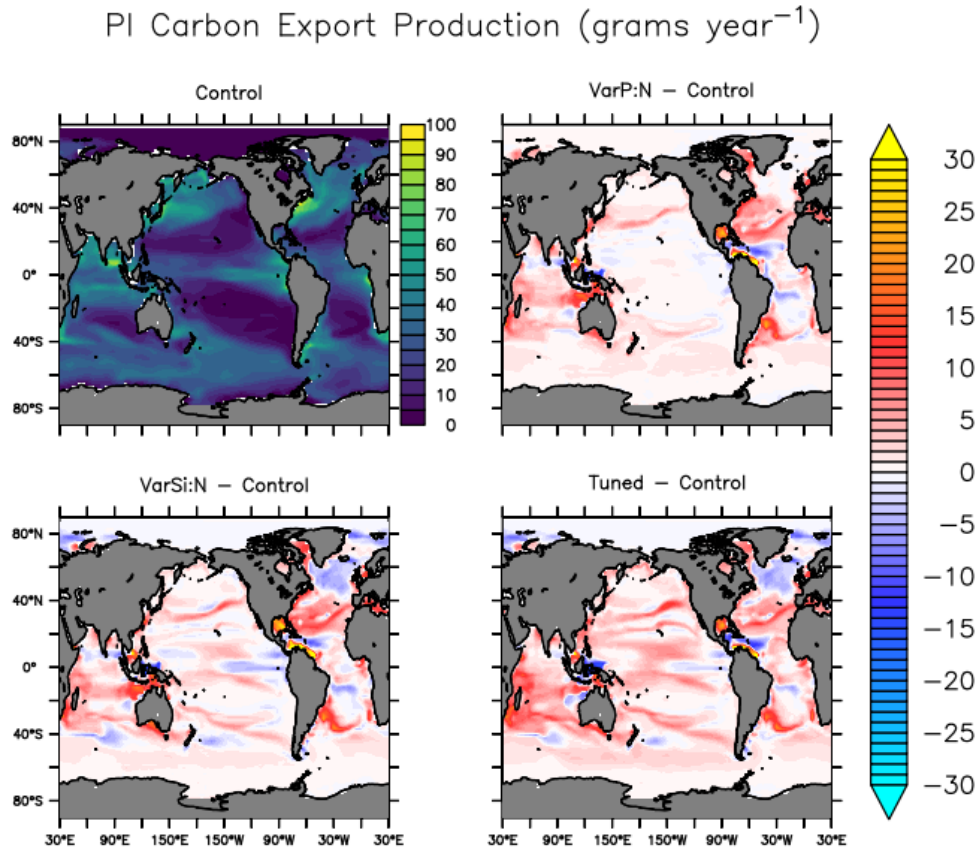
Figure S15. Carbon Export Production in the PI Control simulation with changes induced by the VSMs.
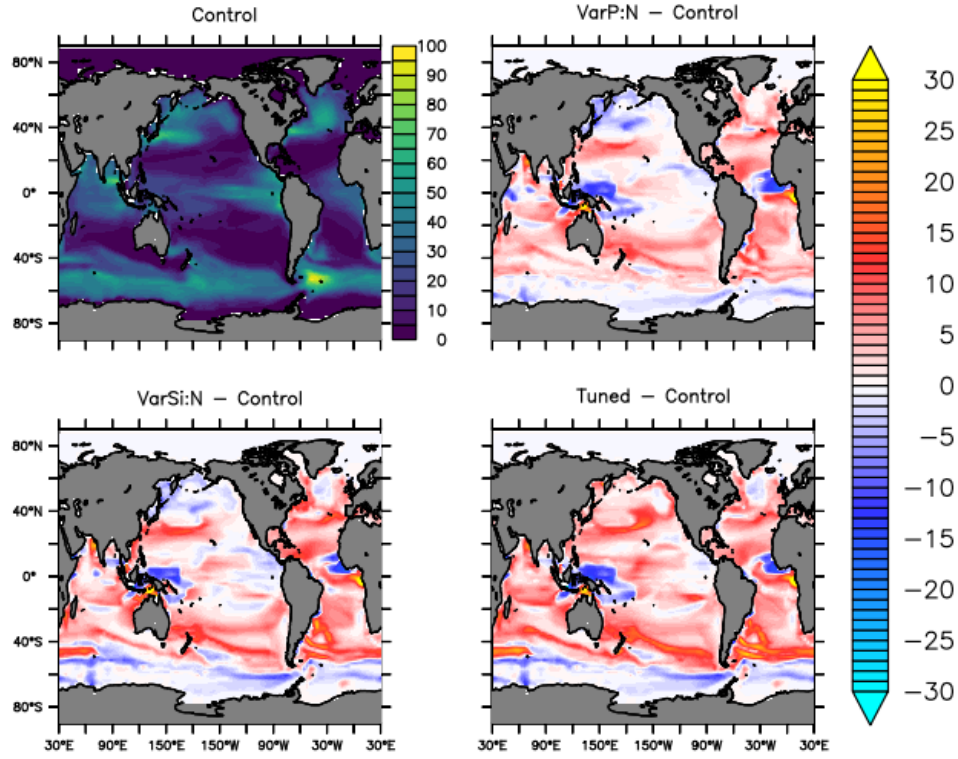
Figure S16. Carbon Export Production in the LGM Control simulation with changes induced by the VSMs.

Table S4. Linearized approximations of changes in DOC fluxes.

LGM – PI (Pg C year^{-1})	Control	VarP:N	VarSi:N	Tuned	VarP:N - Control	VarSi:N - Control	Tuned - Control
$\mu^*_{P_O}(\Delta P_O)$	-0.07	0.04	0.01	0.01	0.11	0.08	0.08
$\Delta(\upsilon_{P_O} P_O T_S)$	-0.18	-0.09	-0.18	-0.19	0.08	0.00	-0.02
$\upsilon_{P_O}(\Delta P_O)T_S$	-0.11	0.08	0.01	-0.01	0.19	0.12	0.10
$\upsilon_{P_O}P_O(\Delta T_S)$	-0.08	-0.15	-0.18	-0.18	-0.08	-0.10	-0.10
$\Delta(\lambda_{DOC}[DOC]T_S)$	-0.46	-0.27	-0.31	-0.33	0.19	0.15	0.13
$\lambda_{DOC}[DOC](\Delta T_S)$	-0.26	-0.39	-0.38	-0.38	-0.13	-0.13	-0.13
$\lambda_{DOC}(\Delta[DOC])T_S$	-0.25	0.11	0.06	0.04	0.37	0.32	0.29
Average Temperature (°C)	-2.16	-2.27	-2.28	-2.28	-0.12	-0.13	-0.12

Note. Selected variables are the P_O specific (μ^*) and quadratic (υ) mortalities (Table S8), the temperature scaling function $T_S=1.066^T$, DOC remineralization (λ_{DOC}), and the average temperature changes. The three right-most columns are the LGM to PI difference of a VSM compared to the same difference in the Control. Both decomposed terms that isolate changes in P_O can be summed for the total P_O effect on DOC and be compared to the corresponding temperature effect.
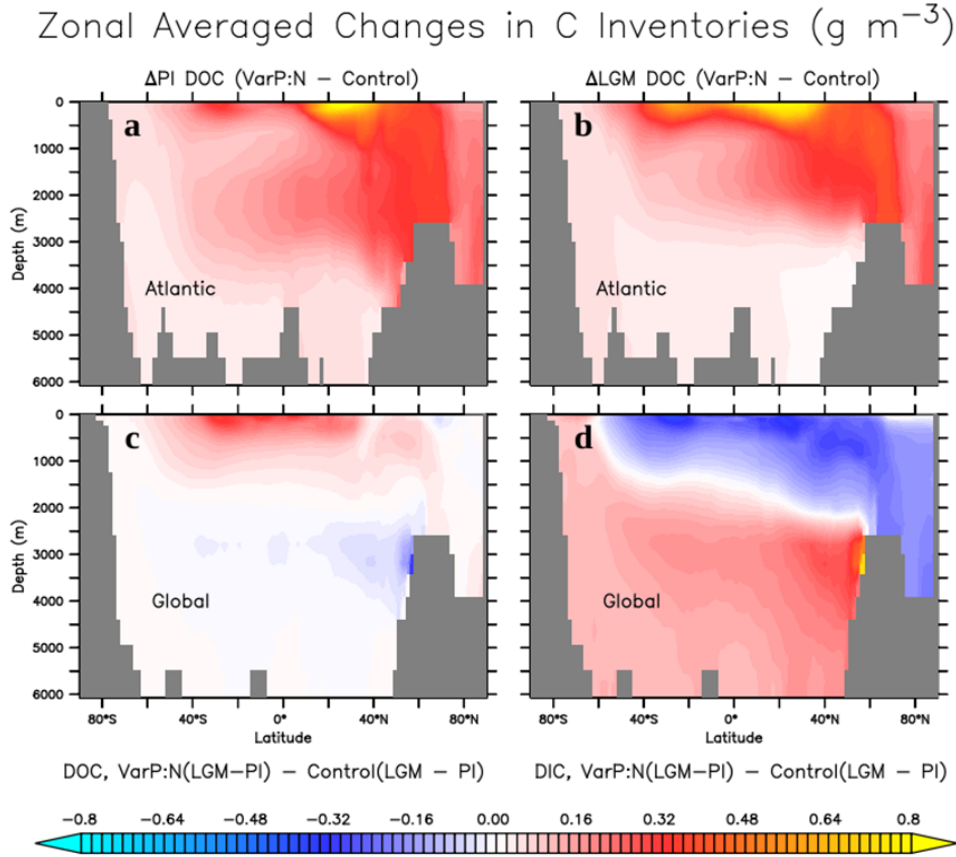
Figure S17. Cross-sections of changes in DIC and DOC. Panels A and B show the VarP:N change in DOC in the PI and LGM Atlantic. The North Atlantic Deep Water (NADW) is visible in DOC's trajectories. Notably, the shoaling of the NADW between the PI and LGM, moves upward the midlatitude deep Atlantic DOC maxima, inducing a negative signature there when comparing the relative LGM-PI DOC changes between VarP:N and Control in Panel C. Panel D the same relative changes but for DIC.

S3.1: Diatom Carbon Export Production.

The amount of P_{Diat}-sourced C that is exported while adhered to the siliceous frustules can be approximated in the following manner. The surface ocean average Fe is weighted by the P_{Diat} biomass and submitted as an argument to the *VarSi:N* model (Equation S4) to calculate the Si:N of P_{Diat}. Once this ratio is divided into the Si export (Si_{EP}), the result describes the ballasted N EP of P_{Diat} as if there were no degradation of soft tissue. Therefore, we subtract off the remineralization and grazing terms from this value (Table S8). It can then be easily converted to C EP using the fixed C:N (Equation S5). The biogenic Si sinking velocity is captured in the Si_{EP} variable.

$$\overline{[Fe]} = \frac{1}{\int_{-120m}^{0} P_{DT}\,dz} \times \int_{-120m}^{0} Fe \times P_{DT}\,dz \tag{S3}$$

$$Si:N\left(\frac{mol}{mol}\right) = -\alpha * \tanh\left(\beta * \overline{[Fe]} - \gamma\right) + \varepsilon \tag{S4}$$

$$P_{DT_{EP}} = \left[\frac{Si_{EP}}{Si:N} - (1-\gamma)P_z G^*_{P_{DT}} - (1-\sigma 1_{DOM})\upsilon_{P_{DT}}P_{DT}\right] \times C:N \tag{S5}$$

Otherwise, if all the P_{Diat} soft tissue is disassociated from the faster sinking biomineral, then the P_{Diat}-only portion of the simulated detritus is given as

$$P_{DT_{EP\_soft}} = w_D\acute{\alpha}\left[(1-\gamma)P_z G^*_{P_{DT}} - (1-\sigma 1_{DOM})\upsilon_{P_{DT}}P_{DT}\right] \times C:N \tag{S6}$$

Where $\acute{\alpha}$ is the timestep of biology used in the model and w_D is the sinking velocity of the detritus. The remaining variables are described in Table S8.

Table S5. Quantifications of the global Si inventory in the surface ocean (left column) and the C export from the surface ocean.

PI	Surface Si (Pg)	C EP via biogenic Si (Pg year^{-1})	C EP via detritus (Pg year^{-1})
Control	37.1	3.2	0.3
VarP:N	36.1	3.9	0.2
VarSi:N	22.6	1.5	0.2
Tuned	22.4	1.6	0.2
LGM			
Control	24.0	2.4	0.2
VarP:N	23.5	3.0	0.2

VarSi:N	16.4	1.6	0.1
Tuned	16.4	1.7	0.1

Note. Total ocean Si inventories are ~9039 Pg but vary little between experiments. The middle column assumes organic matter adheres to the diatom siliceous frustules, while the right column assumes all soft organic matter sinks independently.

The EP of exclusively soft P_{Diat} POM, exported through the detritus inventory, at the bottom of the euphotic zone (120 m) and is ~5 - 10% of the P_{Diat} C export when assuming adhesion to fast-sinking frustules (Table S5). Without the frustules, P_{Diat} EP reduced by ~0.08 Pg C year^{-1} (~35%) from PI *VarSi:N*, instead of the ~2.4 Pg C year^{-1} reduction (~62%) with the accelerated sinking. The model may also be notably underestimating the P_{Diat} C EP in all simulations and may have notable implications for the C export quantifications and atmospheric CO_2 changes between climate states.
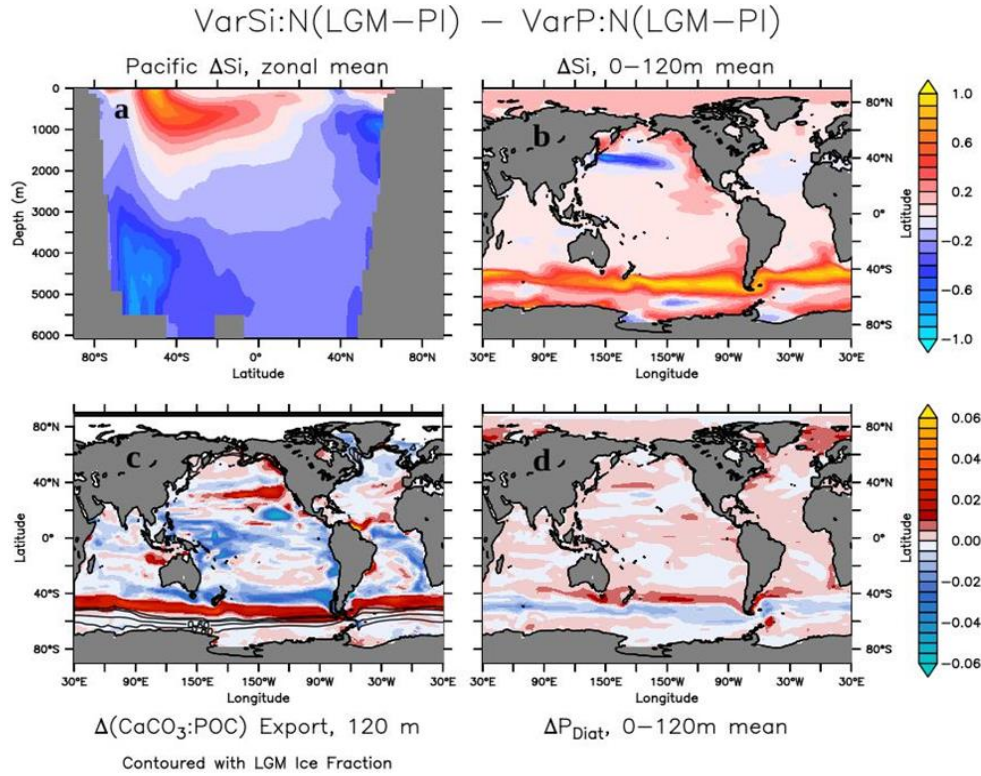
Figure S18. Silica leakage from the Southern Ocean in the LGM. The Pacific sector cross-section (a) and surface map (b) are in units of grams of Si m^{-3} and show the transport of Si from the SO to the equatorial East Pacific. The CaCO$_3$:POC export ratio

(c) and contoured sea ice fraction are unitless. Changes in P_{Diat} are in grams of C m^{-3}. All panels show the difference between VarSi:N's and VarP:N's LGM to PI change, thus removing the climate shift's effect on the selected variables and allowing exclusive visualization of the VarSi:N's influence on the Si cycle.

Text S4. Effects of Reduced Sedimentary Fe Fluxes in the LGM

With the formation of massive ice sheets in the LGM came lower sea levels (~ 125 m) (Lambeck et al., 2014; Muglia et al., 2018). The exposed continental shelves caused a reduction of the sedimentary Fe fluxes into the ocean (Muglia et al., 2017). The model configurations used in this study neglect an interactive ocean sediment module. Particulate organic matter (POM) is then instantaneously remineralized into the adjacent grid cell when it intersects the seafloor. We explored the effects of the altered ocean basin geometry in the LGM by including a recalculated sub-grid bathymetry (SGB) map for the LGM, but we emphasize there are large uncertainties in the model's Fe cycle, as well as the parameterization of the sedimentary Fe flux rates, which rely on constant stoichiometric ratios (Galbraith et al., 2010; Muglia et al., 2017, 2018; Tagliabue et al., 2009). Muglia et al. (2017) discuss in detail the potential limitations of the model's LGM Fe cycling.

The effects of the recalculated Fe sedimentary fluxes (Table S6) here are broadly consistent with those found by Muglia et al. (2017). The recalculated bathymetry map reduced the global ocean and euphotic zone Fe inventory but has notable implications when considering variable stoichiometry and the population dynamics of ocean primary producers. Of course, a reduction in euphotic zone Fe leads to reduced primary production, but when combined with *VarP:N* it also reduced the P_O-P_{Diaz} cohabitation (discussed in the main manuscript) thus reducing total NPP further. The revised sedimentary Fe fluxes expand the Fe limitation for all primary producers (see Figure S19). Ultimately, this leads to a reduction in C EP and reduced efficiency of the biological carbon pump which yields a smaller PI-to-LGM CO_2 drawdown and higher simulated LGM atmospheric CO_2 concentrations.

Of the selected variables in Table S6, most change similarly in the *Control* and *Tuned* models in response to the new SGB. However, the N-fixations, denitrification, and phytoplankton variables change substantially, highlighting the Fe-sensitivity of the P_O-P_{Diaz} cohabitation. These variables, as shown in the main text, are important for C export and ocean inventory quantifications. There are, however, some improvements to the simulated $\delta^{15}N$ and $\delta^{13}C$ as compared to observations, Table S7. The notable changes to N-fixation and denitrification, as opposed to the comparatively small changes in biological C export, explain the more profound impact that the new SGB has on $\delta^{15}N$ representations as compared to the $\delta^{13}C$ representations.

Table S6. Comparison of selected parameters in response to adjusted LGM sedimentary Fe fluxes caused by lower sea levels.

Parameter	Control		Tuned		ΔControl	ΔTuned
	PI SGB	LGM SGB	PI SGB	LGM SGB		
Atmospheric CO_2 (ppm)	204.7	205.9	190.5	197.2	1.2	6.7
EP (Pg C year^{-1})	7.1	6.9	8.3	7.9	-0.2	-0.4
Total Fe inventory (Tg)	61.3	59.5	61.8	58.8	-1.8	-3.0
Surface (0-120 m) Total Fe inventory (Tg)	1.3	1.1	1.1	0.9	-0.2	-0.2
N-Fixation (Tg year^{-1})	145.9	100.8	224.3	108.3	-45.1	-116.0
Water Column Denitrification (Tg year^{-1})	92.6	53.1	155.4	40.7	-39.5	-114.7
Benthic Denitrification (Tg year^{-1})	66.5	58.7	86.3	69.1	-7.8	-17.1
Total NO_3 Inventory (Pg)	2615.4	2723.9	2848.5	2926	108.5	77.5
Surface (0-120 m) NO_3 (Pg)	8.8	9.7	12.6	13.5	0.9	0.9
P_O biomass (N Tmol)	3.0	2.9	7.5	5.6	-0.1	-1.9

Diazotroph Biomass (N Tmol)	0.2	0.1	0.4	0.2	0.0	-0.2

Note. PI SGB indicates that the ocean geometry remained that of the PI ocean during the LGM simulation, while the other column refers to the recalculated LGM bathymetry due to lower sea levels.

Thus, the influence of variable stoichiometry in ocean biogeochemical models can strongly depend on the configuration and accuracy of tertiary, biologically-relevant model components. Using a different Fe flux scheme substantially altered the modeled climate impacts our variable stoichiometry schemes had. It is alternatively possible that the inclusion of other earth system components in the model would diminish the importance of the SGB remineralization schemes. The variable stoichiometry influences will likely vary considerably in other global climate and/or ocean biogeochemical models. Further research and testing are needed to determine the sensitivity of these stoichiometry schemes to various biogeochemical processes.
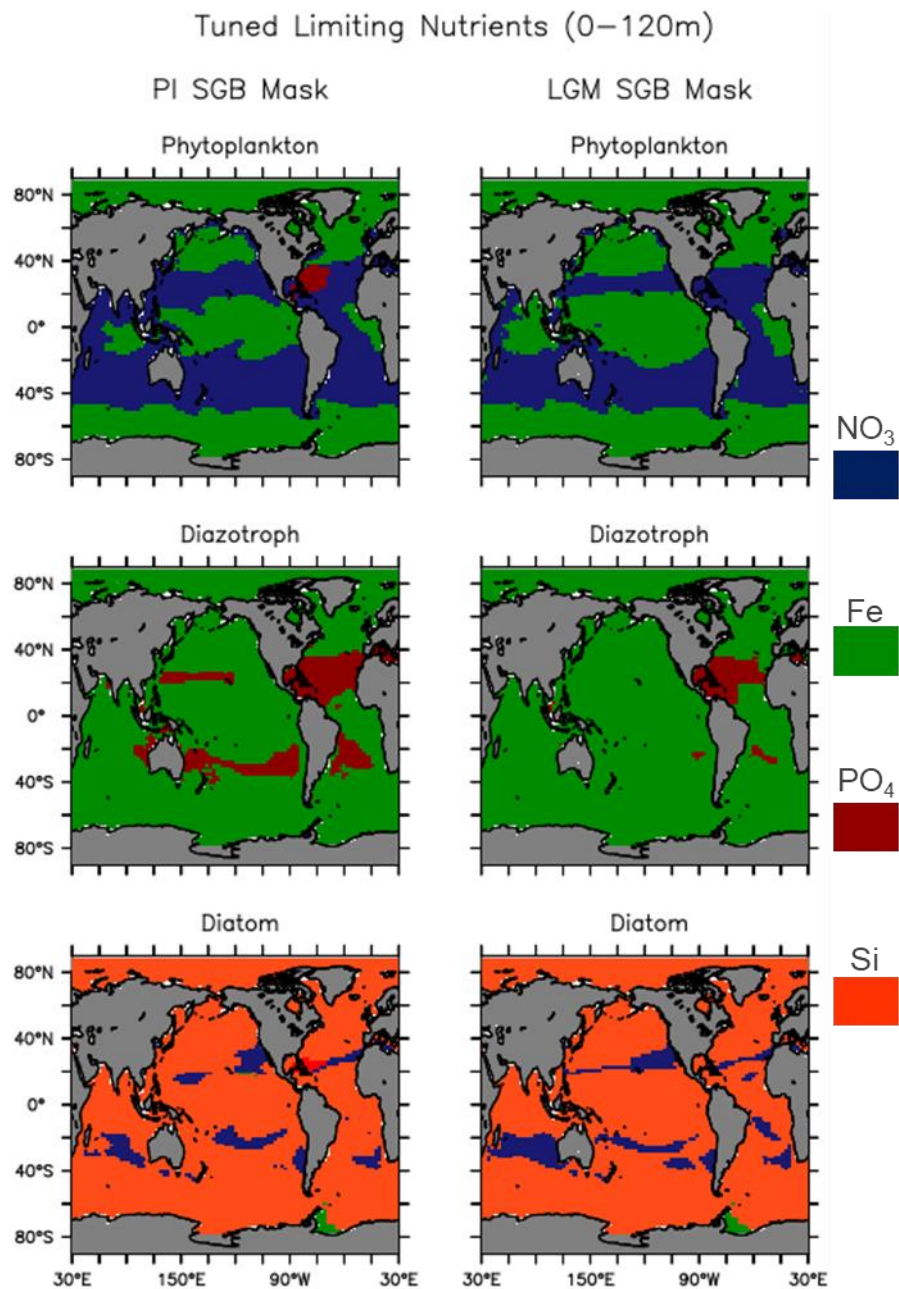
Figure S19. Comparison of each PFT limiting nutrients in response to changes in sedimentary Fe flux from lowered LGM sea levels and recalculated SGB. PI SGB configuration is on the left column and the LGM configuration is on the right. Both simulations are performed under identical LGM boundary conditions.

**Text S5. Variable Stoichiometry Effects on δ^{15}N**

S5.1: Preindustrial

  VarP:N caused a larger N NPP increase than P NPP. From the *Control*, *VarP:*N global N NPP increased by ~13% while P NPP increased by only 2%. *VarSi:N* did not change either NPP considerably, while the *Tuned* model added another 3 and 5% increase, respectively (See Table 3 in main text). An increase in primary production consequently causes increased respiration, altering the O_2 concentrations at depth, thereby changing denitrification rates (Figure S7, S22, and S24) (Somes et al., 2010). Each of these processes uniquely fractionate N isotopes, thus, $\delta^{15}N$ values, which are used to constrain the model, are heavily influenced by variable stoichiometry (Schmittner & Somes, 2016; Somes et al., 2010). The VSMs did not substantially improve simulations of N isotopic ratios. In low oxygen areas, the increased export drives notable inaccuracies in simulated $\delta^{15}N$ values. Many of these are corrected in the *Tuned* simulation.
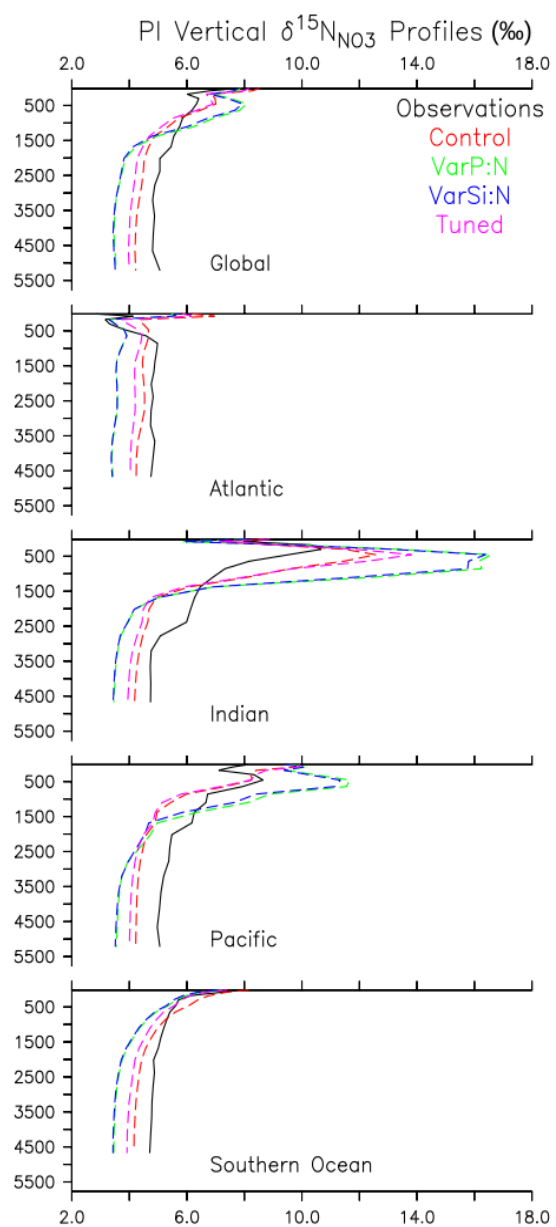
Figure S20. Vertical profiles of horizontally averaged $\delta^{15}N$ in the preindustrial ocean.
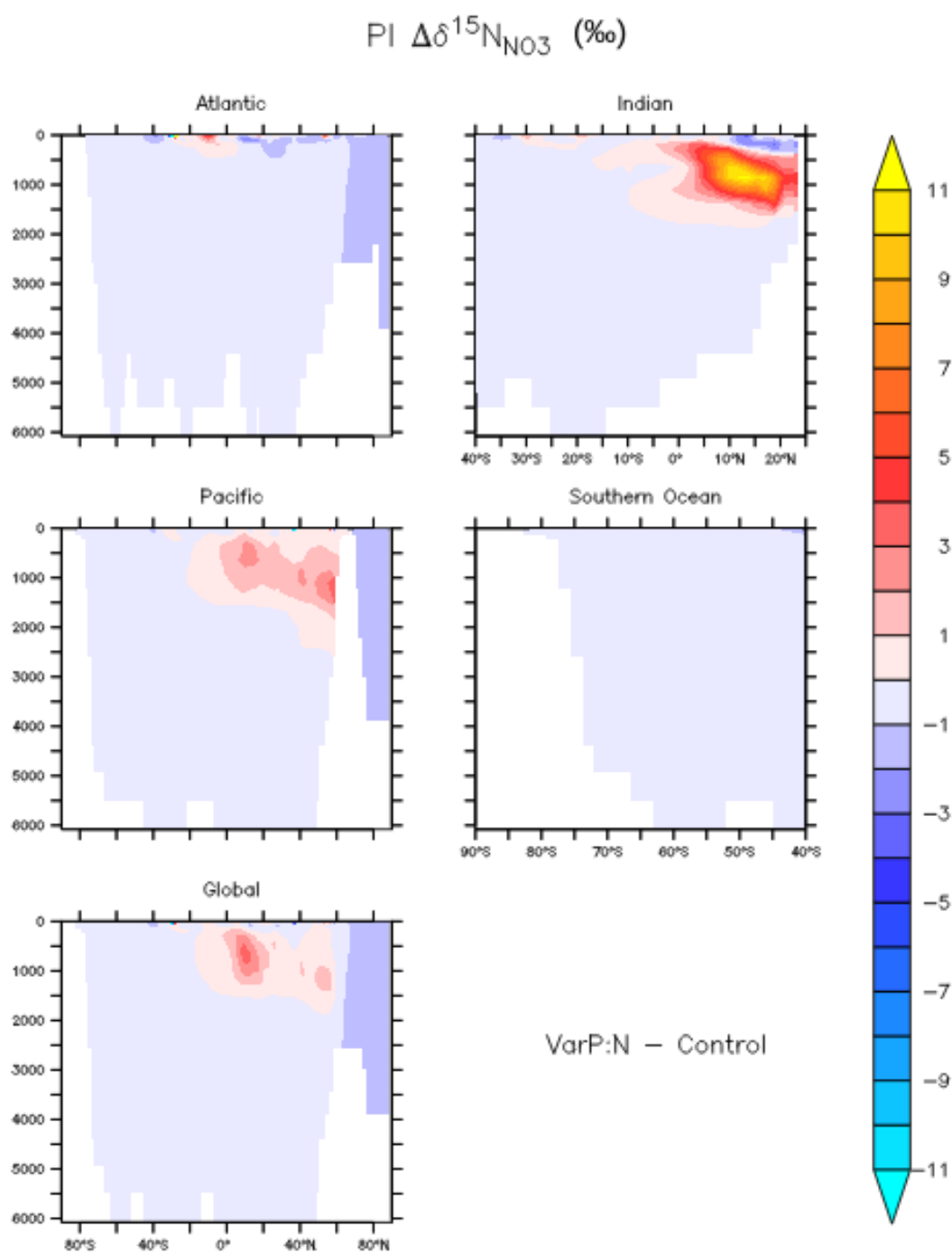
Figure S21. Changes in the $\delta^{15}N$ of NO₃ in response to VarP:N in the preindustrial ocean basins.
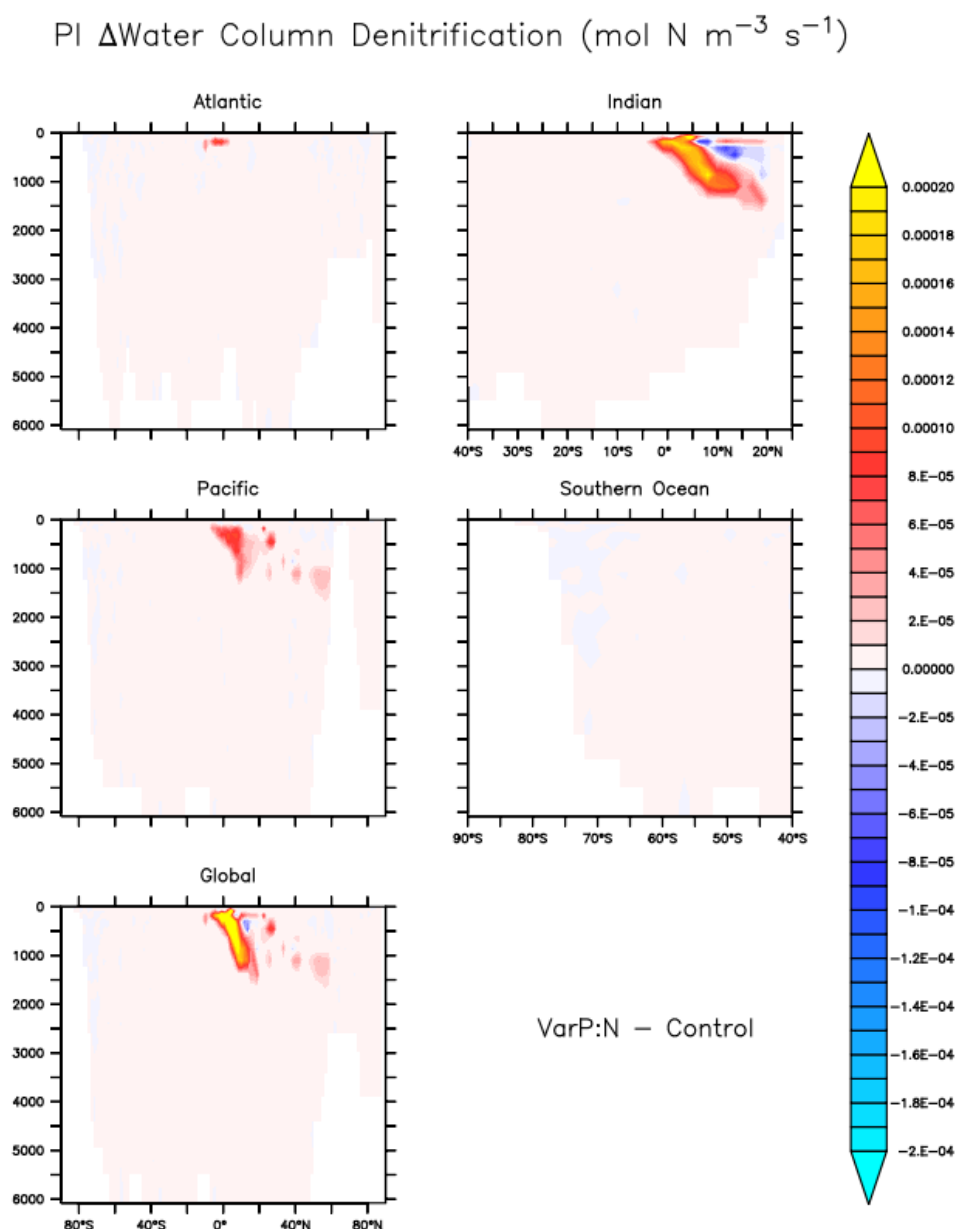
Figure S22. Changes in the water column denitrification in response to VarP:N in the PI ocean basins.

Against observed values, *VarP:N* and *VarSi:N* improve $\delta^{15}N$ simulations in the upper Atlantic and Southern Oceans, above ~500 m, however, both overestimate values in the upper Indian and Pacific (Figure S20) (Somes et al., 2010). These overestimations correlate with regions of low oxygen, suggesting that the increased export of organic matter in *VarP:N* and *VarSi:N* is too high in these areas which subsequently yields too

much denitrification that strongly increases δ^{15}N values (Figures S21 and S22). Similar effects on δ^{15}N was observed in the CSIRO model (Buchanan et al., 2019). The accelerated remineralization of the *Tuned* experiment corrects these overestimations in the upper Indian and Pacific Ocean basins, generally outperforming the *Control* simulation. All experiments underestimate δ^{15}N at depth; the deep ocean values are similar across each basin but remain sensitive to the soft tissue pump as the enhancement of the EP from the VSMs causes preferential export of ^{14}N. Here, the *Tuned* simulation does not best the *Control* but is only slightly less accurate (Table S7). δ^{15}N data for the PI and LGM were compiled and compared against the *Control* model performance in previous works (Muglia et al., 2018; Schmittner & Somes, 2016; Somes et al., 2010).

Table S7. Statistical performance of simulated δ^{15}N and δ^{13}C. Note the PI comparison is representative of the whole ocean volume.

| PI δ^{15}N:	R	STDR	RMS Prime	RMSE
Control	0.75	1.26	0.84	0.84
VarP:N	0.77	2.16	1.53	1.53
VarSi:N	0.77	2.09	1.46	1.47
Tuned	0.75	1.30	0.86	0.88
LGM δ^{15}N:				
Control	0.09	1.24	1.53	1.68
Control + SGB	0.15	1.02	1.31	1.61
VarP:N	0.05	1.94	2.14	2.26
VarSi:N	0.06	2.02	2.20	2.28
Tuned	0.06	1.67	1.90	1.98
Tuned + SGB	0.23	1.08	1.29	1.66
LGM δ^{13}C:				
Control	0.79	0.97	0.64	0.65
Control + SGB	0.79	0.96	0.63	0.64
Tuned	0.79	0.97	0.64	0.74
Tuned + SGB	0.79	0.92	0.62	0.63

Note. Conversely, the LGM comparison is only representative of the surface ocean from where the bulk organic matter measured in the sediment cores originates. Values for each parameter are calculated as described in Muglia et al. (2018).

S5.2: LGM

LGM δ^{15}N data, while spatially limited, represents the cumulative interplay between surface ocean δ^{15}N values and subsequent fractionation by biological processes (Galbraith et al., 2013; Tesdal et al., 2013). Sedimented organic matter isotopic

signatures are exemplary of surface signatures and so the $\delta^{15}N$ of simulated detritus is compared to LGM data (Tesdal et al., 2013). The *Control* experiment mainly errs with overestimations of $\delta^{15}N$ values in the surface North Pacific and Bering Sea by ~2-4‰ compared to the 5‰ of observations (Figure S23). *VarP:N* increases $\delta^{15}N$ by an additional 2‰, causing a significant overestimation for most of the North Pacific. *VarP:N* also causes strong $\delta^{15}N$ increases, ~9‰, off southern Central America and the Arabian Sea from the observed 9‰ and 5‰ values, respectively (Figure S23). Similar to the PI simulations, *VarSi:N* shows little effect on the $\delta^{15}N$ values, whereas the *Tuned* simulation corrects the large overestimation caused by *VarP:N* in the North Pacific and Bering Sea. The $\delta^{15}N$ values are reduced below those of the LGM *Control* and are in better agreement with the observed data, differing by ~1‰. $\delta^{15}N$ off southern Central America and the Arabian Sea values remain elevated.
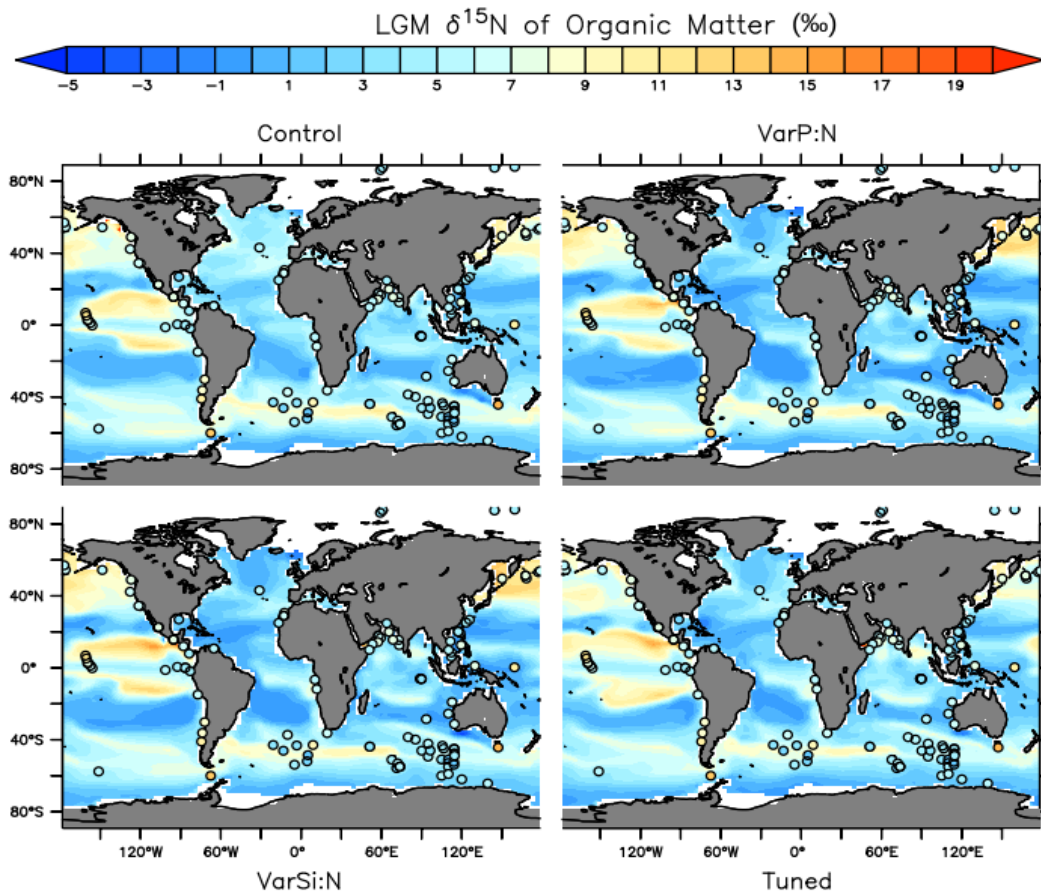

Figure S23. $\delta^{15}N$ of organic matter in the LGM averaged over the uppermost 120 m of the water column. Overlaid are observed values (Tesdal et al., 2013).

In the LGM North Pacific, the effects of *VarP:N* are exacerbated; water column denitrification nearly triples from the *Control* between the levels of 1250 – 4000m (Figure S25). $\delta^{15}N$ values here increased from 18 to ~42‰ (Figure S24). The *Tuned* model mitigates this strong $\delta^{15}N$ increase and is similar to the *Control* experiment's $\delta^{15}N$ in this region. A similar increase in denitrification is seen at this location in the PI but is notably weaker and less spatially extensive (Figures S21 and S24). The differences in $\delta^{15}N$ response to *VarP:N* between the PI and LGM oceans derive from the differences in NPP increases. In the PI ocean, *VarP:N* drove a 13% increase in N NPP compared to the *Control* run, while in the LGM, a 22% increase (Table 3 in the main text). Thus, the biological fractionation and denitrification influences on $\delta^{15}N$ vary.
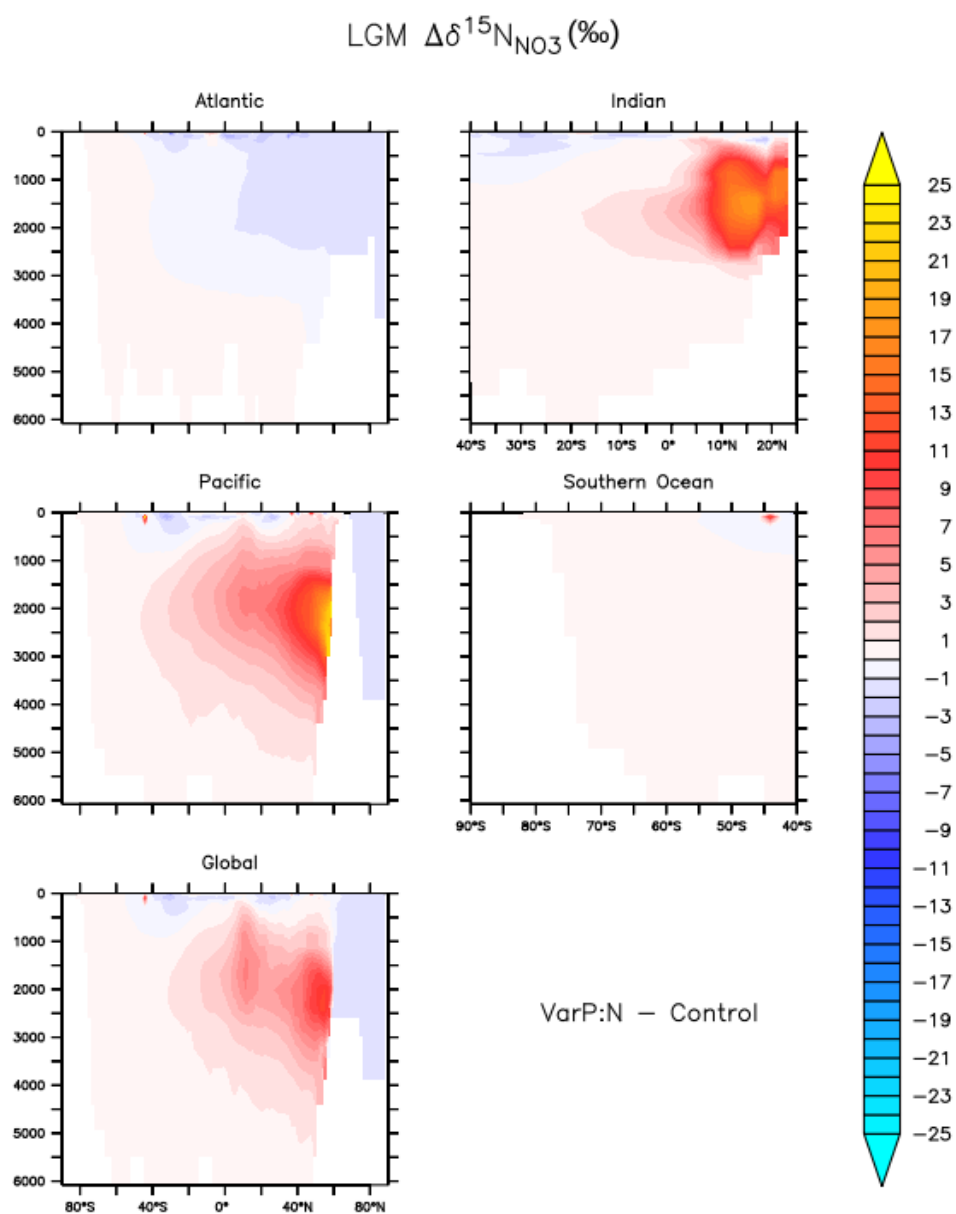
Figure S24. Changes in the $\delta^{15}N$ of NO_3 in response to VarP:N in the LGM ocean basins.
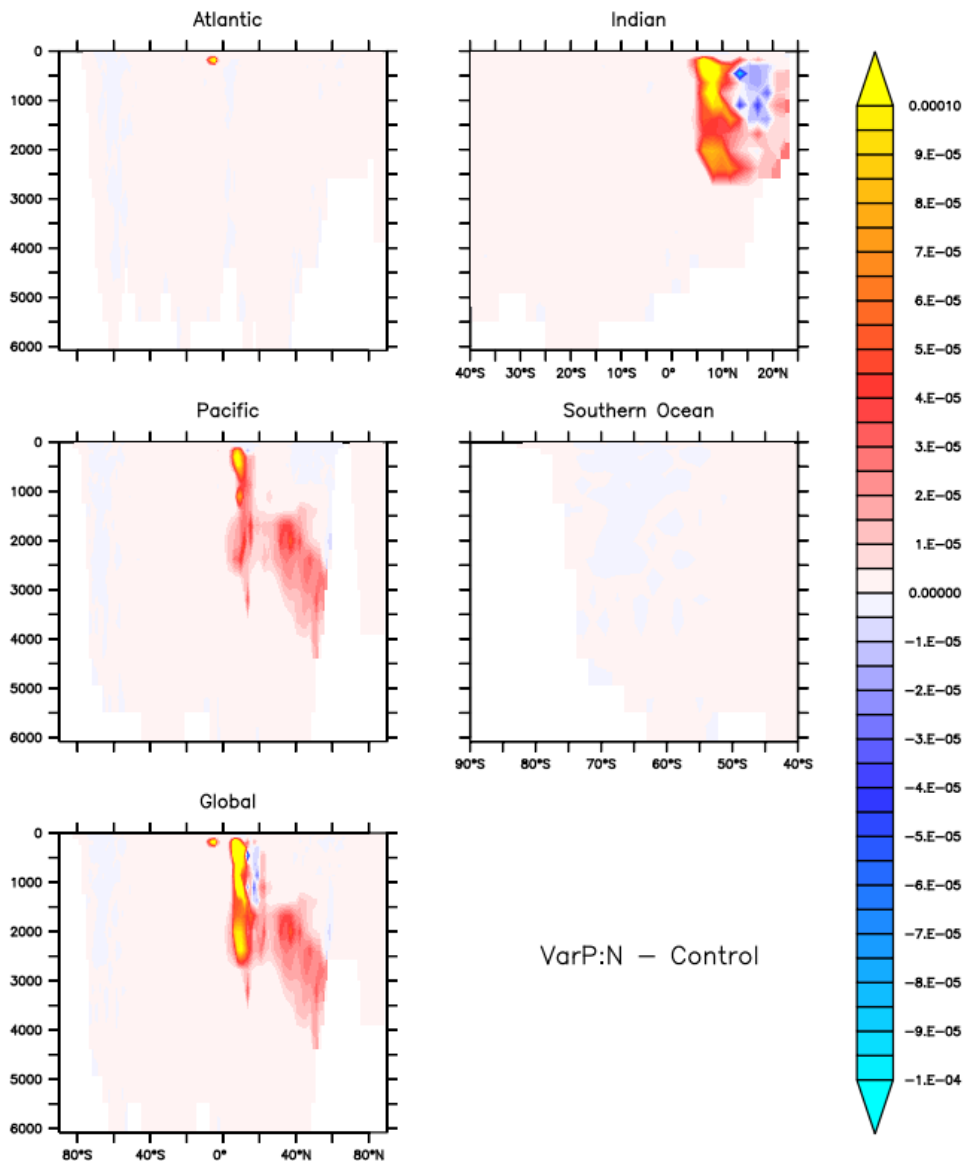
Figure S25. Changes in the water column denitrification in response to VarP:N in the LGM ocean basins.

Text S6. Biogeochemical Equations and Description

This section provides an explicit description of the new and revised prognostic equations for the implementation of the variable N:P scheme adapted from Galbraith and Martiny (2015). These are alterations of the MOBI equations in Somes and Oschlies (2015) with some portions described by external sources as referenced therein. The

inclusion of the variable N:P model necessitated two new prognostic equations to explicitly calculate the P content (indicated by the subscript "$\langle P \rangle$" of P_O and detritus (D) and a reconfiguration of the predictive PO_4 and DOP equations. The original N currency equation are noted with "$\langle N \rangle$". See Table S8 for variable and symbol descriptions.

S7.

$$
\frac{\partial PO_4^{3-}}{\partial t} = \lambda_{DOP}DOP + \mu_D^* DR_{P:N_D}
$$

$$
+ R_{P:N}\left[\gamma P_z(1-\omega)\left(\frac{R_{N:P}}{R_{P:N_{DZ}}}G_{P_{DZ}}^* + \zeta_{P_O}G_{P_O}^* + G_{P_{DT}}^* + G_{P_Z}^* + \zeta_D G_D^*\right)\right.
$$

$$
\left. + (1-\sigma2_{DOM})\mu_{P_{DT}}^* P_{DT} - \left(1-u_{DOP_{P_{DT}}}\right)J_{DT}^* P_{DT}\right]
$$

$$
+ R_{P:N_{P_O}}\left[(1-\sigma2_{DOM})\mu_{P_O}^* P_O + u_{DOP_{P_O}}J_{P_O}^* P_O\right] - R_{GM15}J_{P_O}^* P_O
$$

$$
- R_{P:N_{DZ}}\left(1-u_{DOP_{P_{DZ}}}\right)J_{DZ}^* P_{DZ}
$$

S8. Similar to Equation S7, nutrients are added to the DOP inventory at a ratio equal to the calculated N:P of P_O and detritus (S13). However, the uptake of DOP and DON is consumed at this same ratio, not by the GM15 N:P.

$$
\frac{\partial DOP}{\partial t} = R_{P:N}\left[\sigma1_{DOM}v_{P_{DT}}P_{DT} + \sigma2_{DOM}\mu_{P_{DT}}^* P_{DT} - u_{DOP_{P_{DT}}}J_{DT}^* P_{DT}\right]
$$

$$
+ R_{P:N_{P_O}}\left(\sigma1_{DOM}v_{P_O}P_O + \sigma2_{DOM}\mu_{P_O}^* P_O - u_{DOP_{P_O}}J_{P_O}^* P_O\right)
$$

$$
- R_{P:N_{DZ}}u_{DOP_{P_{DZ}}}J_{DZ}^* P_{DZ} - \lambda_{DOP}DOP
$$

S9.

$$
\frac{\partial P_{O\langle N \rangle}}{\partial t} = J_{P_O}^* P_O - \mu_{P_O}^* P_O - v_{P_O}P_O - \zeta_{P_O}G_{P_O}^* P_z
$$

S10. The P_O equation in the P currency is, again, sourced at a ratio to the N currency version that is determined by the GM15 N:P equation. Reductions to this inventory are at the N:P of the P_O.

$$\frac{\partial P_{O_{\langle P \rangle}}}{\partial t} = R_{GM15} J^*_{P_O} P_O - R_{P:N_{P_O}} \left(\mu^*_{P_O} P_O + v_{P_O} P_O + \zeta_{P_O} G^*_{P_O} P_z \right)$$

S11.

$$\frac{\partial D_{\langle N \rangle}}{\partial t} = (1 - \gamma) P_z \left(G^*_{P_{DZ}} + \zeta G^*_{P_O} + G^*_{P_{DT}} + G^*_{P_z} + \zeta G^*_D \right) + (1 - \sigma 1_{DOM}) v_{P_O} P_O - \mu^*_D D$$

$$- \zeta_D G^*_D P_z + (1 - \sigma 1_{DOM}) v_{P_{DT}} P_{DT} + \frac{R_{N:P}}{R_{N:P_{DZ}}} v_{P_{DZ}} P_{DZ} + v_{P_z} P_z^2 + w_D \frac{\partial D}{\partial z}$$

S12. The N:P of the prognostic detritus is determined by the weighted combination of the different plankton groups and post-grazing detrital matter.

$$\frac{\partial D_{\langle P \rangle}}{\partial t} = (1 - \gamma) P_z \left[R_{P:N} \left(G^*_{P_{DT}} + G^*_{P_z} \right) + R_{P:N_{DZ}} G^*_{P_{DZ}} + \zeta_{P_O} G^*_{P_O} (R_{P:N_{P_O}} - \gamma R_{P:N}) \right.$$

$$\left. + \zeta_D G^*_D (R_{P:N_D} - \gamma R_{P:N}) \right]$$

$$+ R_{P:N} \left[v_{P_z} P_z^2 + \frac{R_{N:P}}{R_{N:P_{DZ}}} v_{P_{DZ}} P_{DZ} + (1 - \sigma 1_{DOM}) v_{P_{DT}} P_{DT} \right]$$

$$+ R_{P:N_D} \left(w_D \frac{\partial D}{\partial z} - \zeta_D G^*_D P_z - \mu^*_D D \right) + R_{P:N_{P_O}} (1 - \sigma 1_{DOM}) v_{P_O} P_O$$

S13. Expression of the P_O and detritus P:N for each timestep and grid box.

$$R_{P:N_X} = \frac{X_{\langle P \rangle}}{X_{\langle N \rangle}},$$

where $X = [P_O, D]$.

S14. ζ acts to regulate the zooplankton grazing on P_O and detritus that are now under variable stoichiometry schemes. If a grazed particle is lacking in P, it is viewed as not nutritious, and the grazing is turned off. This was done to preserve the computational efficiency and realism of having fixed zooplankton stoichiometry without having unrealistic instantaneous remineralization of organic matter into inorganic nutrient constituents.

$$\zeta_X = \begin{cases} R_{P:N_X} \geq \gamma R_{P:N} \; ; \; \zeta_X = 1 \\ R_{P:N_X} < \gamma R_{P:N} \; ; \; \zeta_X = 0 \end{cases}.$$

Table S8. List of biogeochemical variables, their symbols, values, and units.

Variable/Description	Symbol	Value	Units
Ordinary Phytoplankton	P_O	-	mol m^{-3}
Diazotrophs	P_{Diaz}	-	mol m^{-3}
Diatoms	P_{Diat}	-	mol m^{-3}
Zooplankton	P_Z	-	mol m^{-3}
Detritus	D	-	mol m^{-3}
DOP remineralization rate	λ_{DOP}	-	day^{-1}
DON remineralization rate	λ_{DON}	-	day^{-1}
Detritus remineralization rate	μ_D^*	-	day^{-1}
Zooplankton assimilation efficiency	γ	0.7	day^{-1}
Zooplankton growth efficiency	ω	0.54	-
Grazing rate	G^*	-	-
Selective grazing regulator	ζ	0, 1	-
Fraction of phytoplankton mortality routed to DOM	$\sigma 1$	0.1	-
Fraction of microbial fast-recycling routed to DOM	$\sigma 2$	0.08	-
Quadratic mortality rate	υ	-	day^{-1}
Specific mortality rate	μ^*		day^{-1}
Phosphorus uptake source regulator	u_{DOP}	0, J^*	-
Growth rate	J^*	-	-
Variable P:N uptake as defined by GM15	R_{GM15}	-	mol mol^{-1}
Redfield P:N	$R_{P:N}$	1/16	mol mol^{-1}
Diazotroph P:N	$R_{P:N_{DZ}}$	1/40	mol mol^{-1}
Variable traced in N units	<N>	-	-
Variable traced in P units	<P>	-	-
Sinking Velocity of POM	w_D	-	s^{-1}

Note. A "-" in the value column indicates that the item is variable as a function of nutrient availability, temperature, etc. (Somes & Oschlies, 2015).